PHYSICS BASED WASHING MACHINE SIMULATIONS

by

Deniz Tolga Akcabay

A dissertation submitted in partial fulfillment
of the requirements for the degree of
Doctor of Philosophy
(Mechanical Engineering)
in the University of Michigan
2007

Doctoral Committee:

Professor David R. Dowling, Co-Chair
Professor William W. Schultz, Co-Chair
Professor Robert Krasny
Professor Noel C. Perkins
Associate Professor Bogdan I. Epureanu

To my parents and to the memory of Ahmet Tan

ACKNOWLEDGEMENTS

I would like to thank Prof. David Dowling and Prof. William Schultz for their continuous support and guidance as well as for editing this thesis. I would like to thank Prof. Noel Perkins, Prof. Robert Krasny, and Prof. Bogdan Epureanu for being in my dissertation committee.

I am grateful to the Whirlpool Corporation for their interest in this work and their financial support. I specifically want to thank John Patera, Kurt Werner, Raveendran Vaidhyanathan, Flavio Bernardino, and Scott Slabbekoorn for their enthusiasm.

I would like to thank Jinli Feng for her interest in my work and helping me through this research. I would like to thank Brock Palen and the University of Michigan - Center of Advanced Computing (CAC) for their computing resources as well as their great support.

I would like to thank my friends from 2010 AutoLab, and 2200 EECS for the happy times we had together and their support.

Finally, I would like to thank my parents for their continuous support.

TABLE OF CONTENTS

LIST OF FIGURES

LIST OF TABLES

ABSTRACT

This thesis describes the development of a simulation of the interaction of cloth and water that takes place inside a washing machine. The simulation consists of four basic parts: a large deformation elastic thin plate model for the cloth based on Love (1944), a rectangular-Cartesian-mesh solver for the Navier-Stokes equations based on Brown et al. (2001), the Immersed Boundary method of Peskin (1972) for cloth/fluid interaction, and a domain-mapping technique for representing irregular domain boundaries on Cartesian grids.

Although the lack of an accompanying experimental effort prevented its thorough validation, the final simulation was subjected to a variety of validation tests involving analytical solutions and experimental measurements in simple geometries. The implementation of the thin plate model combined with the Immersed Boundary method was able to match the natural frequencies of a vibrating plate within +/- 1%, and was able to predict large deformation beam shapes with similar accuracy. In addition, this validation effort suggests that the ratio between the Immersed Boundary method's Lagrangian and Eulerian point-spacings should be approximately unity for better accuracy, when accounting for finite bending stiffness. Furthermore, it was found that the Immersed Boundary method formulation may provide better results with a narrow desingularization of the two-dimensional cloth onto the three-dimensional Cartesian mesh while sacrificing numerical stability. Complicated moving boundaries are handled by a domain-mapping technique that uses a Heaviside function to switch between solving the equations for the cloth/fluid mixture and specifying the velocity field for the washing machine's solid boundaries. This boundary-condition formulation was benchmarked against well-known steady and unsteady flow fields: circular Couette flow, and a uniform flow past a cylinder.

Using these individually verified basic components together, two and three-dimensional simulations of the washing machine processes are created. A selection of studies involving the effect of different numerical and physical parameters on the kinematics of cloth motion and the statistics of the cloth stresses in a vertical-axis washing machine are reported. In particular, the coarse grid simulations predicted a realistic and qualitatively correct pattern for the motion of the cloth pieces.

CHAPTER I
INTRODUCTION

Since their invention, washing machines are perhaps one of the most important practical tools that have changed our day-to-day life. Their working principle is exceptionally simple: the agitation of cloth pieces in a detergent/water mixture. In this sense, its basic principle is not very different from hand washing of clothes as done for thousands of years. However, detailed physical descriptions of the process are very complex due to the coupled three-dimensional motions of the fluid and cloth, the large and complex cloth deformations, the cloth permeability, and the unsteadiness of the fluid motion. This limits most of the washing machine developments to be driven empirically. In accordance with today's ever increasing demand for better resource management, it is more important to be able to design energy- and water- efficient washing machines. Hence, this requires a better understanding of the physics of the washing machine processes than allowed by the empirical models.

This work presents the numerical simulation development of the washing machine processes based on basic physical models. The simulation consist of a large deformation, elastic, thin cloth model based on Love (1944), a Cartesian-grid Navier-Stokes equations solver based on Brown et al. (2001), Peskin (1972) Immersed Boundary method to couple the cloth/water dynamics, and a domain-mapping technique for representing the irregular geometries of the washing machine agitator and drum on a simple Cartesian grid.

Ward (1999) modeled horizontal-axis washing machines by describing the clothes as a simple single fabric-plug. The motion of the fabric-plug in the basket is modeled for each of its three states: 1) as the fabric-plug is pulled through the water (at the bottom of the basket) by drum rotation, 2) as the fabric is lifted out of the water and 3) as the fabric-plug impacts the air-water interface upon re-entering. Most of the related research on cloth mechanics, computational fluid mechanics, and fluid/structure models will be presented in subsequent chapters.

The clothes washing process is chaotic and governed by multiphysics, it can be considered high Reynolds number, and is in a complex unsteady geometry. As such, the computational demands for the simulation are very large. Since this is the first simulation of its kind, the emphasis is on model development rather than putting the simulation onto a high-performance computing machine. These simulations were run on one processor at a time, and hence, the two-dimensional simulations are only moderately well resolved and the three-dimensional modeling is coarse.

This thesis has been organized as follows:

- Chapter 2 presents the numerical solution of the Navier-Stokes equations and in particular presents the Brown et al. (2001) fractional step method used in the simulation.
- Chapter 3 presents the cloth model based on Love (1944), the fluid/structure interaction model based on Peskin (1972) Immersed Boundary method.
- Chapter 4 presents a domain-mapping technique to represent irregular domain geometries on a simple Cartesian grid.
- Chapter 5 presents the two- and three-dimensional simulations of the washing machine processes.
- Finally, Chapter 6 summarizes the results, specific conclusions and contributions.

CHAPTER II
NUMERICAL SOLUTION OF THE NAVIER-STOKES EQUATIONS

2.1 Introduction

As will be discussed in Chapter 3, the fluid-structure interaction between the washing fluid and cloth pieces is modeled in such a way that their coupled dynamics could be described by variable coefficient Navier-Stokes equations with body forces, so the numerical solution of the Navier-Stokes equation acts as the backbone of the simulation. Although the present simulation's fluid/structure interaction algorithm is reported to have a low-order spatial accuracy, higher-order improvements exist in the literature and anticipating to update the present solution method in the future, it is desirable to have an algorithm that solves the Navier-Stokes equations with high-order of accuracy.

The numerical solution of the incompressible Navier-Stokes equations has been of interest for at least the past four decades and although various solution methods exist and they have been continuously improved, they still bear issues that attract interest and research, some of which will be discussed later in this chapter. Generally speaking, most of the solution methods could be roughly categorized into the so-called: 1) projection methods, 2) grid based vorticity methods, 3) meshless vortex methods, and 4) artificial compressibility methods. The projection methods are further divided into the so-called fractional step methods and pressure-correction methods, whereas the vorticity methods are further divided into the vorticity-vector potential and vorticity-velocity methods. All of these methods have merits and weaknesses, and all the methods except the meshless vortex methods use an Eulerian grid. The text of Ferziger and Peric (2002) briefly summarizes the projection, vorticity-vector potential and artificial compressibility methods. Also, Guj et al. (1993) briefly compares the vorticity-vector potential methods to the vorticity-velocity methods by further referring to Gresho (1991). In addition, the recent article by Yokota et al. (2007) and the survey article by Koumoutsakos (2005) summarize the current status of the meshless vortex methods with citing several further references.

The present simulation code uses a fractional step method because the fluid/structure interaction studies in the literature, particularly involving largely deformable solids, most frequently used them.

Note that, this chapter is only a summary of established methods and no contribution is claimed here.

2.2 Numerical Method

The Navier-Stokes equations for describing the dynamics of a Newtonian and incompressible fluid in a bounded domain Ω with boundaries $\partial\Omega$ read as:

$$\begin{aligned} &\rho\left(\frac{\partial \mathbf{u}}{\partial t}+\mathbf{u}\circ\nabla\mathbf{u}\right)=-\nabla p+\mu\nabla^2\mathbf{u}+\mathbf{f} \\ &\nabla\circ\mathbf{u}=0 \\ &\mathbf{u}\big|_{\partial\Omega}=\mathbf{u}_b \end{aligned} \qquad \textbf{(2.2-1)}$$

where $\mathbf{u}$ and $\mathbf{u}_b$ are respectively the velocities inside Ω and on $\partial\Omega$, ρ is the density, μ is the viscosity, p is the pressure, and $\mathbf{f}$ is the external body force exerted on the fluid. In this form, all these variables are parameterized in an Eulerian description with current space variable $\mathbf{x}$ and time variable t. Interested readers can refer to one of the numerous fluid mechanics texts available, such as Kundu et al. (2004), for a derivation of the Navier-Stokes equations.

Following Section 2.1 on the various methods for numerically solving the Navier-Stokes equations, this section discusses the fractional step method that has been used as a part of the simulation. As it might suggest from its name, fractional step methods attempt to solve the Navier-Stokes equations by rewriting them as a set of sequential equations which are relatively easier to solve numerically. In general, any fractional step method sequence between two discrete time levels t^{n} and $t^{\mathrm{n+1}}$ consists of the following steps:

1. Solve the linear-momentum equation part of the Navier-Stokes equations, Eqn. (2.2-2), in terms of a velocity field $\mathbf{u}^*$ at the next time level $t^{\mathrm{n+1}}$ without referring to the mass-continuity equation.

   $$\rho\left(\frac{\partial \mathbf{u}^*}{\partial t} + \mathbf{u}^* \circ \nabla \mathbf{u}^*\right) = -\nabla q + \mu \nabla^2 \mathbf{u}^* + \mathbf{f} \qquad \textbf{(2.2-2)}$$

   The boundary conditions of Eqn. (2.2-2) are discussed in Section 2.2.1. Also as will be described later, some fractional step methods omit the pressure term of the original Navier-Stokes equations at this step, so in Eqn. (2.2-2) the regular pressure term is replaced with a new parameter q, which may or may not be zero. Not surprisingly, the computed velocity field $\mathbf{u}^*$ will not necessarily satisfy the mass-continuity equation.

2. Decompose the velocity field $\mathbf{u}^*$ into its gradient and divergence-free parts as in Eqn. (2.2-3). This is done by the Hodge/Helmholtz decomposition, which will be discussed in Section 2.2.1 in greater detail.

   $$\mathbf{u}^* = \mathbf{u}^{n+1} + \frac{t^{n+1} - t^n}{\rho} \nabla \tilde{p} \qquad \textbf{(2.2-3)}$$

   In Eqn. (2.2-3), $\mathbf{u}^{n+1}$ is the divergence-free and $\nabla \tilde{p}$ is the gradient/curl-free part of $\mathbf{u}^*$.

3. Assign the divergence-free part of $\mathbf{u}^*$ as the solution of the Navier-Stokes equation at time $t^{\mathrm{n+1}}$ as $\mathbf{u}^{n+1}$.

$$\mathbf{u}^{\mathrm{n}+1} = \mathbf{u}^{*} - \frac{\Delta t}{\rho}\nabla\tilde{p} \qquad \textbf{(2.2-4)}$$

4. If necessary, compute the pressure p using $\tilde{p}$. This is achieved by substituting Eqn. (2.2-3) into the time-discrete form of Eqn. (2.2-2) and comparing the resulting equation to the Navier- Stokes equations' (Eqn. (2.2-1)) linear momentum part.

This idea was first proposed by Chorin (1969) and Temam (1968). There are different fractional step methods that vary in their numerical details and accuracies. The most notable ones are by Kim et al. (1985), Bell et al. (1989, 1991), and Brown et al. (2001). Their most important differences are in their approaches to the first and fourth steps stated above. In our computations we use the method suggested by Brown et al. (2001).

2.2.1 Decomposing a vector field into its gradient and divergence-free parts (Hodge/Helmholtz decomposition)

The Hodge/Helmholtz decomposition uniquely decomposes a vector field into divergence-free and gradient vector fields provided that some conditions, which will be stated below, hold true. For a vector field $\mathbf{u}^{*}$ this decomposition could be written as

$$\mathbf{u}^{*} = \mathbf{u}^{n+1} + \nabla\tilde{\phi} \qquad \textbf{(2.2-5)}$$

where

$$\nabla \circ \mathbf{u}^{n+1} = 0 \;\Leftrightarrow\; \int_{\partial\Omega} \mathbf{u}^{n+1} \circ \mathbf{n}\, dA = 0 \qquad \textbf{(2.2-6)}$$

In these and in the following equations **n** is the normal outward vector at $\partial\Omega$, V is an infinitesimal volume in Ω, and similarly A an infinitesimal area on $\partial\Omega$.

Stated next is the approach given by Chorin (1990) to prove the decomposition. But first, a particular orthogonality condition between the divergence-free and gradient vector fields can be defined as

$$\int_{\Omega} \left(\mathbf{u}^{n+1} \circ \nabla \tilde{\phi} \right) dV = \int_{\Omega} \left(\nabla \circ \left(\phi \mathbf{u}^{n+1} \right) - \tilde{\phi} \left(\nabla \circ \mathbf{u}^{n+1} \right) \right) dV = \int_{\Omega} \left(\nabla \circ \left(\tilde{\phi} \mathbf{u}^{n+1} \right) \right) dV = \int_{\partial\Omega} \tilde{\phi} \mathbf{u}^{n+1} \circ \mathbf{n} \, dA = 0$$

(2.2-7)

This equality is clearly true if $\mathbf{u}^{n+1}$ is always parallel to the domain boundaries $\partial\Omega$ or $\tilde{\phi}$ is constant on the boundaries. However, note that the integral form of Eqn. (2.2-6) is not sufficient to satisfy Eqn. (2.2-7) for a general $\tilde{\phi}$.

Uniqueness of the Hodge/Helmholtz decomposition

Assume the Hodge/Helmholtz decomposition of $\mathbf{u}^*$ is not unique, and decompose $\mathbf{u}^*$ as

$$\mathbf{u}^* = \left(\mathbf{u}^{n+1} \right)_1 + \left(\nabla \tilde{\phi} \right)_1 = \left(\mathbf{u}^{n+1} \right)_2 + \left(\nabla \tilde{\phi} \right)_2$$

such that

$$\nabla \circ \left(\mathbf{u}^{n+1} \right)_1 = 0 \iff \int_{\partial\Omega} \left(\mathbf{u}^{n+1} \right)_1 \circ \mathbf{n} \, dA = 0, \quad \nabla \circ \left(\mathbf{u}^{n+1} \right)_2 = 0 \iff \int_{\partial\Omega} \left(\mathbf{u}^{n+1} \right)_2 \circ \mathbf{n} \, dA = 0$$

This implies

$$\left(\mathbf{u}^{n+1} \right)_2 - \left(\mathbf{u}^{n+1} \right)_1 + \left(\nabla \tilde{\phi} \right)_2 - \left(\nabla \tilde{\phi} \right)_1 = \mathbf{0} \qquad \textbf{(2.2-8)}$$

Also, if one defines

$$
\begin{aligned}
\left(\mathbf{u}^{n+1}\right)_{diff} &= \left(\mathbf{u}^{n+1}\right)_2 - \left(\mathbf{u}^{n+1}\right)_1 \\
\left(\nabla\tilde{\phi}\right)_{diff} &= \left(\nabla\tilde{\phi}\right)_2 - \left(\nabla\tilde{\phi}\right)_1
\end{aligned}
$$

and takes the inner product of Eqn. (2.2-8) with $(\mathbf{u}^{n+1})_{diff}$ and integrates it over Ω, the result is

$$\int_{\Omega}\left(\mathbf{u}_{diff}^{n+1}\right)^2 dV + \int_{\Omega}\left(\nabla\tilde{\phi}_{diff}\circ\mathbf{u}_{diff}^{n+1}\right) dV = \int_{\Omega}\left(\mathbf{u}_{diff}^{n+1}\right)^2 dV + \int_{\partial\Omega}\tilde{\phi}_{diff}\,\mathbf{u}_{diff}^{n+1}\circ\mathbf{n}\,dA = 0 \qquad \textbf{(2.2-9)}$$

Observe that the first term in Eqn. (2.2-9) is non-negative and the second term is zero provided that either $\mathbf{u}_{diff}^{n+1}\circ\mathbf{n}=0$ on $\partial\Omega$ or $\tilde{\phi}_{diff}$ is constant on $\partial\Omega$. Note also that, if $\mathbf{u}^{*}\circ\mathbf{n}=\mathbf{u}^{n+1}\circ\mathbf{n}$ is used as a boundary condition then the condition for $\mathbf{u}_{diff}^{n+1}\circ\mathbf{n}=0$ on $\partial\Omega$ would still be satisfied.

As long as the second term in Eqn. (2.2-9) is zero, the rest of Eqns. (2.2-9) with (2.2-8) would suggest $\mathbf{u}_{diff}=\mathbf{0}$ and $\nabla\tilde{\phi}_{diff}=\mathbf{0}$, and hence prove the uniqueness of the Hodge/Helmholtz decomposition. Interested readers could refer to Denaro (2003) for a further discussion on the uniqueness of the Hodge/Helmholtz decomposition and the implications of failing to satisfy it. Note that the rather popular application cases for solving/testing the Navier-Stokes equations with open boundaries (e.g. flow over a cylinder) might not ‘explicitly’ satisfy the uniqueness condition above. However, it is shown in Chapter 5 that the setups for the simulations inside a washing machine are designed such that one can always set $\mathbf{u}^{*}\circ\mathbf{n}=\mathbf{u}^{n+1}\circ\mathbf{n}=0$.

Implementation of the Hodge/Helmholtz decomposition and a note on its existence

Having discussed the uniqueness of the Hodge/Helmholtz decomposition, the following equations describe its implementation. In the scope of designing a fractional step method for solving the Navier-Stokes equations, it is customary to choose $\tilde{\phi}$ in pressure units and scale it with the time step and fluid density to find a velocity unit, such as

$$\mathbf{u}^* = \mathbf{u}^{n+1} + \frac{\Delta t}{\rho}\nabla\tilde{p} \qquad \textbf{(2.2-10)}$$

Taking the divergence of Eqn. (2.2-10), one gets

$$\frac{1}{\Delta t}\nabla\circ\mathbf{u}^* = \nabla\circ\left(\frac{1}{\rho}\nabla\tilde{p}\right) \qquad \textbf{(2.2-11)}$$

And if the following boundary conditions are chosen for Eqn. (2.2-2)

$$\mathbf{u}^*\circ\mathbf{n} = \mathbf{u}^{n+1}\circ\mathbf{n} = \mathbf{u}_b\circ\mathbf{n} \ \text{ on } \partial\Omega \qquad \textbf{(2.2-12)}$$

together with Eqn. (2.2-10) this implies

$$\nabla\tilde{p}\circ\mathbf{n} = 0 \ \text{ on } \partial\Omega \qquad \textbf{(2.2-13)}$$

Equation (2.2-11) with (2.2-13) is the Poisson equation with homogenous Neumann boundary conditions, which is solvable in terms of $\tilde{p}$ up to a constant. Chorin (1990) refers to Courant et al. (1953) for a further discussion on the existence of solutions. However to set an important requirement for the existence of solutions, note that the following is the weak form of Eqn. (2.2-11)

$$\int_{\Omega}\frac{1}{\Delta t}\nabla\circ\mathbf{u}^*\,dV = \int_{\partial\Omega}\frac{1}{\rho}\nabla\tilde{p}\circ\mathbf{n}\,dA$$

For the boundary condition given in Eqn. (2.2-13), this would imply

$$\int_{\Omega} \frac{1}{\Delta t} \nabla \circ \mathbf{u}^* \, dV = 0 \qquad \textbf{(2.2-14)}$$

which is nothing new, but a trivial statement provided that $\mathbf{u}^* \circ \mathbf{n} = \mathbf{u}^{n+1} \circ \mathbf{n}$ on $\partial\Omega$ and the mass-continuity equation, $\int_{\partial\Omega} \mathbf{u}^{n+1} \circ \mathbf{n} \, dA = 0$, hold true. However, depending on the way Eqn. (2.2-11) is discretized, this compatibility condition may be violated. This issue will be addressed in Section 2.2.6.

Observe that with different boundary conditions selections for Eqn. (2.2-2), such as the one in Eqn. (2.2-12), different boundary conditions could be obtained for the Poisson equation and any such pair of boundary condition selections needs to be consistent via Eqn. (2.2-10).

In a similar way, it seems natural to use the following for the tangential part of the boundary conditions for $\mathbf{u}^*$ in Eqn. (2.2-2):

$$\mathbf{u}^* \circ \boldsymbol{\tau} = \mathbf{u}^{n+1} \circ \boldsymbol{\tau} = \mathbf{u}_b \circ \boldsymbol{\tau} \ \text{ on } \partial\Omega \qquad \textbf{(2.2-15)}$$

where $\boldsymbol{\tau}$ is a tangent vector along two possible directions on $\partial\Omega$. Note that, Eqn. (2.2-15) together with Eqn. (2.2-10) would further imply

$$\nabla \tilde{p} \circ \boldsymbol{\tau} = 0 \ \text{ on } \partial\Omega \qquad \textbf{(2.2-16)}$$

However, Eqn. (2.2-11) can only admit a single boundary condition at a given point on $\partial\Omega$, so both Eqn. (2.2-13) and Eqn. (2.2-16) could not be simultaneously enforced. In Brown et al. (2001), the authors discuss this issue and argue that if an accurate approximation to p could be used for q in Eqn. (2.2-2), $\mathbf{u}^*$ would not be too different from $\mathbf{u}^{n+1}$ and using Eqn. (2.2-15) without enforcing Eqn. (2.2-16) would not degrade the accuracies of the results. However, some fractional step methods, such as Kim et al. (1985), omits the term q in Eqn. (2.2-2), and they use

$$\mathbf{u}^* \circ \boldsymbol{\tau} = \left(\mathbf{u}^{n+1} + \frac{\Delta t}{\rho} \nabla \tilde{p} \right) \circ \boldsymbol{\tau} = \left(\mathbf{u}_b + \frac{\Delta t}{\rho} \nabla \tilde{p} \right) \circ \boldsymbol{\tau} \quad \text{on } \partial\Omega \qquad \textbf{(2.2-17)}$$

with an accurate approximation to $\nabla \tilde{p}$ (note that $\nabla \tilde{p}$ at the present time step is not yet known while solving Eqn. (2.2-2)) to retain accuracy.

As a final remark it is important to point out that although $\tilde{p}$ has pressure units, in general the actual pressure p is different from it and can be evaluated with a known $\tilde{p}$. As will be shown later, the relationship between p and $\tilde{p}$ could be revealed by substituting Eqn. (2.2-10) into the time-discretized form of Eqn. (2.2-2) and comparing the resulting equation to the Navier-Stokes equations' (Eqn. (2.2-1)) linear momentum part.

2.2.2 Kim et al. (1985) fractional step method

As mentioned in Section 2.2.1, Kim et al. (1985) neglects the pressure term (i.e. $q = 0$) while solving the linear momentum equations in the first step of the fractional step method sequence (Eqn. (2.2-2)). They treat the nonlinear hyperbolic terms explicitly with 2nd order Adams-Bashforth, and the viscous terms implicitly with the Crank-Nicholson expressions. So, their time-discrete equations look like

$$\rho \left(\frac{\mathbf{u}^* - \mathbf{u}^n}{\Delta t} + \frac{3}{2}\left(\mathbf{u}^n \circ \nabla \mathbf{u}^n \right) - \frac{1}{2}\left(\mathbf{u}^{n-1} \circ \nabla \mathbf{u}^{n-1} \right) \right) = \frac{1}{2} \mu \nabla^2 \left(\mathbf{u}^* + \mathbf{u}^n \right) + \mathbf{f}^{n+\frac{1}{2}} \qquad \textbf{(2.2-18)}$$

together with the following boundary conditions

$$\begin{aligned} &\mathbf{u}^* \circ \mathbf{n} = \mathbf{u}_b \circ \mathbf{n} \\ &\mathbf{u}^* \circ \boldsymbol{\tau} = \left(\mathbf{u}_b + \frac{\Delta t}{\rho} \nabla \tilde{p} \right) \circ \boldsymbol{\tau} \end{aligned} \qquad \textbf{(2.2-19)}$$

Observe that this boundary condition pair is consistent with Eqn. (2.2-10) if using $\nabla\tilde{p}\circ\mathbf{n}=0$ on $\partial\Omega$ to solve the Poisson equation Eqn. (2.2-11). In the second boundary condition of Eqn. (2.2-19), they approximate $\nabla\tilde{p}$ using the $\nabla\tilde{p}$ from the previous time step, since its recent value is unknown before solving Eqn. (2.2-11). The second and third steps of Kim et al. (1985) fractional method sequence are as given in Section 2.2 and 2.2.1. They update the pressure with

$$p^{n+\frac{1}{2}}=\tilde{p}-\frac{\Delta t\,\mu}{2\rho}\nabla^2\tilde{p}$$

Brown (2001) and Brown et al. (2001) report that this method has second-order accuracy in time for velocity, but they also add for some problems the pressure has a degraded convergence rate.

2.2.3 Brown (2001) and Brown et al. (2001) fractional step method

Brown (2001) and Brown et al. (2001) use the most recently computed pressure field (i.e. $q=p^{n\text{-}1/2}$) while solving the linear momentum equations (Eqn. (2.2-2)). Using Adams-Bashforth and Crank-Nicholson expansions for the hyperbolic and viscous terms respectively, Eqn. (2.2-2) is time-discretized as

$$\rho\left(\frac{\mathbf{u}^*-\mathbf{u}^n}{\Delta t}+\frac{3}{2}\left(\mathbf{u}^n\circ\nabla\mathbf{u}^n\right)-\frac{1}{2}\left(\mathbf{u}^{n-1}\circ\nabla\mathbf{u}^{n-1}\right)\right)=-\nabla p^{n-\frac{1}{2}}+\frac{1}{2}\mu\nabla^2\left(\mathbf{u}^*+\mathbf{u}^n\right)+\mathbf{f}^{n+\frac{1}{2}}$$

(2.2-20)

They use the following boundary conditions for Eqn. (2.2-20):

$$\mathbf{u}\big|_{\partial\Omega}=\mathbf{u}_b \qquad \textbf{(2.2-21)}$$

The second and third steps of their fractional method sequence are as given in Section 2.2 and 2.2.1.They update the pressure by

$$p^{n+\frac{1}{2}} = p^{n-\frac{1}{2}} + \tilde{p} - \frac{\Delta t \mu}{2\rho} \nabla^2 \tilde{p}$$

and report their method to be second-order accurate in time for both the velocity and pressure fields.

2.2.4 Grid choices

This study uses a structured Cartesian finite-volume grid, in particular the ‘Marker and Cell’ (MAC) grid suggested by Harlow et al. (1965). The advantages of using a structured Cartesian grid for fluid/structure interaction problems will be discussed in Chapter 3, but in the scope of solving the Navier-Stokes equations, structured grids allows using uniform discretizations throughout the fluid domain, while avoiding the following nontrivial extra tasks related to the usage of unstructured grids: grid generation, bookkeeping the grid points’ connectivities, and tedious interpolations. On the other hand, the advantage of the unstructured grids against the structured ones is their conformability to domains with complex geometries. Chapter 4 will present the way the simulation handles domains with complex geometries using structured Cartesian grids.

On a MAC grid the pressure variables are defined at the centers of the finite-volumes and the velocities are defined on the edges as plotted in 2D in Fig. 2.2-1.

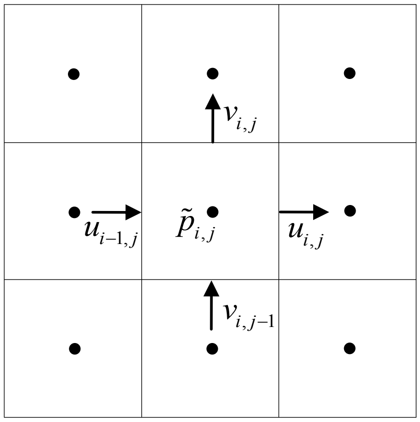

Figure 2.2-1: A two-dimensional 'Marker and Cell' (MAC) grid for solving the fluid dynamics equations

MAC grids are more intuitive when applied to the weak/integral form of the Navier-Stokes equations and the pressure-velocity coupling is stronger compared to the non-staggered grids, since the pressure nodes are between the velocity nodes. Furthermore, as would be discussed in Section 2.2-6 a discrete compatibility condition required for the existence of solutions for Eqn. (2.2-11) is naturally satisfied on a staggered grid, which is not necessarily the case for the non-staggered grids without taking special care.

2.2.5 Numerically solving Eqn. (2.2-20)

This study uses the Brown (2001) and Brown et al. (2001) fractional step method and in doing so, the integral form of Eqn. (2.2-20), as given below in Eqn. (2.2-22), is discretized on a MAC grid.

$$\int_V \rho \frac{\mathbf{u}^* - \mathbf{u}^n}{\Delta t} dV + \int_A \left(\frac{3}{2}\rho \mathbf{u}^n \left(\mathbf{u}^n \circ \mathbf{n}\right) - \frac{1}{2}\rho \mathbf{u}^{n-1}\left(\mathbf{u}^{n-1} \circ \mathbf{n}\right) \right) dA =$$

$$-\int_A p^{n-\frac{1}{2}} \mathbf{n}\, dA + \frac{1}{2}\int_A \mu \nabla\left(\mathbf{u}^* + \mathbf{u}^n\right) \circ \mathbf{n}\, dA + \int_V \mathbf{f}\, dV$$

(2.2-22)

Second-order accurate midpoint methods are used to evaluate the volume and area integrals, where the integrands are respectively evaluated at the centers of finite-volumes and their surface areas. While doing so, second-order accurate interpolations are used to find the midpoint values of the integrands. As a sample illustration, Eqn. (2.2-23) shows the result of this discretization on a single component of Eqn. (2.2-22), with constant fluid density and viscosity, using a two-dimensional finite-volume grid with a uniform mesh width *h* in both directions as plotted in Fig. 2.2-2.

$$\begin{aligned}
&\left(1+\frac{2\Delta t\mu}{\rho h^2}\right)u^*_{i,j}-\frac{\Delta t\mu}{2\rho h^2}\left(u^*_{i+1,j}+u^*_{i-1,j}+u^*_{i,j+1}+u^*_{i,j-1}\right)= \\
&u^n_{i,j}+\frac{\Delta t}{\rho}\left(\frac{f_{i+1,j}+f_{i,j}}{2}\right)-\frac{\Delta t}{\rho}\left(\frac{\tilde{p}^{\,n-\frac{1}{2}}_{i+1,j}-\tilde{p}^{\,n-\frac{1}{2}}_{i,j}}{h}\right) \\
&-\frac{3}{2}\frac{\Delta t}{4h}\Big[\left(u^n_{i+1,j}+u^n_{i,j}\right)^2-\left(u^n_{i,j}+u^n_{i-1,j}\right)^2 \\
&\qquad\qquad+\left(u^n_{i,j+1}+u^n_{i,j}\right)\left(v^n_{i+1,j}+v^n_{i,j}\right)-\left(u^n_{i,j}+u^n_{i,j-1}\right)\left(v^n_{i+1,j-1}+v^n_{i,j-1}\right)\Big] \\
&+\frac{1}{2}\frac{\Delta t}{4h}\Big[\left(u^{n-1}_{i+1,j}+u^{n-1}_{i,j}\right)^2-\left(u^{n-1}_{i,j}+u^{n-1}_{i-1,j}\right)^2 \\
&\qquad\qquad+\left(u^{n-1}_{i,j+1}+u^{n-1}_{i,j}\right)\left(v^{n-1}_{i+1,j}+v^{n-1}_{i,j}\right)-\left(u^{n-1}_{i,j}+u^{n-1}_{i,j-1}\right)\left(v^{n-1}_{i+1,j-1}+v^{n-1}_{i,j-1}\right)\Big] \\
&+\frac{\Delta t\mu}{2\rho h^2}\left(u^n_{i+1,j}+u^n_{i-1,j}+u^n_{i,j+1}+u^n_{i,j-1}-4u^n_{i,j}\right)
\end{aligned}$$

(2.2-23)

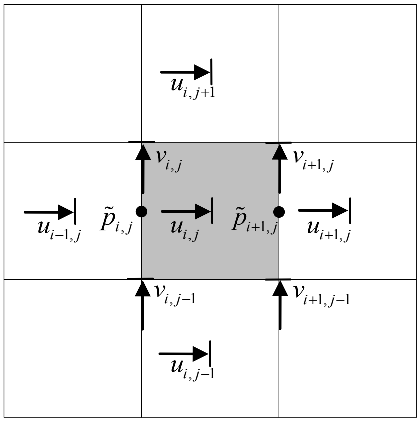

Figure 2.2-2: A finite-volume around velocity component $u_{i,j}$

Note that Eqn. (2.2-23) needs some adjustments near the domain boundaries. In general, there are two different possible configurations near the boundaries, which are shown in Fig. 2.2-3. For Case 1 in Fig.2.2-3, Eqn. (2.2-20) is still valid with $u_{i-1,j} = U_{west}$, but for Case 2 the u velocity field is linearly extrapolated through the wall to find $u_{i,j\text{-}1}$ as $\tilde{u} = 2U_{south} - u_{i,j}$. This is sometimes called as 'reflection technique' and Weinan et al. (1996) shows that it preserves the second-order spatial accuracy.

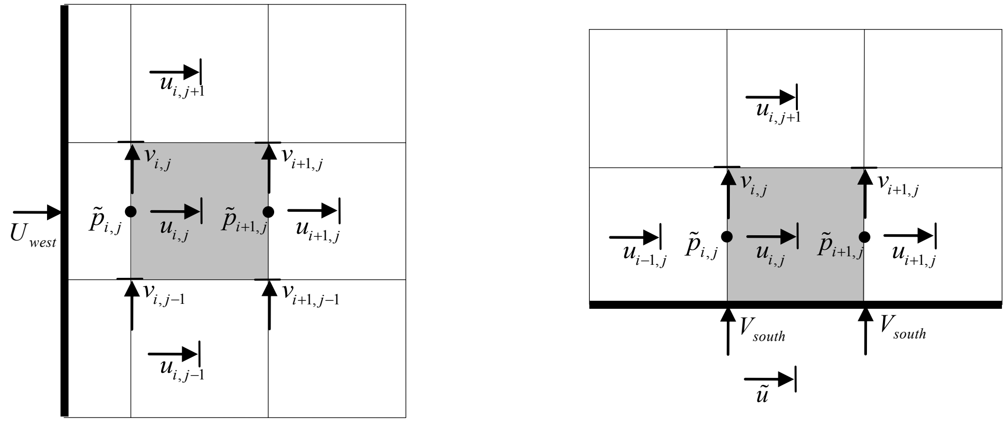

(a): Case 1 (b): Case 2

Figure 2.2-3: Two different cases at the boundaries on a staggered grid

As could be seen from Eqn. (2.2-23), discretizations to Eqn. (2.2-22) will result in a sparse matrix structure with only 5 or 7 nonzero diagonals for two or three-dimensional formulations, respectively. The simulation code takes advantage of this sparse matrix structure by only storing the non-zero diagonals, allowing any matrix-vector multiplication involving a vector with n entities to be done with only O(n) operation count. In this study Eqn. (2.2-23) is solved with the Generalized Minimal Residual (GMRES) method, whose operation count is O(n). Interested readers could refer to Trefethen et al. (1997) for a detailed description of GMRES. In the same source it is shown that the convergence speed of the GMRES method increases if the eigenvalues of the matrix part of the set of equations are clustered away from 0. Before further proceeding, it is desirable to present Gershgorin's circle theorem to assess the convergence speed of GMRES applied on the discrete forms of Eqn. (2.2-22).

Gershgorin's circle theorem states that for a general complex square matrix A, if λ is one of its eigenvalues, then there exists a matrix row index i such that

$$\left|\lambda - A_{ii}\right| \le \sum_{j,j\neq i} \left|A_{ij}\right| \tag{2.2-24}$$

Denoting u as the eigenvector match of the eigenvalue λ, Gershgorin's theorem could be proven as

$Au = \lambda u$ so for any row i one can write

$$(\lambda - A_{ii})u_i = \sum_{j,j\neq i} A_{ij}u_j \Rightarrow \left|(\lambda - A_{ii})u_i\right| = \left|(\lambda - A_{ii})\right|\left|u_i\right| = \left|\sum_{j,j\neq i} A_{ij}u_j\right| \le \sum_{j,j\neq i}\left|A_{ij}u_j\right|$$

$$\Rightarrow \left|(\lambda - A_{ii})\right| \le \sum_{j,j\neq i}\frac{\left|A_{ij}u_j\right|}{\left|u_i\right|} = \sum_{j,j\neq i}\frac{\left|A_{ij}\right|\left|u_j\right|}{\left|u_i\right|}$$

if row i is selected such that $\left|u_i\right| = \max_k\left(\left|u_k\right|\right)$

$$\left|(\lambda - A_{ii})\right| \le \sum_{j,j\neq i}\left|A_{ij}\right|$$

Observe from Eqn. (2.2-23) that the diagonal terms of the matrix of the two-dimensional implicit equations of Eqn. (2.2-22) will be $1+\frac{2\Delta t\mu}{\rho h^2}$, while the off-diagonal terms will be $-\frac{\Delta t\mu}{2\rho h^2}$. In general, the eigenvalues of the set of linear equations will be bounded in one of the circles with a center of $1+\frac{2\Delta t\mu}{\rho h^2}$ and a radius of $\sum_{i=1}^{n}\frac{\Delta t\mu}{2\rho h^2}$ where n is 4 for a two-dimensional formulation and 6 for three-dimensional formulation. Note that, the terms ρ and μ may not necessarily be constant, in general. But still one can deduce that with higher cell-Reynolds numbers and smaller time steps, the eigenvalues of Eqn. (2.2-22) will cluster around a disk that is centered near unity and the convergence of the GMRES method will be enhanced. This agrees with this present study's observations that, the real computational bottleneck of the simulations is solving the Poisson's equation given in Eqn. (2.2-11), in contrast to Eqn. (2.2-22). For a quicker alternative to the GMRES method one might apply the ADI techniques as described in Kim et al. (1985).

2.2.6 Numerically solving Eqn. (2.2-11)

This study follows the approach of Morton et al. (1994) to discretize the elliptic Poisson equation given in Eqn. (2.2-11) to compute $\tilde{p}$, which is repeated below in Eqn. (2.2-25). In their approach, Morton et al. uses finite-volumes as shown in Fig. 2.2-4 and equate the fluxes between the adjacent finite volumes sharing the same faces, in the way as given in Eqn. (2.2-26).

$$\begin{aligned} &\frac{1}{\Delta t}\nabla \circ \mathbf{u}^{*} = \nabla \circ \left(\frac{1}{\rho}\nabla\tilde{p}\right) \\ &\frac{1}{\Delta t}\int_{\partial A} \mathbf{u}^{*} \circ \mathbf{n}\, dA = \int_{\partial A}\left(\frac{1}{\rho}\nabla\tilde{p}\right)\circ \mathbf{n}\, dA \end{aligned} \tag{2.2-25}$$

$$\frac{1}{\rho_{i+1,j}}\frac{\tilde{p}_{i+1,j}-\tilde{p}_{i+1/2,j}}{h/2} = \frac{1}{\rho_{i,j}}\frac{\tilde{p}_{i+1/2,j}-\tilde{p}_{i,j}}{h/2} = \frac{1}{\rho_{i+1/2,j}}\frac{\tilde{p}_{i+1,j}-\tilde{p}_{i,j}}{h} \tag{2.2-26}$$

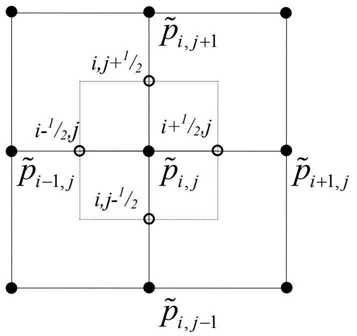

Figure 2.2-4: An imaginary finite volume used to discretize Eqn. (2.2-23)

Equation (2.2-26) gives

$$\rho_{i+1/2,j} = \frac{\rho_{i+1,j} + \rho_{i,j}}{2} \tag{2.2-27}$$

Using this result Eqn. (2.2-25) is discretized as

$$\frac{1}{\Delta t}\sum_{n=1}^{d}\left(\mathbf{u}^*\Big|_{\bar{\mathbf{x}}+\frac{h}{2}\mathbf{e}_\mathrm{n}} - \mathbf{u}^*\Big|_{\bar{\mathbf{x}}-\frac{h}{2}\mathbf{e}_\mathrm{n}}\right)\circ \mathbf{e}_\mathrm{n} = \sum_{n=1}^{d}\left[\frac{1}{\rho\big|_{\bar{\mathbf{x}}+\frac{h}{2}\mathbf{e}_\mathrm{n}}}\left(\frac{\tilde{p}\big|_{\bar{\mathbf{x}}+h\mathbf{e}_\mathrm{n}} - \tilde{p}\big|_{\bar{\mathbf{x}}}}{h}\right) - \frac{1}{\rho\big|_{\bar{\mathbf{x}}-\frac{h}{2}\mathbf{e}_\mathrm{n}}}\left(\frac{\tilde{p}\big|_{\bar{\mathbf{x}}} - \tilde{p}\big|_{\bar{\mathbf{x}}-h\mathbf{e}_\mathrm{n}}}{h}\right)\right] \tag{2.2-28}$$

where *d* is the dimension of the problem. The pressure fluxes are set to zero near the boundaries to enforce

$$\nabla\tilde{p}\circ\mathbf{n} = 0 \quad \text{on } \partial\Omega$$

The simulation code solves the set of linear equations of Eqn. (2.2-28) using the Weighted Jacobi method with Geometric Multigrid preconditioning. Interested readers could refer to Briggs et al. (2000) for further information on these methods. Solving Eqn. (2.2-28) is the bottleneck of the whole simulation, including the yet to be presented fluid/solid coupling part. The reason for this is, the eigenvalues of the matrix systems in Eqn. (2.2-28) are not necessarily clustered, as was the case for Eqn. (2.2-22), so GMRES is not efficient here. The advantage of using Weighted Jacobi method with Multigrid preconditioner is for a system of *n* equations its operation count is O(*n* log(*n*)) and it has a grid independent convergence rate. However, its convergence speed deteriorates if using highly non-uniform fluid densities and with highly anisotropic grids using non-unity aspect ratios. As a remedy, these difficulties could be tackled with Algebraic Multigrid preconditioners as discussed in Briggs et al. (2000).

Moreover, as previously discussed in Section 2.2.1, solving Eqn. (2.2-25) with $\nabla\tilde{p}\circ\mathbf{n} = 0$ on $\partial\Omega$ requires the realization of a compatibility condition (Eqn. (2.2-14)), in order to ensure existence of solutions. Eqn. (2.2-14) is repeated below

$$\int_{\Omega} \frac{1}{\Delta t} \nabla \circ \mathbf{u}^{*} dV = 0 \qquad \textbf{(2.2-29)}$$

This issue is discussed in Briggs et al. (2000), and they show that as long as the matrix of Eqn. (2.2-28) is symmetric, the discrete compatibility condition is

$$\sum_{\Omega} \left\{ \sum_{n=1}^{d} \left(\mathbf{u}^{*}\Big|_{\bar{\mathbf{x}}+\frac{h}{2}\mathbf{e}_{\mathrm{n}}} - \mathbf{u}^{*}\Big|_{\bar{\mathbf{x}}-\frac{h}{2}\mathbf{e}_{\mathrm{n}}} \right) \circ \mathbf{e}_{\mathrm{n}} \right\} = 0 \qquad \textbf{(2.2-30)}$$

Note that the sum in Eqn. (2.2-30) is a telescopic sum and if

$$\int_{\partial\Omega} \mathbf{u}^{*} \circ \mathbf{n} dA = 0$$

is satisfied, so will Eqn. (2.2-30). In practice, due to round-off errors, this might not exactly happen, so the simulation code uses a ‘correction-technique’ that calculates the residual in Eqn. (2.2-30), then divides it to the number of the discrete elements and subtracts the result from each of them. The situation is more complicated on non-staggered grids. Using one-sided differences near the boundaries and central differences elsewhere does not necessarily result in a telescopic series in Eqn. (2.2-30) to assure the sum to be zero. This issue is discussed in Pozrikidis (2001) and he suggests using the ‘correction-technique’ discussed above.

2.3 Verification study

In this section the simulation’s Navier-Stokes equations solver is tested with the two-dimensional lid driven cavity problem, as described in Fig. 2.3-1. In this problem, a Newtonian fluid is enclosed in a square cavity and the horizontal top wall is sliding with a constant speed U_o, while all the other walls are stationary. The effect of gravity is neglected. At low Reynolds numbers only the central vortex is apparent, but at higher Reynolds numbers secondary vortices become apparent at the corners. This problem has been a standard benchmark case for testing the Navier-Stokes equations solvers for single-phase fluids in simple geometries. It is simple to implement, but it reveals complex patterns of fluid motion at high enough Reynolds numbers.

This problem is non-dimensionalized with the following length, time, and mass scales:

$$l^o = a, \quad t^o = \frac{a}{U_o}, \quad M^o = \rho a^3 \qquad \textbf{(2.3-1)}$$

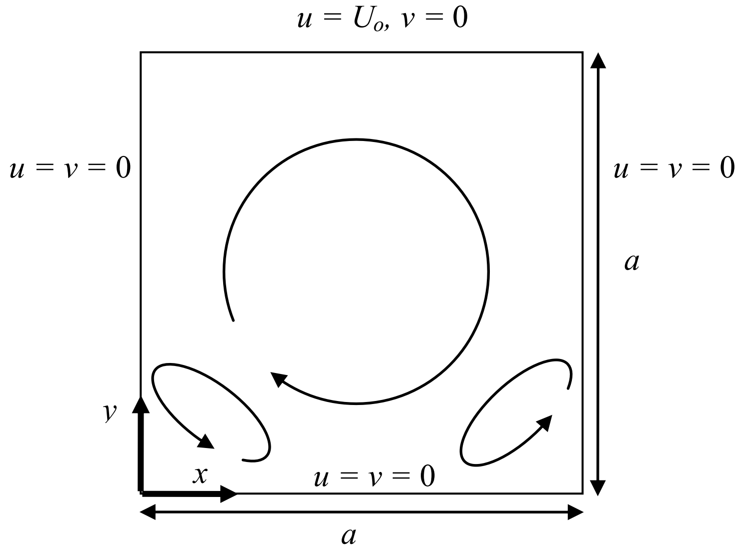

Figure 2.3-1: Two-dimensional lid driven cavity

Using these mass, length, and time scales and the boundary conditions shown in Fig. (2.3-1) the Navier-Stokes equations can be written in the following dimensionless form

$$\begin{aligned} &\frac{\partial \overline{\mathbf{u}}}{\partial \overline{t}} + \overline{\mathbf{u}} \circ \overline{\nabla}\, \overline{\mathbf{u}} = -\overline{\nabla}\, \overline{p} + \frac{1}{Re} \overline{\nabla}^2 \overline{\mathbf{u}} \\ &\overline{\nabla} \circ \overline{\mathbf{u}} = 0 \end{aligned} \qquad \textbf{(2.3-2)}$$

where

$$Re = \frac{\rho U_o a}{\mu} \qquad \textbf{(2.3-3)}$$

is the Reynolds number, which is set to 1000 in this study. In Eqn. (2.3-2), the dimensionless variables are shown with bars above them. The reason for conducting this study at this *Re* is: 1) to check if the simulation can predict the secondary vortices at the corners, which are clearly apparent at this selected *Re* and 2) to compare the results with the available data in literature, which are only tabulated at a few different *Re*.

In Figs. 2.3-2 and 2.3-3, respectively, the *x*-component of the velocity at the plane $\bar{x} = 0.5$ and the *y*-component of the velocity at the plane $\bar{y} = 0.5$ are plotted together with the computational results given in Ghia et al. (1982) using the same uniform grid size (129 x 129). Table 2.3-1 gives quantitative comparisons of the dimensionless velocities, where the percent values are given with respect to the common velocity scale U_o. Also, Tables 2.3-2 and 2.3-3 give the computed velocities at the same locations reported in Ghia et al. (1982). At this Reynolds number, in addition to the major central vortex, two minor vortices at the bottom corners were observed in the computations in agreement with Ghia et al. (1982) and Kim et al. (1985).

Table 2.3-1: Quantitative comparisons between the results given in Ghia et al. (1982) and our results using the same grid size

	rms of the relative difference	**max relative difference**
Horizontal velocities at $\bar{x} = 0.5$	0.19 %	0.30 %
Vertical velocities at $\bar{y} = 0.5$	0.62 %	0.39 %

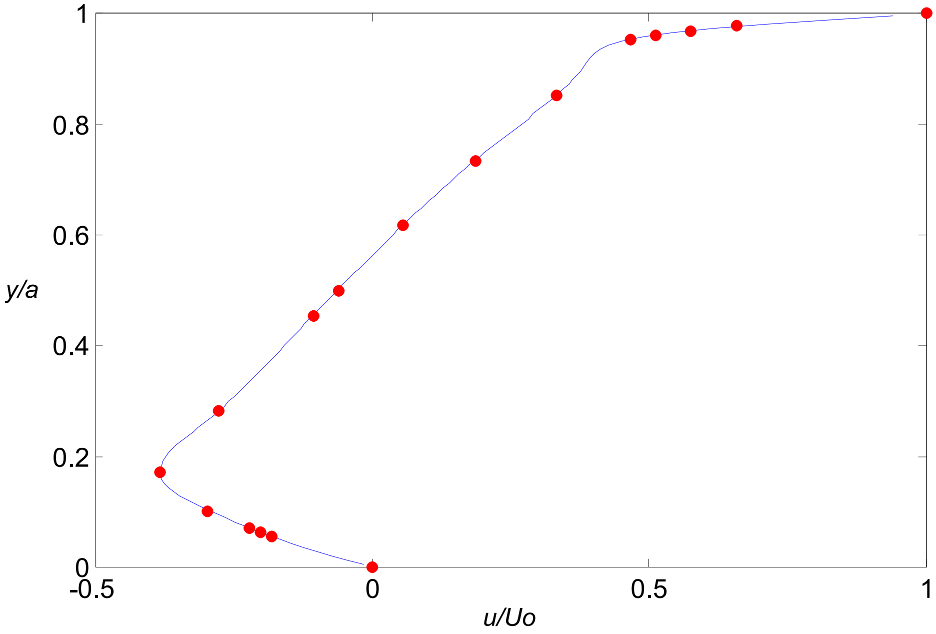

Figure 2.3-2: **Horizontal velocity profile at the plane $\bar{x} = 0.5$ for *Re* = 1000 using an Eulerian grid size of 129 x 129. The solid line is the computed solution, whereas the filled circles are Ghia et al. (1982)'s results.**

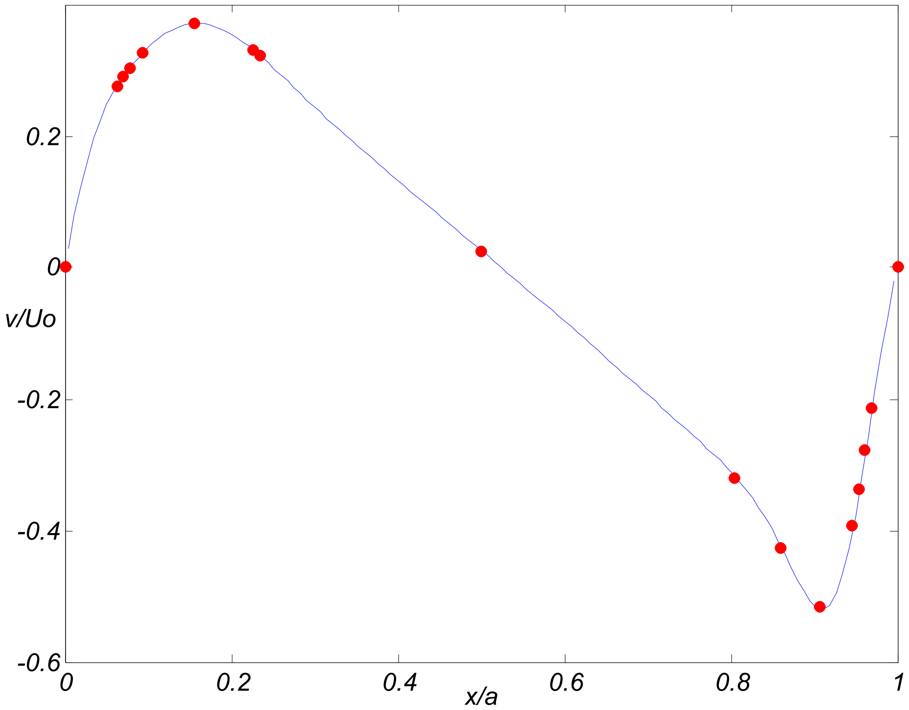

Figure 2.3-3: **Vertical velocity profile at the plane $\bar{y} = 0.5$ for *Re* = 1000 using an Eulerian grid size of 129 x 129. The solid line is the computed solution, whereas the filled circles are Ghia et al. (1982)'s results.**

Table 2.3-2: Computed horizontal velocity values at $\bar{x} = 0.5$, *Re* = 1000 using a 129 x 129 Eulerian grid size

$\bar{y}$	$\bar{u}$
0	0
0.0547	-0.17846
0.0625	-0.19908
0.0703	-0.21919
0.1016	-0.29486
0.1719	-0.38246
0.2813	-0.27806
0.4531	-0.10734
0.5000	-0.06172
0.6172	0.05605
0.7344	0.18631
0.8516	0.33264
0.9531	0.46815
0.9609	0.51329
0.9688	0.57768
0.9766	0.66168
1	1

Table 2.3-3: Computed vertical velocity values at $\bar{y} = 0.5$, *Re* = 1000 using a 129 x 129 Eulerian grid size

$\bar{x}$	$\bar{v}$
0	0
0.0625	0.27561
0.0703	0.29099
0.0781	0.30447
0.0938	0.32729
0.1563	0.37113
0.2266	0.33041
0.2344	0.32201
0.5000	0.02584
0.8047	-0.31721
0.8594	-0.42276
0.9063	-0.51819
0.9453	-0.40403
0.9531	-0.34967
0.9609	-0.28871
0.9688	-0.22369
1	0

Table 2.3-4 reports the relative differences in horizontal velocities at the plane $\bar{x} = 0.5$ with different grid resolutions, assuming the computed solution using a 257 x 257 Eulerian grid size is the true solution. Similarly, Table 2.3-5 reports the relative differences in vertical velocities at the plane $\bar{y} = 0.5$ with different grid resolutions. The percent values are given with respect to the common velocity scale U_o. The relative differences are respectively defined as

$$\bar{u} - \bar{u}_{\text{finest grid}}, \quad \bar{v} - \bar{v}_{\text{finest grid}}$$

Table 2.3-4: Relative differences in horizontal velocities *u*, at the plane $\bar{x} = 0.5$ with different grid resolutions, assuming the computed solution at the 257 x 257 Eulerian grid size is the true solution

Eulerian grid size	rms of the relative difference	max relative difference
33 x 33	3.87 %	7.01 %
65 x 65	1.31 %	2.13 %
129 x129	0.26 %	0.46 %

Table 2.3-5: Relative differences in vertical velocities *v*, at the plane $\bar{y} = 0.5$ with different grid resolutions, assuming the computed solution at the 257 x 257 Eulerian grid size is the true solution

Eulerian grid size	rms of the relative difference	max relative difference
33 x 33	5.14 %	8.82 %
65 x 65	1.69 %	2.83 %
129 x129	0.37 %	0.61 %

Note that, in Tables 2.3-4 and 2.3-5 the convergence rates are approximately second-order.

CHAPTER III
MODELING THE FLUID/STRUCTURE INTERACTION AND CLOTH MECHANICS

3.1 Introduction

3.1.1 Fluid/structure interaction models

The traditional approach for solving problems involving a deformable solid in a fluid flow is to first write the equations that describe the individual fluid and solid mechanics with the contact forces at their common interface, and then simultaneously solve them while applying the necessary initial and boundary conditions. These boundary conditions include constraints such as whether or not the fluid can flow/slip through the solid, and if so how it does so. These computations are classically done on two sets of grids, one for each element of the solid, and one for the fluid. To handle irregular geometries, these grids are usually unstructured. Such a method could be found in Chen et al. (2005). The major setbacks of these methods are in their expensive requirement to repeatedly regenerate the grids, finding the intersection of the solid and fluid grids to impose the proper boundary conditions on each grid, and iterating for a solution at every time step. This present study involves simulating several cloth pieces in moving water, so one would expect this classical approach's expensive computational burden to get even higher for modeling washing machine processes.

As an alternative, the Arbitrary Lagrangian Eulerian (ALE) method uses moving grids. As explained in Van Loon et al. (2007), in ALE method the grid points at the solid/fluid interface are set to move with the solid, so the rest of the fluid grid is deformed. The relative advantage of this method with respect to the traditional approaches is that the

ALE method avoids the requirement to find the intersection between the solid and fluid grids, because the interface is explicitly tracked. However, because the fluid grid next to the solid may deform unfavorably, the ALE method requires a nontrivial effort to smooth the grid deformations away from the solid and this process may get more difficult in the presence of multiple solids in fluid.

In the context of vortex methods, fluid-structure interaction can be modeled by placing material-bounded vortices on solid surfaces and shedding free vortices from sharp solid edges. The strengths of shed vortices are selected to satisfy interface constraints. There are many reported studies using this method, but to count a few: Krasny (1990) applied this method to model the vortex sheet roll-up due to the motion of a flat plate and Attar et al. (2003) used this method to model delta wings and flapping flags in fluid flow. Although these studies use an inviscid fluid model, vortex methods can also be applied to viscous flow simulations as shown in Yokota et al. (2007) and Zhao et al. (2007).

York et al. (2000) used the Material Point (MP) method for simulating the expansion of a pressurized membrane. The MP method uses moving Lagrangian points for advecting both the fluid and solid, while interpolating the solid and fluid properties on an Eulerian grid to solve the other necessary equations. The MP method is a relatively new method and lacks an extensive literature.

On the other hand, the Peskin (1972)’s Immersed Boundary (IB) method and its derivatives use a fixed Eulerian grid for the fluid and moving Lagrangian points for solids, approximating them as lower dimensional objects in space. The IB method works as follows: first it computes the elastic forces in the solids based on their current shapes, then it desingularizes solids’ elastic and inertial properties onto a higher dimensional space by approximate Dirac-delta functions, then it constructs a common equation for both the fluid and solids to be solved for a common velocity field, and finally it uses this common velocity field to move the solids to their new positions. No-slip and impenetrability conditions at the solid/fluid interfaces are automatically satisfied, since this method assumes a common fluid and solid velocity. Moreover, since both the solids and fluid use a common velocity field, the solids cannot penetrate into each other, at least for the well refined simulations. Generally speaking, the advantage of the IB method is in its substantial simplicity and cheaper computational cost with respect to the traditional fluid-structure interaction methods. With the IB method it is possible to use non-conforming structured Cartesian grids as the fixed Eulerian grid and this substantially eases the formulation by: allowing the use of regular stencils for the discrete equations, allowing the use of fast Geometric Multigrid methods for solving linear sets of discretized equations (as long as the solids do not have a large excess mass with respect to the fluid), and by keeping the computer code simple.

The Immersed Boundary (IB) method has been widely used for modeling complex flows involving flexible structures with irregular geometries. Some applications of the IB method that Peskin (2002) cites in his review paper include: heart modeling (Peskin (1972), Peskin (1977), Peskin et al. (1989), and McQueen et al. (2000)), platelet aggregation during blood clotting (Faucci et al. (1993)), swimming motions of eels, sperms, and bacteria (Faucci et al. (1988) and Faucci et al. (1995)), biofilm processes (Dillon et al. (1996)), flapping filaments (Zhu et al. (2002) and Zhu et al. (2003)) and many others. Moreover, Unverdi et al. (1992) and Tryggvason et al. (2001) used the principle of the IB method to model multiphase flows, in which the surface tension of the interface between two different fluids is desingularized on a higher dimensional space. In addition to flexible solids, the IB method has also been used to simulate fluid flows on Cartesian grids involving rigid solids with complex geometries, as will be discussed in Chapter 4.

As a disadvantage, the IB method suffers from low-order spatial accuracy because of its use of desingularized Dirac-delta functions. As an improvement, the Immersed Interface (II) method presented in LeVeque et al. (1997), Lee (2002), and Lee et al. (2003) overcomes this issue by reformulating the problem with interface jump conditions. In the framework of the IB method, the II method of Lee (2002) and Lee et al. (2003) abandons using distributed Dirac-delta functions for the interface normal direction and these studies show improved accuracies. Li et al. (2001) went one step further and totally dispensed the usage of the Dirac-delta functions, but their algorithm is no longer a 'simple' patch to the original IB method. The drawback of the II method is the solids' inertial effects can no longer be represented on the fixed Eulerian grid as an added mass, but are included in the interface forces as d'Alembert forces (at least in the interface normal direction). Such a formulation requires guessing/iterating for the velocity of the interface at the next time step before formulating the jump conditions, creating inconveniencies.

As another drawback, both the IB and II methods suffer from numerical stiffness for problems involving stiff solids and require much smaller time steps than the standard CFL (Courant-Friedrichs-Lewy) restriction. Stockie et al. (1999) made the linear stability analysis of the IB method and concluded that Runge-Kutta methods are better suited for this problem for explicit time-marching formulations. Following earlier attempts, LeVeque et al. (1997), Lee (2002) and Lee et al. (2003) suggest a semi-Newtonian implicit method for time-marching.

The Immersed Boundary method has been selected as the main solution algorithm for this study. The amount of the literature, presence of three-dimensional versions, and most importantly, its simplicity are the reasons why it has been selected.

3.1.2 Cloth models

The mechanical modeling of cloth pieces has been of interest in a diverse range of applications. For instance, the computer graphics community has been using cloth models to incorporate them into the animation movies and computer games (Terzopoulos et al. (1987), House et al. (1996), Baraff et al. (1998), Bridson et al. (2003)). Although most of them have used physical principals in their models, they are not restricted to do so as long as their outputs are 'realistic', as Breen et al. (1994) and Gibson et al. (1997) mention in their papers. Within the engineering community, especially textile engineers have been studying cloth mechanical behavior (Chen et al. (1995), Zhao et al. (1997), Mingxiang et al. (1998), Yu et al. (2000), and Kang et al. (2004)).

This study uses an elastic plate model that can simulate large cloth deformations with small strains. The literature on elastic plates is vast, but there are two main classes of elastic plate models depending on whether or not the through-thickness (transverse) shear deformations are modeled. These plate models are shortcuts to a complete three-dimensional elastic model. The first class of models assumes the plates to be very thin with respect to their length and width dimensions and neglects their transverse shear deformations. This assumption is sometimes called as the Kirchhoff-Love hypothesis. Although there are many models of this class, Pai et al. (1992) quotes from Koiter (1960) saying that these models cannot be substantially different from each other unless traverse shear deformations are taken into account. The second class of plate models makes low-order approximations to the through-thickness shear deformation and is sometimes referred as the Mindlin-Reissner formulations. Since cloth thicknesses are very small compared to their other dimensions, this present study uses a Kirchoff-Love type of a plate formulation, similar to the models presented in Love (1944) and Cerda et al. (2005).

3.1.3 Organization

In this chapter first the Immersed Boundary method for modeling the fluid/structure interaction will be presented. Next, a large-deformation/small-strain, isotropic, and elastic model for the cloth mechanics will be derived. This will be followed by some verification studies including capturing the frequencies of a vibrating plate, capturing the static deformed shape of a heavy cantilever beam, and comparing the model with the recorded fluttering motion of a plate as it descends in an initially still water under its own weight.

3.2 The Immersed Boundary Method for modeling the fluid/structure interaction

This discussion is a summary of the Immersed Boundary method developed by Peskin (1972), which models the coupled fluid and solid dynamics. The Navier-Stokes equations for an incompressible Newtonian fluid are written as

$$\rho_f\left(\frac{\partial \mathbf{u}(\mathbf{x},t)}{\partial t}+\mathbf{u}(\mathbf{x},t)\circ\nabla\mathbf{u}(\mathbf{x},t)\right)=-\nabla p(\mathbf{x},t)+\mu\nabla^2\mathbf{u}(\mathbf{x},t)+\mathbf{i}(\mathbf{x},t)+\mathbf{w}_f(\mathbf{x},t) \qquad \textbf{(3.2-1)}$$

$$\nabla\circ\mathbf{u}(\mathbf{x},t)=0 \qquad \textbf{(3.2-2)}$$

In these equations **x** is the current position, t is the time, ρ_f is the fluid mass density, μ is the fluid viscosity, **u** is the fluid velocity, p is the pressure, $\mathbf{w}_f$ is the external body force (e.g. weight) acting on the fluid excluding the interface forces due to immersed solids which are denoted by **i**. On the other hand, for the immersed solids one can write

$$\frac{1}{K}\rho_s\frac{D\mathbf{U}(\mathbf{x_0},t)}{Dt}=\mathbf{F}(\mathbf{x_0},t)-\mathbf{I}(\mathbf{x_0},t)+\mathbf{W}_s(\mathbf{x_0},t) \qquad \textbf{(3.2-3)}$$

$$\frac{D\mathbf{X}(\mathbf{x_0},t)}{Dt}=\mathbf{U}(\mathbf{x_0},t) \qquad \textbf{(3.2-4)}$$

In these equations ρ_s is the undeformed solid mass density, K is the Jacobian of the solid deformation (such that $\rho_s=\rho_{sc}K$, where ρ_{sc} is the deformed solid mass density), **U** is the solid velocity, **X** is the solid current position parameterized in terms of local coordinates $\mathbf{x_0}$ attached onto the solid at its hypothetical reference position, **F** is the solid's internal forces (due to elastic and plastic effects), and $\mathbf{W}_s$ represents the external body forces (e.g. weight) except the interface forces –**I** at the solid/fluid interface. If one idealizes the solids as lower dimensional objects (e.g. curves in $\mathbf{R}^2$ or $\mathbf{R}^3$, surfaces in $\mathbf{R}^3$) then the solids can be represented with Dirac-delta functions in a higher dimensional space. Specifically, for a lower dimensional solid in $\mathbf{R}^\mathbf{m}$ we rephrase Eqn. (3.2-3) in a higher dimension $\mathbf{R}^\mathbf{n}$ as

$$\begin{aligned}\int\frac{1}{K}\rho_s\frac{D\mathbf{U}(\mathbf{x_0},t)}{Dt}\delta^*\left(\mathbf{x}-\mathbf{X}(\mathbf{x_0},t)\right)K\,d\mathbf{x_0}&=\int\left(\mathbf{F}(\mathbf{x_0},t)+\mathbf{W}_s(\mathbf{x_0},t)\right)\delta^*\left(\mathbf{x}-\mathbf{X}(\mathbf{x_0},t)\right)K\,d\mathbf{x_0}\\&\quad-\int\mathbf{I}(\mathbf{x_0},t)\delta^*\left(\mathbf{x}-\mathbf{X}(\mathbf{x_0},t)\right)K\,d\mathbf{x_0}\end{aligned}$$

$$\textbf{(3.2-5)}$$

$$\mathbf{x_o} \in \mathbf{R^m}, \quad \{\mathbf{x}, \ \mathbf{X}\} \in \mathbf{R^n}$$

where

$$\delta^*\left(\mathbf{x}-\mathbf{X}(\mathbf{x_o},t)\right) \equiv \delta\left(x_1 - X_1(\mathbf{x_o},t)\right)\delta\left(x_2 - X_2(\mathbf{x_o},t)\right)...\delta\left(x_n - X_n(\mathbf{x_o},t)\right)$$

and δ is the Dirac-delta function. The term $K\, d\mathbf{x_o}$ is the infinitesimal unit length/area/volume/… of the lower dimensional deformed solid.

To clarify this process, think about a three-dimensional space-curve parameterized by its arclength s, such as

$$\mathbf{X} = \mathbf{X}(s), \quad s \in \mathbf{R}, \quad \mathbf{X} \in \mathbf{R^3}$$

Next, imagine this curve has a mass, and its associated mass density (mass per unit length) is given by $\rho(s)$. With the same process described above, in a three-dimensional space this mass density could be represented as

$$\rho_{3D}(\mathbf{x}) = \int \rho(s)\ \delta\left(x - X(s)\right)\delta\left(y - Y(s)\right)\delta\left(z - Z(s)\right) ds$$

Turning back to the main discussion, the following is true because of Newton's third law

$$-\mathbf{i}\left(\mathbf{x}\big|_{\mathbf{x}=\mathbf{X}}, t\right) = -\int \mathbf{I}(\mathbf{x_o},t)\ \delta^*\left(\mathbf{x}-\mathbf{X}(\mathbf{x_o},t)\right) K\, d\mathbf{x_o} \tag{3.2-6}$$

which states that the interface forces acting on the solid and on the fluid should be same in magnitude but opposite in direction. Using Eqns. (3.2-5), (3.2-6), and (3.2-1) one finds

$$\rho_f\left(\frac{\partial \mathbf{u}(\mathbf{x},t)}{\partial t} + \mathbf{u}(\mathbf{x},t)\circ\nabla\mathbf{u}(\mathbf{x},t)\right) = -\nabla p(\mathbf{x},t) + \mu\nabla^2\mathbf{u}(\mathbf{x},t) + \mathbf{f}(\mathbf{x},t) + \mathbf{w}_f(\mathbf{x},t) \tag{3.2-7}$$

where

$$\mathbf{f}\left(\mathbf{x}\big|_{\mathbf{x}=\mathbf{X}},t\right)=\int\left(\mathbf{F}\left(\mathbf{x_o},t\right)+\mathbf{W}_s\left(\mathbf{x_o},t\right)-\frac{1}{K}\rho_s\frac{D\mathbf{U}\left(\mathbf{x_o},t\right)}{Dt}\right)\delta^*\left(\mathbf{x}-\mathbf{X}\left(\mathbf{x_o},t\right)\right)K\,d\mathbf{x_o} \tag{3.2-8}$$

If the solid is assumed to be impermeable and there is no slip between the solid and fluid one can write

$$\mathbf{U}\left(\mathbf{x_o},t\right)=\mathbf{u}\left(\mathbf{x}\big|_{\mathbf{x}=\mathbf{X}},t\right)$$

or

$$\mathbf{U}\left(\mathbf{x_o},t\right)=\int\mathbf{u}\left(\mathbf{x},t\right)\delta^*\left(\mathbf{x}-\mathbf{X}\left(\mathbf{x_o},t\right)\right)d\mathbf{x} \tag{3.2-9}$$

As a summary, the following set of equations can model the fluid-structure interaction between an *m* dimensional solid and an *n* dimensional fluid;

$$\rho_f\left(\frac{\partial\mathbf{u}\left(\mathbf{x},t\right)}{\partial t}+\mathbf{u}\left(\mathbf{x},t\right)\circ\nabla\mathbf{u}\left(\mathbf{x},t\right)\right)=-\nabla p\left(\mathbf{x},t\right)+\mu\nabla^2\mathbf{u}\left(\mathbf{x},t\right)+\mathbf{f}\left(\mathbf{x},t\right)+\mathbf{w}_f\left(\mathbf{x},t\right) \tag{3.2-10}$$

$$\nabla\circ\mathbf{u}\left(\mathbf{x},t\right)=0 \tag{3.2-11}$$

$$\mathbf{f}\left(\mathbf{x},t\right)=\int\left(\mathbf{F}\left(\mathbf{x_o},t\right)+\mathbf{W}_s\left(\mathbf{x_o},t\right)-\frac{1}{K}\rho_s\frac{D\mathbf{U}\left(\mathbf{x_o},t\right)}{Dt}\right)\delta^*\left(\mathbf{x}-\mathbf{X}\left(\mathbf{x_o},t\right)\right)K\,d\mathbf{x_o} \tag{3.2-12}$$

$$\mathbf{U}\left(\mathbf{x_o},t\right)=\int\mathbf{u}\left(\mathbf{x},t\right)\;\delta^*\left(\mathbf{x}-\mathbf{X}\left(\mathbf{x_o},t\right)\right)d\mathbf{x} \tag{3.2-13}$$

$$\frac{D\mathbf{X}\left(\mathbf{x_o},t\right)}{Dt}=\mathbf{U}\left(\mathbf{x_o},t\right) \tag{3.2-14}$$

Eqns. (3.2-10)-(3.2-14) are also called the Immersed Boundary method equations, first developed by Peskin in 1972 and applied to heart simulations.

As stated earlier, the term **F** in Eqn. (3.2-12) represents the internal forces in the solid. For a rigid body the internal forces cancel out each other at every point in the solid, but for an elastic solid they might not. Our scope in this research is the deformable solid curves and surfaces, so in the next section we will present the elastic models.

3.3 Solid Modeling

3.3.1 Three-dimensional elastic solids

This discussion states some results from the study of the continuum mechanics, and interested readers could refer to Malvern (1969) or Fung (1965) to view their detailed derivations and discussions.

For finite deformations the Lagrangian (finite deformation/Green) strain tensor, **E**, is given as

$$E_{ij}\left(\mathbf{x_o},t\right)=\frac{1}{2}\left(\frac{\partial X_k}{\partial x_{oi}}\frac{\partial X_k}{\partial x_{oj}}-\delta_{ij}\right) \tag{3.3-1}$$

where δ is the Kronecker delta. This strain tensor represents the state of deformation of the solid with respect to an unstrained reference state $\mathbf{x_o}$. As stated earlier $\mathbf{X} = (X_1, X_2, X_3) = (X, Y, Z)$ represents the current position of the solid.

Having defined a strain measure, the strains are related to stresses through a constitutive model. If the solid is assumed to have small strains even if it deforms largely, a linear stress-strain model can be used. In an index form such a relation can be written as

$$S_{ij} = C_{ijkl}E_{kl} \tag{3.3-2}$$

where **S** is a symmetric stress tensor (sometimes called the 2nd Piola stress or Kirchhoff's stress), which is defined on the reference state $\mathbf{x_o}$, and **C** is a 4th order elasticity tensor which can theoretically have 81 entities (in a three-dimensional space) but could be shown to have only 21 independent terms if a strain energy potential is assumed to exist. Furthermore, if the solid is assumed to be isotropic there would be only two independent terms in **C** and the general linear stress strain relationship given in Eqn. (3.3-2) can be rewritten as

$$S_{ij} = \lambda E_{kk}\delta_{ij} + 2GE_{ij} \tag{3.3-3}$$

In this equation λ and G are the so-called 'Lame's constants' which are given as

$$\lambda = \frac{\overline{E}\,\nu}{(1+\nu)(1-2\nu)} \quad , \quad G = \frac{\overline{E}}{2(1+\nu)} \tag{3.3-4}$$

where $\overline{E}$ is the material's 'Young modulus' and ν is the material's 'Poisson's ratio'.

The conservation of linear momentum, relating solid's motion to its state of loading, is

$$\frac{1}{K}\rho_s \frac{D^2 X_i}{Dt^2} = \frac{1}{K}\frac{\partial}{\partial x_{oj}}\left(S_{jk}\frac{\partial X_i}{\partial x_{ok}} \right) - I_i + W_{si} \tag{3.3-5}$$

Similar to Eqn. (3.2-3), W_{si} is the external body force acting on the solid except the forces applied by the fluid on the solid which are contained in I_i and K is the Jacobian of the solid deformation (such that $\rho_s = \rho_{sc} K$, where ρ_{sc} is the deformed solid mass density) . Comparing Eqn. (3.2-3) with Eqn. (3.3-5) reveals the following relationship for **F** in (3.2-3)

$$F_i(x_o, t) = \frac{1}{K}\frac{\partial}{\partial x_{oj}}\left(S_{jk}\frac{\partial X_i}{\partial x_{ok}} \right) \tag{3.3-6}$$

Having formulated a model for three-dimensional, linearly elastic, and isotropic solids undergoing finite deformations but small strains, the next sections will discuss some lower dimensional models for 2D surfaces in a 3D space (for three-dimensional washing machine simulations) and 1D fibers in a 2D space (for two-dimensional washing machine simulations). Note that, a 1D fiber in a 2D space cannot undergo torsion, but by adding this elastic effect to the present 1D fiber / 2D space formulation and by updating the lower dimensional curvature expressions one might as well model a 1D fiber in a 3D space.

3.3.2 Two-dimensional elastic membranes

Two-dimensional membranes are solid surfaces that can resist stretching and in-plane shearing, but lack bending and torsional stiffness. In this development, a surface patch **X** is parameterized with respect to *s* and *r* as

$$\mathbf{X} = \mathbf{X}(s, r)$$

so the infinitesimal distance vector between any two neighboring points could be approximated as

$$d\mathbf{X} = \frac{\partial \mathbf{X}}{\partial s}\delta s + \frac{\partial \mathbf{X}}{\partial r}\delta r$$

and the square of the magnitude of this distance vector is

$$d\mathbf{X}^2 = d\mathbf{X} \circ d\mathbf{X} = \frac{\partial \mathbf{X}}{\partial s} \circ \frac{\partial \mathbf{X}}{\partial s}(\delta s)^2 + \frac{\partial \mathbf{X}}{\partial s} \circ \frac{\partial \mathbf{X}}{\partial r} 2(\delta s)(\delta r) + \frac{\partial \mathbf{X}}{\partial r} \circ \frac{\partial \mathbf{X}}{\partial r}(\delta r)^2$$

If one chooses *s* and *r* such that at a hypothetical reference position $\mathbf{x_o}$ constant *s* and *r* lines are arclength parameters on two orthogonal directions, then the last expression on the reference state reduces to

$$d\mathbf{X}_{original}{}^2 = (\delta s)^2 + (\delta r)^2$$

and consequently one can write

$$d\mathbf{X}^2 - d\mathbf{X}_{original}{}^2 = \left(\frac{\partial \mathbf{X}}{\partial s}\circ\frac{\partial \mathbf{X}}{\partial s}-1\right)(\delta s)^2 + \left(\frac{\partial \mathbf{X}}{\partial s}\circ\frac{\partial \mathbf{X}}{\partial r}\right)2(\delta s)(\delta r) + \left(\frac{\partial \mathbf{X}}{\partial r}\circ\frac{\partial \mathbf{X}}{\partial r}-1\right)(\delta r)^2$$

which is a standard deformation measure in solid mechanics. The Lagrangian strain tensor defined in Eqn. (3.3-1) could be rewritten as

$$d\mathbf{X}^2 - d\mathbf{X}_{original}{}^2 = 2E_{ij}\left(\delta x_i\right)\left(\delta x_j\right)$$

so

$$\mathbf{E} = \frac{1}{2}\begin{pmatrix} \left(\frac{\partial X}{\partial s}\right)^2 + \left(\frac{\partial Y}{\partial s}\right)^2 + \left(\frac{\partial Z}{\partial s}\right)^2 - 1 & \left(\frac{\partial X}{\partial s}\frac{\partial X}{\partial r} + \frac{\partial Y}{\partial s}\frac{\partial Y}{\partial r} + \frac{\partial Z}{\partial s}\frac{\partial Z}{\partial r}\right) \\ \left(\frac{\partial X}{\partial s}\frac{\partial X}{\partial r} + \frac{\partial Y}{\partial s}\frac{\partial Y}{\partial r} + \frac{\partial Z}{\partial s}\frac{\partial Z}{\partial r}\right) & \left(\frac{\partial X}{\partial r}\right)^2 + \left(\frac{\partial Y}{\partial r}\right)^2 + \left(\frac{\partial Z}{\partial r}\right)^2 - 1 \end{pmatrix} \qquad \textbf{(3.3-7)}$$

On the other hand, for the plane-stress state of an isotropic solid, Hooke's law relating the stresses to strains is given as

$$\begin{pmatrix} S_{11} \\ S_{22} \\ S_{12} \end{pmatrix} = \frac{\overline{E}}{1-\nu^2}\begin{pmatrix} 1 & \nu & 0 \\ \nu & 1 & 0 \\ 0 & 0 & 1-\nu \end{pmatrix}\begin{pmatrix} E_{11} \\ E_{22} \\ E_{12} \end{pmatrix} \qquad \textbf{(3.3-8)}$$

where **S** is the 2nd Piola stress or Kirchhoff's stress, which is defined on the solid's hypothetical reference state. Note that stresses computed by Eqns. (3.3-7) and (3.3-8) are only in-plane stresses, standing for the solid surface's resistance to stretch and in-plane shear. For two-dimensional elastic membranes these stresses are assumed to be uniform through solid thickness *q*, so a 'two-dimensional stress resultant' could be defined by integrating these stresses through the solid thickness. Finally, the divergence of these stress resultants is computed through Eqn. (3.3-6), which are then used with the solid's linear momentum equation Eqn. (3.3-5) or in Eqn. (3.2-12) with the IB method.

3.3.3 Two-dimensional elastic plates

In addition to solid's in-plane elastic resistance to stretch and in-plane shear, it is desirable to model out-of-plane effects such as its stiffness to bending and torsion. To do so, it is necessary to digress from the previous assumption that the solid had an infinitesimal thickness. Instead of using the full three-dimensional elasticity equations, an approximate and simplified thin plate model will be presented. This model is from Love (1944) and the presentation sometimes uses the notation of Cerda et al. (2005). It assumes:

1. The solid has a constant thickness,
2. The solid is very thin compared to its length and width,
3. The solid thickness is much smaller than its minimum radius of curvature,
4. Although the deformations are large, strains are small and Hooke's law still applies,
5. Normal planes to the solid element's middle-surface stay normal as the solid deforms,
6. The mass moments of inertia of the through thickness cross-sections are negligible (which is shown to be true if the velocities of the bending deformations are slower than the velocity of the plate natural frequencies)

Assume the solid is not stressed at a hypothetical flat reference state. As before, the solid element's middle-surface at this reference state is parameterized with *s* and *r*, which are the arclength parameters of the constant *r* and *s* lines, respectively. Again, these constant *r* and *s* lines are orthogonal to each other everywhere at this reference state. This surface is extruded to form a solid volume with a thickness *h*. Tangent vectors $\mathbf{e}_1$ and $\mathbf{e}_2$ are defined parallel to the constant *r* and *s* lines, respectively. The surface normal vector $\mathbf{e}_3$ is defined as

$$\mathbf{e}_3 = \mathbf{e}_1 \times \mathbf{e}_2 \qquad \textbf{(3.3-9)}$$

so **(e₁, e₂, e₃)** form a right handed local coordinate system. Figure 3.3-1 shows an arbitrarily deformed surface patch. The area of this surface patch is given as

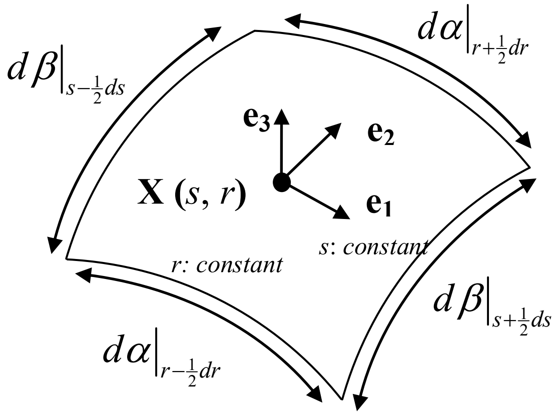

Figure 3.3-1: An arbitrarily deformed surface patch

$$dA = \left|\mathbf{e}_1 \times \mathbf{e}_2\right| ds\,dr = K\,ds\,dr \tag{3.3-10}$$

where

$$K = \left(\left|\frac{\partial \mathbf{X}}{\partial s}\right|^2 \left|\frac{\partial \mathbf{X}}{\partial r}\right|^2 - \left(\frac{\partial \mathbf{X}}{\partial s} \circ \frac{\partial \mathbf{X}}{\partial r}\right)^2 \right)^{1/2} \tag{3.3-11}$$

Define an arbitrary point **O** on the middle-surface of the shell as

$$\mathbf{X}_\mathbf{O} = \mathbf{X}_\mathbf{O}\left(s,r\right)$$

and a point **A** which is at a distance z away from the point **O** along the $\mathbf{e}_3$ direction as

$$\mathbf{X}_\mathbf{A} = \mathbf{X}_\mathbf{O}\left(s,r\right) + z\,\mathbf{e}_3\left(s,r\right) \tag{3.3-12}$$

Any neighboring point **A’** to **A** could be described as

$$\mathbf{X}_{\mathbf{A'}} = \mathbf{X}_{\mathbf{O}}\left(s+\delta s, r+\delta r\right) + \left(z+\delta z\right)\mathbf{e}_3\left(s+\delta s, r+\delta r\right)$$

Using Taylor series one can write

$$\mathbf{X}_{\mathbf{O}}\left(s+\delta s, r+\delta r\right) = \mathbf{X}_{\mathbf{O}}\left(s,r\right) + \frac{\partial \mathbf{X}}{\partial s}\delta s + \frac{\partial \mathbf{X}}{\partial r}\delta r + \ldots$$

$$\mathbf{e}_3\left(s+\delta s, r+\delta r\right) = \mathbf{e}_3\left(s,r\right) + \frac{\partial \mathbf{e}_3}{\partial s}\delta s + \frac{\partial \mathbf{e}_3}{\partial r}\delta r + \ldots$$

and consequently

$$\mathbf{dX}_{\mathbf{A}} = \mathbf{X}_{\mathbf{A'}} - \mathbf{X}_{\mathbf{A}} = \frac{\partial \mathbf{X}}{\partial s}\delta s + \frac{\partial \mathbf{X}}{\partial r}\delta r + z\left(\frac{\partial \mathbf{e}_3}{\partial s}\delta s + \frac{\partial \mathbf{e}_3}{\partial r}\delta r\right) + \mathbf{e}_3\delta z + \ldots$$

So the square of the distance between the neighboring points **A** and **A’** could be found as

$$\begin{aligned}
\mathbf{dX}_{\mathbf{A}}{}^{2} = \mathbf{dX}_{\mathbf{A}} \circ \mathbf{dX}_{\mathbf{A}} = {} & \left(\frac{\partial \mathbf{X}}{\partial s} \circ \frac{\partial \mathbf{X}}{\partial s}\right)\left(\delta s\right)^2 + 2\left(\frac{\partial \mathbf{X}}{\partial s} \circ \frac{\partial \mathbf{X}}{\partial r}\right)\left(\delta s\right)\left(\delta r\right) + \left(\frac{\partial \mathbf{X}}{\partial r} \circ \frac{\partial \mathbf{X}}{\partial r}\right)\left(\delta r\right)^2 \\
& + 2z\left(\frac{\partial \mathbf{X}}{\partial s} \circ \frac{\partial \mathbf{e}_3}{\partial s}\right)\left(\delta s\right)^2 + 2z\left(\frac{\partial \mathbf{X}}{\partial r} \circ \frac{\partial \mathbf{e}_3}{\partial r}\right)\left(\delta r\right)^2 \\
& + 2z\left(\frac{\partial \mathbf{X}}{\partial s} \circ \frac{\partial \mathbf{e}_3}{\partial r} + \frac{\partial \mathbf{X}}{\partial r} \circ \frac{\partial \mathbf{e}_3}{\partial s}\right)\left(\delta s\right)\left(\delta r\right) + z^2\left(\frac{\partial \mathbf{e}_3}{\partial s} \circ \frac{\partial \mathbf{e}_3}{\partial s}\right)\left(\delta s\right)^2 \\
& + 2z^2\left(\frac{\partial \mathbf{e}_3}{\partial s} \circ \frac{\partial \mathbf{e}_3}{\partial r}\right)\left(\delta s\right)\left(\delta r\right) + z^2\left(\frac{\partial \mathbf{e}_3}{\partial r} \circ \frac{\partial \mathbf{e}_3}{\partial r}\right)\left(\delta r\right)^2 \\
& + 2\left(\frac{\partial \mathbf{X}}{\partial s} \circ \mathbf{e}_3\right)\left(\delta s\right)\left(\delta z\right) + 2\left(\frac{\partial \mathbf{X}}{\partial r} \circ \mathbf{e}_3\right)\left(\delta r\right)\left(\delta z\right) + \\
& + 2z\left(\frac{\partial \mathbf{e}_3}{\partial s} \circ \mathbf{e}_3\right)\left(\delta s\right)\left(\delta z\right) + 2z\left(\frac{\partial \mathbf{e}_3}{\partial r} \circ \mathbf{e}_3\right)\left(\delta r\right)\left(\delta z\right) + \left(\delta z\right)^2 + \ldots
\end{aligned}$$

(3.3-13)

Since tangent vectors $\mathbf{e_1}$ and $\mathbf{e_2}$ are respectively defined to be parallel to the constant r and s lines, they can be written as

$$\mathbf{e}_1 = \frac{\partial \mathbf{X}}{\partial s} \Big/ \left| \frac{\partial \mathbf{X}}{\partial s} \right| \tag{3.3-14}$$

$$\mathbf{e}_2 = \frac{\partial \mathbf{X}}{\partial r} \Big/ \left| \frac{\partial \mathbf{X}}{\partial r} \right| \tag{3.3-15}$$

Note that $\mathbf{e_3}$ was given with Eqn. (3.3-9). Using the following definitions of normal curvatures κ_s and κ_r of the constant r and s lines respectively,

$$\begin{aligned} \kappa_s &= \left(\frac{\partial \mathbf{e_1}}{\partial s} \circ \mathbf{e_3} \right) \Big/ \left| \frac{\partial \mathbf{X}}{\partial s} \right| \\ \kappa_r &= \left(\frac{\partial \mathbf{e_2}}{\partial r} \circ \mathbf{e_3} \right) \Big/ \left| \frac{\partial \mathbf{X}}{\partial r} \right| \end{aligned} \tag{3.3-16}$$

and noting that the vectors $\mathbf{e_1}$ and $\mathbf{e_2}$ are orthogonal to $\mathbf{e_3}$, the following results hold true

$$\begin{aligned}
&(\mathbf{e} \circ \mathbf{e}) = 1 \Rightarrow \left(\mathbf{e} \circ \frac{\partial \mathbf{e}}{\partial s} \right) = 0, \quad \left(\mathbf{e} \circ \frac{\partial \mathbf{e}}{\partial r} \right) = 0 \\
&(\mathbf{e_i} \circ \mathbf{e_3})_{\mathbf{i} \neq 3} = 0 \Rightarrow \left(\mathbf{e_i} \circ \frac{\partial \mathbf{e_3}}{\partial s} \right) = -\left(\mathbf{e_3} \circ \frac{\partial \mathbf{e_i}}{\partial s} \right), \quad \left(\mathbf{e_i} \circ \frac{\partial \mathbf{e_3}}{\partial r} \right) = -\left(\mathbf{e_3} \circ \frac{\partial \mathbf{e_i}}{\partial r} \right) \\
&\left(\frac{\partial \mathbf{X}}{\partial s} \circ \frac{\partial \mathbf{e_3}}{\partial s} \right) = \left| \frac{\partial \mathbf{X}}{\partial s} \right| \left(\mathbf{e_1} \circ \frac{\partial \mathbf{e_3}}{\partial s} \right) = -\left| \frac{\partial \mathbf{X}}{\partial s} \right| \left(\frac{\partial \mathbf{e_1}}{\partial s} \circ \mathbf{e_3} \right) = -\left| \frac{\partial \mathbf{X}}{\partial s} \right|^2 \kappa_s \\
&\left(\frac{\partial \mathbf{X}}{\partial r} \circ \frac{\partial \mathbf{e_3}}{\partial r} \right) = \left| \frac{\partial \mathbf{X}}{\partial r} \right| \left(\mathbf{e}_2 \circ \frac{\partial \mathbf{e_3}}{\partial r} \right) = -\left| \frac{\partial \mathbf{X}}{\partial r} \right| \left(\frac{\partial \mathbf{e}_2}{\partial r} \circ \mathbf{e_3} \right) = -\left| \frac{\partial \mathbf{X}}{\partial r} \right|^2 \kappa_r \\
&\left(\frac{\partial \mathbf{X}}{\partial s} \circ \frac{\partial \mathbf{e_3}}{\partial r} \right) = -\left(\frac{\partial^2 \mathbf{X}}{\partial r \partial s} \circ \mathbf{e_3} \right) \\
&\left(\frac{\partial \mathbf{X}}{\partial r} \circ \frac{\partial \mathbf{e_3}}{\partial s} \right) = -\left(\frac{\partial^2 \mathbf{X}}{\partial r \partial s} \circ \mathbf{e_3} \right)
\end{aligned}$$

In these equations the term $\left(\dfrac{\partial^2 \mathbf{X}}{\partial r \partial s} \circ \mathbf{e_3} \right)$ is related to the geodesic torsion of the deformed plate. In this development the plate is assumed to be very thin so terms of order z^2 and higher will be ignored in Eqn. (3.3-13). Furthermore, terms of order greater than δ^2 will be neglected, since the distance between point **A** and **A’** is infinitesimal. Using the results that we just stated, Eqn. (3.3-13) simplifies into

$$\begin{aligned}\mathbf{dX_A}^2 = \mathbf{dX_A} \circ \mathbf{dX_A} \approx & \left(\frac{\partial \mathbf{X}}{\partial s} \circ \frac{\partial \mathbf{X}}{\partial s} \right) (\delta s)^2 + 2 \left(\frac{\partial \mathbf{X}}{\partial s} \circ \frac{\partial \mathbf{X}}{\partial r} \right) (\delta s)(\delta r) + \left(\frac{\partial \mathbf{X}}{\partial r} \circ \frac{\partial \mathbf{X}}{\partial r} \right) (\delta r)^2 \\ & - 2 z \kappa_s \left| \frac{\partial \mathbf{X}}{\partial s} \right|^2 (\delta s)^2 - 2 z \kappa_r \left| \frac{\partial \mathbf{X}}{\partial r} \right|^2 (\delta r)^2 - 4 z \left(\frac{\partial^2 \mathbf{X}}{\partial r \partial s} \circ \mathbf{e_3} \right) (\delta s)(\delta r) + (\delta z)^2\end{aligned}$$

Since *s* and *r* are selected as arclength parameters on two orthogonal lines on the unstressed and flat reference configuration

$$\mathbf{dX_A}^2 \Big|_{original} = (\delta s)^2 + (\delta r)^2 + (\delta z)^2$$

So the change in the square of length between infinitesimal points **A** and **A’** as the solid deforms from the unstressed reference position could be expressed as

$$\begin{aligned}\mathbf{dX_A}^2 - \mathbf{dX_A}^2 \Big|_{original} \approx & \left(\frac{\partial \mathbf{X}}{\partial s} \circ \frac{\partial \mathbf{X}}{\partial s} - 1 - 2 z \kappa_s \left| \frac{\partial \mathbf{X}}{\partial s} \right|^2 \right) (\delta s)^2 + \left(\frac{\partial \mathbf{X}}{\partial r} \circ \frac{\partial \mathbf{X}}{\partial r} - 1 \ - 2 z \kappa_r \left| \frac{\partial \mathbf{X}}{\partial r} \right|^2 \right) (\delta r)^2 \\ & + \left(\frac{\partial \mathbf{X}}{\partial s} \circ \frac{\partial \mathbf{X}}{\partial r} - 2 z \frac{\partial^2 \mathbf{X}}{\partial r \partial s} \circ \mathbf{e_3} \right) 2 (\delta s)(\delta r)\end{aligned}$$

(3.3-17)

Note that, point **A** is assumed to always lie along the $\mathbf{e_3}$ direction with respect to the point **O** on the middle-surface (through Eqn. (3.3-12)). In other words, normal planes to the middle-plane are assumed to stay normal as the solid deforms, which is the Kirchhoff-Love hypothesis. The Lagrangian strain tensor at point **A** is given as

$$\mathbf{dX_A}^2 - \mathbf{dX_A}^2\Big|_{original} = 2E_{ij}\left(\delta x_i\right)\left(\delta x_j\right)$$

where x_i's are the coordinates of the undeformed reference position (note that we selected x_1 as s and x_2 as r). On the other hand, the Almansi or Eulerian strain tensor at point **A**, which is defined in terms of the current configuration, is given as

$$\mathbf{dX_A}^2 - \mathbf{dX_A}^2\Big|_{original} = 2e_{ij}\left(\delta X_i\right)\left(\delta X_j\right)$$

where X_i's are the coordinates of the current position. The constant r and s lines on the deformed surface are respectively re-parameterized with arclength variables α and β as

$$\begin{aligned} \delta\alpha &= \left|\frac{\partial \mathbf{X}}{\partial s}\right| \delta s \\ \delta\beta &= \left|\frac{\partial \mathbf{X}}{\partial r}\right| \delta r \end{aligned} \qquad \textbf{(3.3-18)}$$

So the change in the square of length between infinitesimal points **A** and **A'** as the solid deforms from the unstressed flat reference position can be re-expressed with current position variables α and β as

$$\begin{aligned} \mathbf{dX_A}^2 - \mathbf{dX_A}^2\Big|_{original} &\approx \left(1 - 1\Big/\left|\frac{\partial \mathbf{X}}{\partial s}\right|^2 - 2z\kappa_s\right)\left(\delta\alpha\right)^2 + \left(1 - 1\Big/\left|\frac{\partial \mathbf{X}}{\partial r}\right|^2 - 2z\kappa_r\right)\left(\delta\beta\right)^2 \\ &\left(1\Big/\left|\frac{\partial \mathbf{X}}{\partial s}\right|\left|\frac{\partial \mathbf{X}}{\partial r}\right|\right)\left\{\frac{\partial \mathbf{X}}{\partial s} \circ \frac{\partial \mathbf{X}}{\partial r} - 2z\frac{\partial^2 \mathbf{X}}{\partial r \partial s} \circ \mathbf{e_3}\right\} 2\left(\delta\alpha\right)\left(\delta\beta\right) \end{aligned} \qquad \textbf{(3.3-19)}$$

Therefore one can respectively write the Lagrangian and Eulerian strains as

$$E_{11} = \frac{1}{2}\left(\frac{\partial \mathbf{X}}{\partial s} \circ \frac{\partial \mathbf{X}}{\partial s} - 1 \right) - z\kappa_s \left| \frac{\partial \mathbf{X}}{\partial s} \right|^2$$
$$E_{12} = \frac{1}{2}\left(\frac{\partial \mathbf{X}}{\partial s} \circ \frac{\partial \mathbf{X}}{\partial r} \right) - z\left(\frac{\partial^2 \mathbf{X}}{\partial r \partial s} \circ \mathbf{e_3} \right) \tag{3.3-20}$$
$$E_{22} = \frac{1}{2}\left(\frac{\partial \mathbf{X}}{\partial r} \circ \frac{\partial \mathbf{X}}{\partial r} - 1 \right) - z\kappa_r \left| \frac{\partial \mathbf{X}}{\partial r} \right|^2$$

and

$$e_{11} = \frac{1}{2}\left(1 - 1 \middle/ \left| \frac{\partial \mathbf{X}}{\partial s} \right|^2 \right) - z\kappa_s$$
$$e_{12} = \frac{1}{2}\left(\frac{\partial \mathbf{X}}{\partial s} \circ \frac{\partial \mathbf{X}}{\partial r} \right) \middle/ \left| \frac{\partial \mathbf{X}}{\partial s} \right| \left| \frac{\partial \mathbf{X}}{\partial r} \right| - z\left\{ \left(\frac{\partial^2 \mathbf{X}}{\partial r \partial s} \circ \mathbf{e_3} \right) \middle/ \left| \frac{\partial \mathbf{X}}{\partial s} \right| \left| \frac{\partial \mathbf{X}}{\partial r} \right| \right\} \tag{3.3-21}$$
$$e_{22} = \frac{1}{2}\left(1 - 1 \middle/ \left| \frac{\partial \mathbf{X}}{\partial r} \right|^2 \right) - z\kappa_r$$

We will assume that although displacements are large, the strains remain small, so the stresses and strains could be linearly related with Hooke's law. This will allow us to superpose the stresses due to in-plane and out-of-plane deformations after treating them separately. In particular, we choose to use a Lagrangian formulation for the in-plane deformations and an Eulerian description for the out-of-the plane deformations. Equivalent to Section 3.3.2's Eqn. (3.3-7), the in-plane components of the Lagrangian strains given in Eqn. (3.3-20) are

$$E_{11\_in\ plane} = \frac{1}{2}\left(\frac{\partial \mathbf{X}}{\partial s} \circ \frac{\partial \mathbf{X}}{\partial s} - 1 \right)$$
$$E_{12\_in\ plane} = \frac{1}{2}\left(\frac{\partial \mathbf{X}}{\partial s} \circ \frac{\partial \mathbf{X}}{\partial r} \right) \tag{3.3-22}$$
$$E_{22\_in\ plane} = \frac{1}{2}\left(\frac{\partial \mathbf{X}}{\partial r} \circ \frac{\partial \mathbf{X}}{\partial r} - 1 \right)$$

and the Eulerian strains due to the out-of-plane deformations (bending and torsion) are

$$\begin{aligned}
e_{11\_out\ of\ plane} &= -z\kappa_s \\
e_{12\_out\ of\ plane} &= -z\left\{\left(\frac{\partial^2\mathbf{X}}{\partial r\partial s}\circ\mathbf{e_3}\right)\Big/\left|\frac{\partial\mathbf{X}}{\partial s}\right|\left|\frac{\partial\mathbf{X}}{\partial r}\right|\right\} = -z\tau \\
e_{22\_out\ of\ plane} &= -z\kappa_r
\end{aligned} \tag{3.3-23}$$

The Kirchhoff or 2nd Piola stresses due to the in-plane deformations are calculated by the isotropic Hooke's law for plane stresses as

$$\begin{aligned}
S_{11\_in\ plane} &= \frac{\bar{E}}{\left(1-\nu^2\right)}\left(E_{11\_in\ plane}+\nu E_{22\_in\ plane}\right) \\
S_{12\_in\ plane} &= \frac{\bar{E}}{\left(1+\nu\right)}\left(E_{12\_in\ plane}\right) \\
S_{22\_in\ plane} &= \frac{\bar{E}}{\left(1-\nu^2\right)}\left(E_{22\_in\ plane}+\nu E_{11\_in\ plane}\right)
\end{aligned} \tag{3.3-24}$$

where $\bar{E}$ is the Young's modulus and ν is the Poisson's ratio of the solid. Similarly, the Cauchy stresses due to the out-of-plane deformations are calculated by the isotropic Hooke's law for plane stresses as

$$\begin{aligned}
\sigma_{11\_out\ of\ plane} &= -\frac{\bar{E}z}{\left(1-\nu^2\right)}\left(\kappa_s+\nu\kappa_r\right) \\
\sigma_{12\_out\ of\ plane} &= -\frac{\bar{E}z}{\left(1+\nu\right)}\left\{\left(\frac{\partial^2\mathbf{X}}{\partial r\partial s}\circ\mathbf{e_3}\right)\Big/\left|\frac{\partial\mathbf{X}}{\partial s}\right|\left|\frac{\partial\mathbf{X}}{\partial r}\right|\right\} \\
\sigma_{22\_out\ of\ plane} &= -\frac{\bar{E}z}{\left(1-\nu^2\right)}\left(\kappa_r+\nu\kappa_s\right)
\end{aligned} \tag{3.3-25}$$

As in Section 3.3-2, we define stress resultants as the integrals of the stresses over the solid thickness q. Eqn. (3.3-26) is the divergence of these stress resultants due to in-plane deformations, which can be used with the solid's linear momentum equation stated in Eqn. (3.3-5) or in Eqn. (3.2-12) with the IB method.

$$F_{i\_in\ \ plane}\left(\mathbf{x_o},t\right)=\frac{1}{K}\frac{\partial}{\partial x_{oj}}\left(qS_{jk\_in\ \ plane}\frac{\partial X_i}{\partial x_{ok}}\right) \tag{3.3-26}$$

Next, we define internal moments throughout the thickness of the deformed solid as

$$\begin{aligned}
\mathbf{M_{11}} &= \int_{-\frac{q}{2}}^{\frac{q}{2}} z\mathbf{e_3}\times\sigma_{11}\mathbf{e_1}dz\\
\mathbf{M}_{12} &= \int_{-\frac{q}{2}}^{\frac{q}{2}} z\mathbf{e_3}\times\sigma_{12}\mathbf{e}_2dz\\
\mathbf{M}_{21} &= \int_{-\frac{q}{2}}^{\frac{q}{2}} z\mathbf{e_3}\times\sigma_{21}\mathbf{e}_1dz\\
\mathbf{M}_{22} &= \int_{-\frac{q}{2}}^{\frac{q}{2}} z\mathbf{e_3}\times\sigma_{22}\mathbf{e}_2dz
\end{aligned} \tag{3.3-27}$$

Substituting Eqns. (3.3-25) into Eqns. (3.3-27), and noting that the stresses due to in-plane deformations are uniform throughout the thickness so they will not contribute to the internal moments, we find

$$\begin{aligned}
\mathbf{M_{11}} &= -\frac{\bar{E}q^3}{12\left(1-\nu^2\right)}\left(\kappa_s+\nu\ \kappa_r\right)\mathbf{e_2}\\
\mathbf{M_{12}} &= \frac{\bar{E}q^3}{12\left(1+\nu\right)}\left\{\left(\frac{\partial^2\mathbf{X}}{\partial r\partial s}\circ\mathbf{e_3}\right)\Big/\left|\frac{\partial\mathbf{X}}{\partial s}\right|\left|\frac{\partial\mathbf{X}}{\partial r}\right|\right\}\mathbf{e_1}\\
\mathbf{M}_{21} &= -\frac{\bar{E}q^3}{12\left(1+\nu\right)}\left\{\left(\frac{\partial^2\mathbf{X}}{\partial r\partial s}\circ\mathbf{e_3}\right)\Big/\left|\frac{\partial\mathbf{X}}{\partial s}\right|\left|\frac{\partial\mathbf{X}}{\partial r}\right|\right\}\mathbf{e_2}\\
\mathbf{M_{22}} &= \frac{\bar{E}q^3}{12\left(1-\nu^2\right)}\left(\kappa_r+\nu\ \kappa_s\right)\mathbf{e_1}
\end{aligned} \tag{3.3-28}$$

Additionally, we define $\mathbf{M}_1$ and $\mathbf{M}_2$ as the internal moments applied on the constant *r* and *s* lines respectively (via the definition given in Eqn. 3.3-27), so

$$\begin{aligned}\mathbf{M}_1 &= \mathbf{M}_{11} + \mathbf{M}_{12} \\ \mathbf{M}_2 &= \mathbf{M}_{21} + \mathbf{M}_{22}\end{aligned} \tag{3.3-29}$$

Figure 3.3-2 shows the forces acting on an infinitesimal surface patch, where **N** denotes internal forces per unit length that are exerted by the neighboring surface patches, **-I** is the fluid force per unit area, and $\mathbf{W_s}$ is the external body force per unit area. The balance of linear momentum on this deformed patch yields to

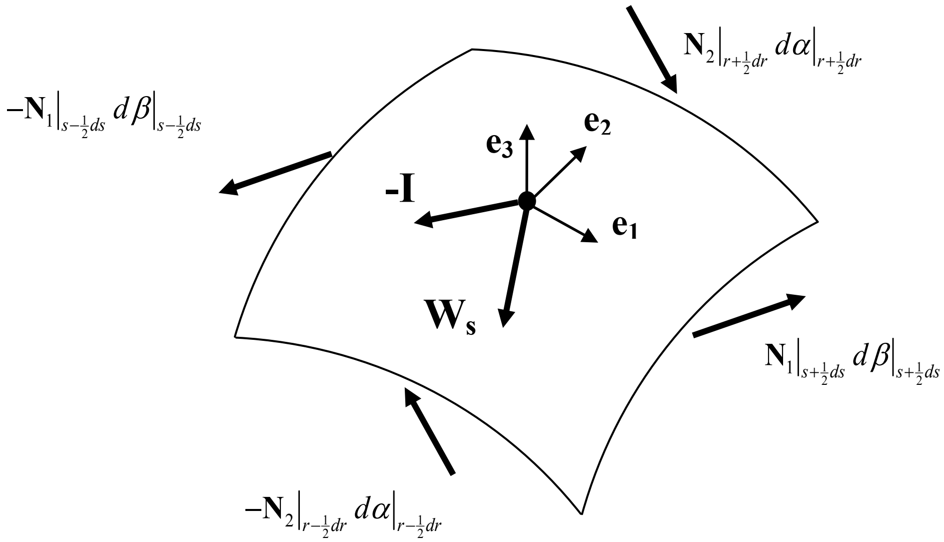

Figure 3.3-2: Forces acting on an infinitesimal surface patch

$$-\left(\mathbf{N}_1 d\beta\right)\big|_{s-\frac{1}{2}ds} + \left(\mathbf{N}_1 d\beta\right)\big|_{s+\frac{1}{2}ds} - \left(\mathbf{N}_2 d\alpha\right)\big|_{r-\frac{1}{2}dr} + \left(\mathbf{N}_2 d\alpha\right)\big|_{r+\frac{1}{2}dr} - \mathbf{I}\, dA + \mathbf{W_s}\, dA = \rho_{sc}\, dA \frac{\partial^2 \mathbf{X}}{\partial t^2}$$

or

$$\frac{1}{K}\frac{\partial}{\partial s}\left(\mathbf{N}_1 \left|\frac{\partial \mathbf{X}}{\partial r}\right|\right) + \frac{1}{K}\frac{\partial}{\partial r}\left(\mathbf{N}_2 \left|\frac{\partial \mathbf{X}}{\partial s}\right|\right) - \mathbf{I} + \mathbf{W_s} = \frac{1}{K}\rho_s \frac{\partial^2 \mathbf{X}}{\partial t^2} \tag{3.3-30}$$

Here ρ_s and ρ_{sc} are respectively the solid surface's mass density per unit undeformed and deformed area, which are related as $\rho_s = \rho_{sc} K$. Note that, the form of Eqn. (3.3-30) is used only for the out-of-plane elastic effects, whereas Eqns. (3.3-26) and (3.3-5) are used for the in-plane effects. Comparing Eqn. (3.3-30) with Eqn. (3.2-3) we find

$$\mathbf{F}_{out\ of\ plane} = \frac{1}{K}\frac{\partial}{\partial s}\left(\mathbf{N}_1\left|\frac{\partial \mathbf{X}}{\partial r}\right|\right) + \frac{1}{K}\frac{\partial}{\partial r}\left(\mathbf{N}_2\left|\frac{\partial \mathbf{X}}{\partial s}\right|\right) \tag{3.3-31}$$

Figure 3.3-3 shows the moments acting on the same infinitesimal surface patch, where **M** denotes internal moments per unit length and **M_s** is the external applied moment per unit area. Denoting the angular momentum per unit area by **H**, the balance of angular momentum on this patch yields to

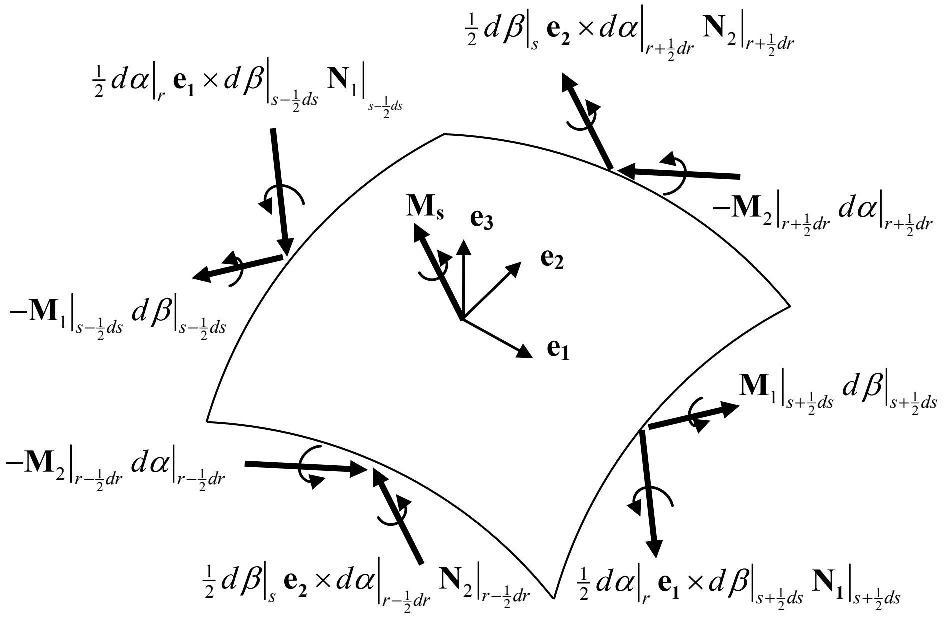

Figure 3.3-3: Moments acting on an infinitesimal surface patch

$$-(\mathbf{M}_1 d\beta)\big|_{s-\frac{ds}{2}} + (\mathbf{M}_1 d\beta)\big|_{s+\frac{ds}{2}} - (\mathbf{M}_2 d\alpha)\big|_{r-\frac{dr}{2}} + (\mathbf{M}_2 d\alpha)\big|_{r+\frac{dr}{2}} +$$

$$+ d\alpha\big|_r \, \mathbf{e}_1 \times \left(\frac{(d\beta \mathbf{N}_1)_{s+\frac{ds}{2}} + (d\beta \mathbf{N}_1)_{s-\frac{ds}{2}}}{2} \right) + d\beta\big|_s \, \mathbf{e}_2 \times \left(\frac{(d\alpha \mathbf{N}_2)_{r+\frac{dr}{2}} + (d\alpha \mathbf{N}_2)_{r-\frac{dr}{2}}}{2} \right)$$

$$+\mathbf{M}_\mathbf{s} dA = dA \frac{\partial \mathbf{H}}{\partial t}$$

which could be reduced to

$$\frac{1}{K}\frac{\partial}{\partial s}\left(\mathbf{M}_1 \left|\frac{\partial \mathbf{X}}{\partial r}\right|\right) + \frac{1}{K}\frac{\partial}{\partial r}\left(\mathbf{M}_2 \left|\frac{\partial \mathbf{X}}{\partial s}\right|\right) + \frac{1}{K}\left|\frac{\partial \mathbf{X}}{\partial s}\right|\left|\frac{\partial \mathbf{X}}{\partial r}\right|\left(\mathbf{e}_1 \times \mathbf{N}_1 + \mathbf{e}_2 \times \mathbf{N}_2\right) + \mathbf{M}_\mathbf{s} = \frac{\partial \mathbf{H}}{\partial t}$$

(3.3-32)

For very thin solid surfaces, such as a cloth, the contribution of the change of angular momentum is neglected from Eqn. (3.3-32). To assess the validity of this assumption we nondimensionalize Eqn. (3.3-32) with a characteristic length scale L, velocity scale U_o, and mass scale $\rho_s L^2$ where ρ_s is the solid surface's mass per unit area as before. We scale the internal moments by $\bar{E}q^3/L$ (due to the form of Eqn. (3.3-28)) and drop the external applied moment ($\mathbf{M}_\mathbf{s}$) for simplicity. Doing so, the nondimensional form of Eqn. (3.3-32) can be found as

$$\frac{\bar{E}q}{\rho_s {U_o}^2}\left(\frac{q^2}{L^2}\right)\frac{1}{\bar{K}}\frac{\partial}{\partial \bar{s}}\left(\overline{\mathbf{M}}_1 \left|\frac{\partial \overline{\mathbf{X}}}{\partial \bar{r}}\right|\right) + \frac{\bar{E}q}{\rho_s {U_o}^2}\left(\frac{q^2}{L^2}\right)\frac{1}{\bar{K}}\frac{\partial}{\partial \bar{r}}\left(\overline{\mathbf{M}}_2 \left|\frac{\partial \overline{\mathbf{X}}}{\partial \bar{s}}\right|\right)$$

$$+\frac{1}{\bar{K}}\left|\frac{\partial \overline{\mathbf{X}}}{\partial \bar{s}}\right|\left|\frac{\partial \overline{\mathbf{X}}}{\partial \bar{r}}\right|\left(\mathbf{e}_1 \times \overline{\mathbf{N}}_1 + \mathbf{e}_2 \times \overline{\mathbf{N}}_2\right) = \left(\frac{q^2}{L^2}\right)\frac{\partial \overline{\boldsymbol{\omega}}}{\partial \bar{t}}$$

where the symbols with bars denote dimensionless quantities, and $\boldsymbol{\omega}$ is the angular velocity of the plate. This form shows that if $\left(\bar{E}q/\rho_s\right) >> {U_o}^2$ the effect of the change in angular momentum will be small in Eqn. (3.3-32).

Dropping the effect of change of angular momentum, Eqn. (3.3-32) reduces to

$$\frac{\partial}{\partial s}\left(\mathbf{M}_1\left|\frac{\partial \mathbf{X}}{\partial r}\right|\right)+\frac{\partial}{\partial r}\left(\mathbf{M}_2\left|\frac{\partial \mathbf{X}}{\partial s}\right|\right)+\left|\frac{\partial \mathbf{X}}{\partial s}\right|\left|\frac{\partial \mathbf{X}}{\partial r}\right|\left(\mathbf{e}_1\times\mathbf{N}_1+\mathbf{e}_2\times\mathbf{N}_2\right)+K\mathbf{M}_s=\mathbf{0} \qquad \textbf{(3.3-33)}$$

Moreover, it can be shown that

$$\left[\frac{\partial}{\partial s}\left(\mathbf{M}_1\left|\frac{\partial \mathbf{X}}{\partial r}\right|\right)+\frac{\partial}{\partial r}\left(\mathbf{M}_2\left|\frac{\partial \mathbf{X}}{\partial s}\right|\right)\right]\circ\mathbf{e}_3=0$$

so if the externally applied moment, $\mathbf{M}_s$, is zero then

$$\begin{aligned}\mathbf{N}_1&=N_1\mathbf{e}_3\\ \mathbf{N}_2&=N_2\mathbf{e}_3\end{aligned} \qquad \textbf{(3.3-34)}$$

This result helps us to rewrite the balance of angular momentum as,

$$\frac{\partial}{\partial s}\left(\mathbf{M}_1\left|\frac{\partial \mathbf{X}}{\partial r}\right|\right)+\frac{\partial}{\partial r}\left(\mathbf{M}_2\left|\frac{\partial \mathbf{X}}{\partial s}\right|\right)+\left|\frac{\partial \mathbf{X}}{\partial s}\right|\left|\frac{\partial \mathbf{X}}{\partial r}\right|\left(-N_1\mathbf{e}_2+N_2\mathbf{e}_1\right)=\mathbf{0} \qquad \textbf{(3.3-35)}$$

Summary

As a summary, the sequence of Eqns. (3.3-14), (3.3-15), (3.3-9), (3.3-16), (3.3-28), (3.3-29), (3.3-35), (3.3-34) and (3.3-31) models the solid internal forces due to out-of-plane deformations, whereas the sequence of Eqns. (3.3-22), (3.3-24) and (3.3-26) models the internal forces due to in-plane deformations, which are both in turn used with Eqn. (3.2-12) in the context of the simulation's fluid/structure interaction model.

3.3.4 One-dimensional elastic fibers

One-dimensional elastic fibers can be modeled as lines and we use the results of Section 3.3.3 to quickly derive the equations of motion. We parameterize a line in $\mathbf{R}^2$ as

$$\mathbf{X} = \mathbf{X}(s)$$

and we define the tangent vector to this line as

$$\mathbf{e}_1 = \frac{\partial \mathbf{X}}{\partial s} \Big/ \left| \frac{\partial \mathbf{X}}{\partial s} \right| \qquad \textbf{(3.3-36)}$$

We choose

$$\mathbf{e}_2 = (0,0,1) \qquad \textbf{(3.3-37)}$$

so we restrict the fiber normal vector to construct a right-handed coordinate system $\mathbf{e}_1$, $\mathbf{e}_2$, and $\mathbf{e}_3$ as

$$\mathbf{e}_3 = \mathbf{e}_1 \times \mathbf{e}_2 \qquad \textbf{(3.3-38)}$$

Following Section 3.3.3, but taking the derivatives and variations with respect to r as zero, from Eqn. (3.3-22) we find the in-plane Lagrangian strain of the fiber as

$$E_{in\ plane} = \frac{1}{2}\left(\frac{\partial \mathbf{X}}{\partial s} \circ \frac{\partial \mathbf{X}}{\partial s} - 1 \right) \qquad \textbf{(3.3-39)}$$

and we use the one-dimensional Hooke's law to find the 2nd Piola stress of the fiber as

$$S_{in\ plane} = \bar{E}\, E_{in\ plane} \qquad \textbf{(3.3-40)}$$

where $\bar{E}$ is the fiber Young's modulus. Next we find the in-plane internal forces as

$$F_{i\_in\ plane}(\mathbf{x_0},t)=\frac{1}{K}\frac{\partial}{\partial s}\left(q\,S_{in\ plane}\frac{\partial X_i}{\partial s}\right) \tag{3.3-41}$$

where q is the solid thickness and K is

$$K=\left|\frac{\partial \mathbf{X}}{\partial s}\right|$$

Again from Section 3.3.3, we find the internal moment on the fiber as

$$\mathbf{M_{11}}=-\frac{\bar{E}q^3}{12}\kappa_s\mathbf{e_2} \tag{3.3-42}$$

where κ_s is the curvature of the fiber that is given as

$$\kappa_s=\left(\frac{\partial \mathbf{e_1}}{\partial s}\circ\mathbf{e_3}\right)\Big/\left|\frac{\partial \mathbf{X}}{\partial s}\right|$$

which is equal to

$$\kappa_s=\frac{\left(\frac{\partial Y}{\partial s}\frac{\partial^2 X}{\partial s^2}-\frac{\partial X}{\partial s}\frac{\partial^2 Y}{\partial s^2}\right)}{\left(\left(\frac{\partial X}{\partial s}\right)^2+\left(\frac{\partial Y}{\partial s}\right)^2\right)^{3/2}} \tag{3.3-43}$$

Next, the balance of angular and linear momentum equations yield into

$$\frac{\partial}{\partial s}(\mathbf{M_{11}})+\left|\frac{\partial \mathbf{X}}{\partial s}\right|(-N_1\mathbf{e_2})=\mathbf{0} \tag{3.3-44}$$

and

$$\mathbf{F}_{out\ of\ plane} = \frac{1}{K}\frac{\partial}{\partial s}\left(N_1\mathbf{e}_3\right) \qquad \textbf{(3.3-45)}$$

3.3.5 Real cloth

In the previous sections the solid membranes, plates, and fibers are idealized as isotropic materials and assumed to obey the Hooke's law, which linearly relates their strains and stresses. However, real cloth is anisotropic and the material laws relating strains to stresses are nonlinear. Cloth consists of wefts and warps. Warps are strong lengthwise yarns through which less strong weft yarns are woven[1]. The individual properties of wefts and warps and their interwoven structure set the anisotropy of cloth mechanical properties. Moreover, the interwoven structure of the cloth causes frictional forces as the warps and wefts slide against each other as the cloth deforms. As a simplified but yet more advanced assumption than the previous isotropic one, one might apply the orthotropic material model to describe the clothes, which is summarized below.

Assume the warp and weft directions to be orthogonal to each other (at least at the undeformed, reference state) and denote those directions with unit vectors $\mathbf{t}_\mathbf{x}$ and $\mathbf{t}_\mathbf{y}$ respectively. If we choose to align $\mathbf{t}_\mathbf{x}$ and $\mathbf{t}_\mathbf{y}$ with the previously defined $\mathbf{e}_1$ and $\mathbf{e}_2$ directions respectively (see Section 3.3.3 for their description) the stresses and strains could be linearly related as

$$\begin{pmatrix} S_{11} \\ S_{22} \\ S_{12} \end{pmatrix} = \begin{pmatrix} Q_{11} & Q_{12} & 0 \\ Q_{12} & Q_{22} & 0 \\ 0 & 0 & Q_{33} \end{pmatrix} \begin{pmatrix} E_{11} \\ E_{22} \\ 2E_{12} \end{pmatrix} \qquad \textbf{(3.3-46)}$$

with

---

[1] As defined in www.wikipedia.org as of 9/2007

$$Q_{11} = \frac{\bar{E}_{xx}}{1-\nu_{xy}\nu_{yx}}$$
$$Q_{22} = \frac{\bar{E}_{yy}}{1-\nu_{xy}\nu_{yx}}$$
$$Q_{12} = \frac{\nu_{xy}\bar{E}_{yy}}{1-\nu_{xy}\nu_{yx}} = \frac{\nu_{yx}\bar{E}_{xx}}{1-\nu_{xy}\nu_{yx}}$$
$$Q_{33} = \bar{G}_{xy} = \bar{G}_{yx}$$
$$\nu_{yx} = \frac{\bar{E}_{yy}}{\bar{E}_{xx}}\nu_{xy}$$

where $\bar{E}_{xx}$, $\bar{E}_{yy}$ are respectively the Young's modulus in the warp and weft directions, $\bar{G}_{xy}$ is the in-plane shear modulus between the warp and weft directions, ν_{xy} is the ratio between the shrinkage in the weft direction to the unit extension in the warp direction, while ν_{yx} is vice versa. Moreover, if $\mathbf{t_x}$ makes an angle θ with $\mathbf{e_1}$ as $\mathbf{t_x}$ is rotated along the positive $\mathbf{e_3}$ direction then the equations are

$$\begin{pmatrix} S_{11} \\ S_{22} \\ S_{12} \end{pmatrix} = \begin{pmatrix} \bar{Q}_{11} & \bar{Q}_{12} & \bar{Q}_{13} \\ \bar{Q}_{12} & \bar{Q}_{22} & \bar{Q}_{23} \\ \bar{Q}_{13} & \bar{Q}_{23} & \bar{Q}_{33} \end{pmatrix} \begin{pmatrix} E_{11} \\ E_{22} \\ 2E_{12} \end{pmatrix} \tag{3.3-47}$$

where

$$\bar{Q}_{11} = Q_{11}\cos^4\theta + 2(Q_{12}+2Q_{33})\sin^2\theta\cos^2\theta + Q_{22}\sin^4\theta$$
$$\bar{Q}_{12} = Q_{12}\left(\sin^4\theta+\cos^4\theta\right) + (Q_{11}+Q_{22}-4Q_{33})\sin^2\theta\cos^2\theta$$
$$\bar{Q}_{22} = Q_{11}\sin^4\theta + 2(Q_{12}+2Q_{33})\sin^2\theta\cos^2\theta + Q_{22}\cos^4\theta$$
$$\bar{Q}_{13} = (Q_{11}-Q_{12}-2Q_{33})\sin\theta\cos^3\theta + (Q_{12}-Q_{22}+2Q_{33})\sin^3\theta\cos\theta$$
$$\bar{Q}_{23} = (Q_{11}-Q_{12}-2Q_{33})\sin^3\theta\cos\theta + (Q_{12}-Q_{22}+2Q_{33})\sin\theta\cos^3\theta$$
$$\bar{Q}_{33} = (Q_{11}+Q_{22}-2Q_{12}-2Q_{33})\sin^2\theta\cos^2\theta + Q_{33}\left(\sin^4\theta+\cos^4\theta\right)$$

Note that, as the cloth deforms the weft and the warp directions would not necessarily stay orthogonal to each other, so one needs to update the above stress-strain model to accommodate the non-orthogonality between the warp and weft lines if formulating the problem on the deformed cloth shape. In Section 3.3.3 the in-plane membrane effects were modeled at the undeformed cloth state and the out-of-plane effects such as bending and torsion stiffness were modeled at the deformed cloth state.

There are several ways to measure cloth mechanical properties, but to our knowledge the most traditional and applied techniques are: "Kawabata Evaluation System for Fabrics" (KES-F) developed by Kawabata (1980) for measuring cloth axial and bending stiffness, Hu et al. (1997)'s "Kawabata Shear Test" (KES-Shear) for measuring cloth in-plane shear rigidity, and "Fabric Assurance by Simple Testing" (FAST) by Ly et al. (1991). Bassett et al. (1999) gives a review of the experimental techniques. Lo et al (2002) offers a way of estimating in-plane shear modulus values at directions different than waft and weft. There are also micromechanical models on the cloth's interwoven structure to predict its macro behavior and recent works include Boisse et al. (2006, 2005, 2001), Zhang et al. (2003), King et al. (2005), Lu et al. (2005), and Xue et al. (2003) as well as the empirical model of Taibi (2001). Interested readers can refer to these works for a survey of the older micromechanical and empirical models.

3.3.6 Boundary Conditions for Cloth in Fluid

Unless stated otherwise, the cloth free-ends are modeled to be traction and moment free. If the clothes are modeled as membranes without any bending or torsion stiffness, only zero tension and in-plane shear boundary conditions are required at the free-edges. See Section 3.4.1 for the numerical implementation of these boundary conditions. One might question these choices by noting that these clothes are inserted into fluids and they are no longer 'free in space'. But note that, as explained in Section 3.2 the reaction forces between the fluid and solid are separately modeled, so these free-edge boundary conditions still hold true.

3.4 Numerical discretization

3.4.1 Discretization of the equations describing the cloth mechanics

This present study uses second-order accurate finite-difference approximations to compute the various spatial derivatives in the equations presented in Section 3.3. Doing so, to imply the correct boundary conditions various quantities are being computed at different locations.

For the case of a one-dimensional cloth, the Lagrangian markers that are used to track the cloth pieces are interpreted to form the cloth pieces as shown in Fig. 3.4-1(a) below. The first Lagrangian marker is assumed to be half a uniform grid-spacing inside from the edge of the cloth. The rest of the markers inside the cloth are regularly spaced. Note that this is only true for an unstreched cloth and various correction terms are already included in the physical formulations to compensate the stretching of the cloth pieces. Next, cloth's tension and internal moment are calculated on the staggered positions shown in Fig. 3.4-1(b). To do so, deformation gradients and curvatures are also being computed at these same staggered points. Then, the zero tension and zero internal moment boundary conditions are implied at the cloth's free-ends as shown in Fig. 3.4-1(c). Using the computed tension and internal moment with their boundary values, their derivatives are calculated at the Lagrangian markers as sketched in Fig. 3.4-1(d). Note that the derivative of the tension is the in-plane elastic force via Eqn. (3.3-41), whereas the derivative of the internal moment is the internal shear force via Eqn. (3.3-44). Before computing the out-of-plane elastic force through Eqn. (3.3-45), to ease implying the zero internal shear force boundary condition at the cloth's free-ends, internal shear forces are interpolated to the staggered locations as shown in Fig. 3.4-1(e). Using the internal shear forces on the staggered locations as well as their boundary values at the edges, the out-of-plane cloth elastic forces are computed on the Lagrangian markers as shown in Fig. 3.4-1(g).

This methodology is similar for a two-dimensional cloth in a three-dimensional space. However, some differences are needed to calculate cloth's in-plane shear stress and strain components through Eqns. (3.3-22b) and (3.3-24b) and the internal moments through Eqn. (3.3-23), and (3.3-28). To understand the reasons for these modifications, first view the positions of the Lagrangian markers and the staggered locations on a two-dimensional unstreched and flat cloth, which is parameterized with constant *r* and *s* lines as plotted in Fig. 3.4-2 below. As noted in Section 3.3, these constant *r* and *s* lines are unstreched and orthogonal to each other in the cloth piece's hypothetical unstressed, undeformed, flat hypothetical reference position. Note from Fig. 3.4-2 that the staggered locations on the constant *r* and *s* lines do not coincide. This obviously creates inconveniences while calculating the cloth's in-plane shear deformation (through Eqn. (3.3-22b)), curvature (through Eqns. (3.3-14), (3.3-15), (3.3-9), and (3.3-16)), and twist (through Eqn. (3.3-28b and c)) at these staggered locations.

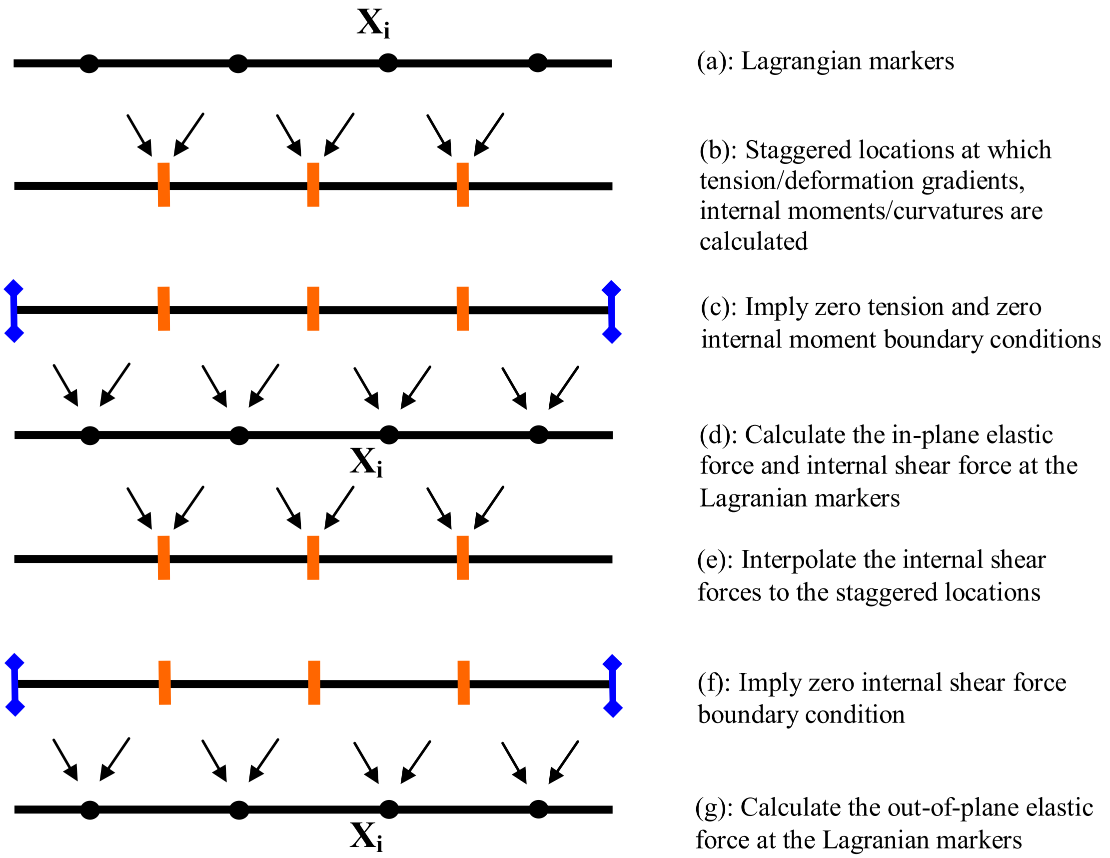

Figure 3.4-1: An illustrative procedure for computing the elastic forces on a one-dimensional cloth piece

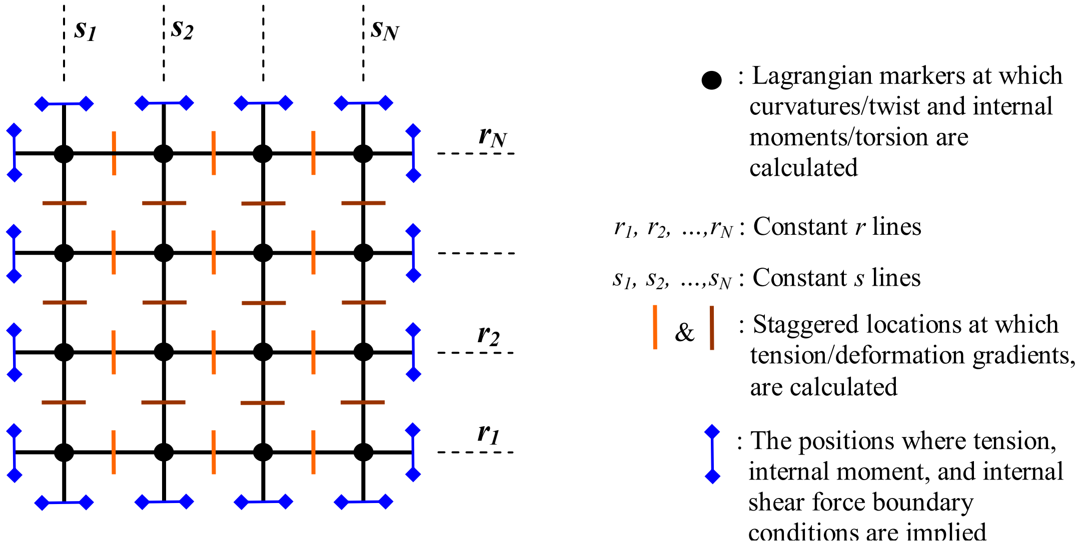

Figure 3.4-2: The locations of the Lagrangian markers, constant r and s lines, and the staggered locations on a two-dimensional cloth piece

To avoid these difficulties the cloth's in-plane shear deformations are computed at the so called 'centroid points' as shown in Fig. 3.4-3 below. Then, the in-plane shear stresses computed through Eqn. (3.3-24b) at these 'centroid points' are interpolated onto the original staggered points by implying the zero in-plane shear stress boundary condition at the free edges as shown in Fig. 3.4-3.

On the other hand, curvature/ twist and the internal moment/torsion are computed at the positions of the Lagrangian markers, which are then interpolated onto the staggered points (only near the free-edges) to conveniently apply the zero moment boundary conditions and to proceed computing the internal shear forces on the Lagrangian markers via Eqn. (3.3-35).

The rest of the procedure follows the one-dimensional case discussed before.

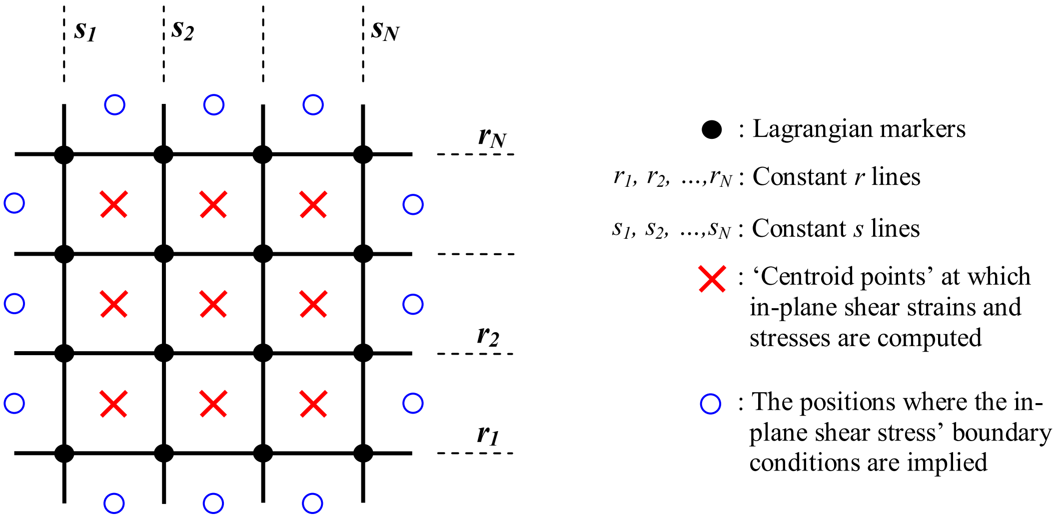

Figure 3.4-3: The locations of the 'centroid points'

As for implementing Eqn. (3.2-14), we use the forward Euler method in the three-dimensional simulations, whereas we use the implicit Broyden's method (iterative) for the two-dimensional computations as suggested in Leveque et al. (1997), Lee (2002) and Lee et al. (2003).

3.4.2 Numerical approximation of the Dirac-delta functions

The Immersed Boundary method presented in Section 3.2 desingularizes a lower dimensional solid on to a higher dimensional Eulerian grid by approximate Dirac-delta functions. This section describes the approximate Dirac-delta function that this present study uses with some further considerations.

For $a \in (-\infty, +\infty)$, $0 < \varepsilon \ll 1$, a one-dimensional Dirac-delta function δ is defined as

$$\int_{a-\varepsilon}^{a+\varepsilon} \delta(x-a)\,dx = 1 \qquad \textbf{(3.4-1)}$$

$$\int_{-\infty}^{a-\varepsilon} \delta(x-a)\,dx = \int_{a+\varepsilon}^{+\infty} \delta(x-a)\,dx = 0 \qquad \textbf{(3.4-2)}$$

Higher-dimensional Dirac-delta functions could be defined by repeatedly multiplying one-dimensional forms. For instance, a three-dimensional Dirac-delta function is

$$\delta(\mathbf{x}-\mathbf{X})=\delta(x-X)\,\delta(y-Y)\,\delta(z-Z) \quad \text{where } \mathbf{x}=(x,y,z) \quad \text{and} \quad \mathbf{X}=(X,Y,Z)$$

(3.4-3)

It is not possible to use this form of the Dirac-delta function in the numerical computations because of the following reasons: (i) one cannot infinitely discretize the discrete computational domain to capture an infinitesimal ε , and (ii) it is not possible to work with singular functions on digital computers. As an approximation to the Dirac-delta function, Peskin (2002) uses the following form for the three-dimensional Dirac-delta functions

$$\delta(\mathbf{x})=\phi(x)\phi(y)\phi(z) \quad \text{where } \mathbf{x}=(x,y,z) \tag{3.4-4}$$

where ϕ is a one-dimensional Dirac-delta function approximation. As for ϕ this present study uses

$$\phi(r)=\begin{cases}\dfrac{1}{2\varepsilon_{\delta}}\left(1+cos\left(\dfrac{\pi\, r}{\varepsilon_{\delta}}\right)\right), & |r|\le\varepsilon_{\delta}\\ 0, & \text{otherwise}\end{cases} \tag{3.4-5}$$

with $\varepsilon_{\delta} = 2h$ as was mentioned by Peskin (2002), where h is the uniform Eulerian grid size. Other than this form, there are some other forms of ϕ that have been used as mentioned by Peskin (2002). Note that, the current approximate Dirac-delta function has a compact support of four grid spacings. Such a compact support can make closely located solid pieces artificially stick to each other. On the other hand, in this research it was observed that a narrower compact support has adverse effects on the computational stability.

3.5 Verification

3.5.1 Matching the natural frequencies of a vibrating plate

In this verification study the simulation's solid model is tested using the reported free vibration frequencies of a free edged and thin vibrating plate. Doing so, the results given in Leissa (1969) and Clark (1972) are used as the true natural frequencies and modes. However, some of these reported results are not exact, but are obtained by the approximate Ritz method. It is also important to mention that those natural frequencies and modes were derived assuming the vibrations are small in amplitude, or in other words, the solids are given a very small initial perturbation from their flat and unstressed equilibrium states to initiate vibrations. For this reason, the results of this study cannot serve to verify our solid formulation with large deformations.

As described in Section 3.2, in the simulation the linear momentum equations of the solid are solved together with the linear momentum equations of the fluid in which they are immersed in. To reduce the effect of the surrounding fluid on the results, very small but non-zero values are set to the fluid density and viscosity. The reason for not using zero fluid density is because the simulation contains terms proportional to the reciprocal of fluid density. Also, using very small fluid viscosity values adversely affected the long-term robustness of the computations, since truncation errors in the finite difference approximations might include small anti-viscosity terms accidentally increasing the total energy and amplifying the imperfections.

Unless stated otherwise, the results presented below for the bending or torsional modes are obtained for a square plate with

$$\frac{1}{L^2}\sqrt{\frac{K_b}{\rho_s}} = \frac{1}{10}\left(\frac{N_p\text{-}1}{N_p}\right)^2 \quad \text{rad/s, or}$$

$$\frac{1}{L^2}\sqrt{\frac{K_t}{\rho_s}} = \frac{1}{10}\left(\frac{N_p\text{-}1}{N_p}\right)^2 \quad \text{rad/s}$$

where N_p x N_p is the number of the Lagrangian points on the plate, and K_b and K_t is the bending and torsional stiffness defined as

$$K_b = \frac{\bar{E}q^3}{12\left(1-\nu^2\right)}, \quad K_t = \frac{\bar{E}q^3}{12\left(1+\nu\right)}$$

where $\bar{E}$ and ν are respectively the isotropic Young's modulus and Poisson's ratio, q is the uniform plate thickness and, ρ_s is the plate's mass density over its surface area. The size of the square plate we use in our tests is L x L.

On the other hand, the results presented below for the longitudinal vibration mode is obtained for a square plate with

$$\frac{1}{L}\sqrt{\frac{\bar{E}q}{\rho_s}} = \frac{1}{2}\left(\frac{N_p\text{-}1}{N_p}\right)^2 \quad \text{rad/s}$$

Also, unless stated otherwise, the maximum amplitude Δ of the initial perturbations are set to satisfy

$$\frac{\Delta}{L} \leq O(\ 10^{-4})$$

The two different bending modes used in this study are plotted in Fig. 3.5-1(a) and (b) below, whereas Fig. 3.5-1(c) shows the tested torsional mode.

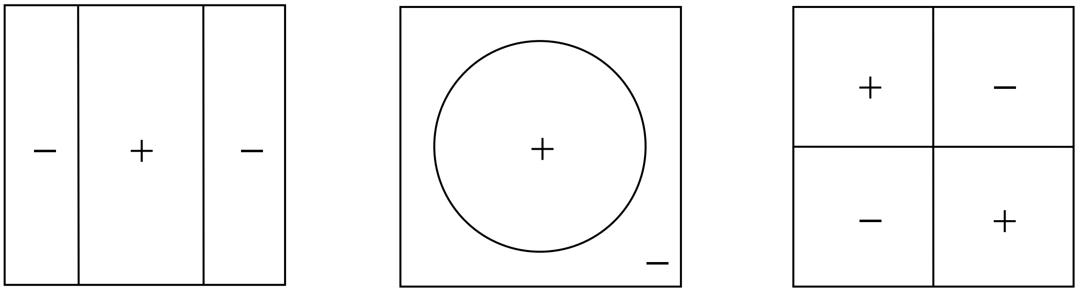

Case (a) Case (b) Case (c)

Figure 3.5-1: The bending and torsional mode shapes of the vibrating plate used in this study

The distinct regions in each of the mode shapes shown in Fig. 3.5-1 move in opposite directions as the plate oscillate. The natural frequencies corresponding to these mode shapes are given in Leissa (1969) as,

$$\omega = 22.373\left(\frac{1}{L}\right)^2\sqrt{\frac{K_b}{\rho_s}} \quad (\text{for } \upsilon = 0, \text{Case (a)}) \tag{3.5-1}$$

$$\omega = 23.97\left(\frac{1}{L}\right)^2\sqrt{\frac{K_b}{\rho_s}} \quad (\text{for } \upsilon = 0.225, \text{Case (b)}) \tag{3.5-2}$$

$$\omega = 13.086\left(\frac{1}{L}\right)^2\sqrt{\frac{K_t}{\rho_s}} \quad (\text{for } \upsilon = 0.343,\ \text{Case (c)}) \tag{3.5-3}$$

Moreover, the simulation is tested against the lowest natural frequency of a plate due to longitudinal/axial vibrations, which is given by Clark (1972) as,

$$\omega = \frac{\pi}{L}\sqrt{\frac{\bar{E}q}{\rho_s}} \quad (\text{for } \upsilon = 0) \tag{3.5-4}$$

which will be referred as ‘Case (d)’. For this case, it’s the plate’s extensional stiffness together with the plate’s inertia causing the mechanical vibrations. The mode shape of this motion is given in Clark (1972).

To save computational time, the pressure-correction step of the fractional step Navier-Stokes solver (presented in Chapter 2) – the bottleneck part of the whole computer program, was ‘switched-off’. As a result, the computed velocity field is no longer being enforced to be divergence-free anymore. This action is reasonable because in this verification study the solid elastic response is tested against the reported results which don’t consider the surrounding fluid. As long as very small but non-zero values are set for the fluid density and viscosity, the effect of the surrounding fluid will vanish from the results as will be verified below.

In the simulation results, the period of the first vibration cycle in time histories of the plate’s elastic bending or extensional energy was used to report natural frequencies. The reason for this is the simulations are run with very small physical damping and the numerical anti-damping in truncation errors amplifies the noise in the results as the time elapses.

In all the simulations, for every L x L cloth a $2L$ x $2L$ x $2L$ Eulerian domain was used. The convergence rate is defined as the slope of the line joining two points with coordinates $\left(\ln(h),\ \ln(\text{Error})\right)$, where h is the uniform Eulerian mesh width.

3.5.1.1 Effect of the Eulerian grid size

The effect of the Eulerian grid size was studied using an approximate 1:1 Lagrangian to Eularian mesh width ratio. The results obtained for the mode shapes (a), (b), (c), and (d) are tabulated in Tables 3.5-1, 3.5-2, 3.5-3, and 3.5-4, respectively. The time step values used in the simulations are given in the captions of the tables.

Table 3.5-1: Effect of the Eulerian grid size on the computed natural frequency for the mode shape of case (a), $\Delta t \approx 1.3\text{x}10^{-4}$ (1/ω)

Eulerian grid size	Lagrangian grid size	ω_{exact} [rad/s]	Relative error	Convergence rate
33^3	15^2	1.95	8.69 ±0.15 % slower	—
65^3	30^2	2.09	3.17 ±0.16 % slower	1.49
129^3	60^2	2.16	1.31 ±0.17 % slower	1.29

Table 3.5-2: Effect of the Eulerian grid size on the computed natural frequency for the mode shape of case (b), $\Delta t \approx 1.4\text{x}10^{-4}$ (1/ω)

Eulerian grid size	Lagrangian grid size	ω_{exact} [rad/s]	Relative error	Convergence rate
33^3	15^2	2.09	8.79 ±0.16 % slower	—
65^3	30^2	2.24	3.38 ±0.36 % slower	1.41
129^3	60^2	2.32	0.93 ±0.18 % slower	1.88

Table 3.5-3: Effect of the Eulerian grid size on the computed natural frequency for the mode shape of case (c), $\Delta t \approx 1.5\text{x}10^{-4}$ (1/ω)

Eulerian grid size	Lagrangian grid size	ω_{exact} [rad/s]	Relative error	Convergence rate
33^3	15^2	1.14	5.59 ±0.36 % slower	—
65^3	30^2	1.22	2.36 ±0.39 % slower	1.27
129^3	60^2	1.27	0.24 ±0.10 % slower	3.33

Table 3.5-4: Effect of the Eulerian grid size on the computed natural frequency for the mode shape of case (d), $\Delta t \approx 9.3\text{x}10^{-5}$ (1/ω)

Eulerian grid size	Lagrangian grid size	ω_{exact} [rad/s]	Relative error	Convergence rate
17^3	7^2	1.15	7.59 ±0.10 % slower	—
33^3	15^2	1.37	2.37 ±0.11 % slower	1.75
65^3	30^2	1.47	0.92 ±0.11 % slower	1.40

The results were very noisy when using the mode shape given in Leissa (1969) for Case (c). To overcome this issue the ‘noisy’ plate was let to vibrate in a very viscous fluid until the high frequency noise in its mode shape died-out, and then this ‘corrected’ mode shape at a predetermined bending energy value was released in a negligibly viscous fluid to measure its natural frequency. However, at this predetermined bending energy value the mode shape was still noisy for the case with 129^3 Eulerian and 60^2 Lagrangian points, so for that particular case the ‘noisy’ plate was left in the viscous fluid getting damped for a longer duration than the other cases. This might be part of the reason for why the result of this case had a very high convergence rate compared to the other cases.

As could be seen in the tabulated results above, the simulation's solid model can capture the dynamics of a vibrating plate at the small deformation regime.

3.5.1.2 Effect of the ratio between Lagrangian and Eulerian mesh width

The effect of the ratio between Lagrangian to Eularian mesh width was studied for cases (b) and (d). These cases were selected because Case (b) captures the out-of-plane bending mode, whereas Case (d) captures the in-plane extension mode. The results are summarized in Tables 3.5-5 and 3.5-6.

Table 3.5-5: Effect of the ratio between Lagrangian and Eulerian mesh width on the computed natural frequency for the mode shape of case (b) with $\Delta t \approx 1.4\text{x}10^{-4}$ (1/ω) and using 33^3 Eulerian points

Lagrangian to Eulerian mesh width ratio	Relative error
1.18	8.79 ±0.16 % slower
0.57	results diverged
0.28	results diverged

Table 3.5-6: Effect of the ratio between Lagrangian and Eulerian mesh width on the computed natural frequency for the mode shape of case (d) with $\Delta t \approx 9.3\text{x}10^{-5}$ (1/ω) and using 17^3 Eulerian points

Lagrangian to Eulerian mesh width ratio	Relative error
1.42	7.59 ±0.10 % slower
0.61	6.74 ±0.11 % slower
0.29	6.60 ±0.12 % slower

For Case (b), using a 0.57 Lagrangian to Eulerian mesh width ratio, in its first quarter of vibration cycle the plate flattened itself under the effect of its bending stiffness, but then failed to complete its oscillation cycle. On the other hand, using a 0.28 Lagrangian to Eulerian mesh width ratio the plate developed an artificial surface texture at the shortest wave number between its Lagrangian points. In subsequent studies, the time step was lowered to $\Delta t/4$, the initial amplitude of the mode shape was increased to x4 and x16, and the surrounding fluid density was amplified by 4 and 8 times to assess whether or not the divergence of the results of Case (b) using a 0.57 Lagrangian to Eulerian mesh width ratio could be avoided. However, the dynamics of the vibrating plate did not change with these alterations.

On the other hand, the results of Case (d) were numerically stable (at least for the duration of the simulation time before it was ended) and the errors in the results slightly decreased with increasing the Lagrangian points with a constant Eulerian grid size.

From these observations one might conclude that although no such limitation is apparent for the in-plane (extensional) dynamics, the simulation's out-of-plane (bending) dynamics favors a Lagrangian to Eulerian mesh width ratio as low as unity.

3.5.1.3 Effect of the ambient fluid's density

Keeping all the other parameters same, the ambient fluid density was changed to assess its effect on the results using the mode shape of Case (a) with 33^3 Eulerian grid points and 15^2 Lagrangian points. The presence of a finite ambient fluid density is expected to yield into slower natural frequencies due to its added mass effect on the vibrating plate. Note from Eqns. (3.5-1), (3.5-2), (3.5-3), and (3.5-4) that increasing mass decreases the natural frequencies. The results are presented in Table 3.5-7 below. In the computations the Lagrangian to Eularian mesh width ratio was approximately 1.

Table 3.5-7: Effect of ambient fluid's density on the computed natural frequency for the mode shape of Case (a), $\Delta t \approx 1.3\text{x}10^{-4}$ (1/ω)

Fluid density	Relative error	Convergence rate
ρ_f x 4	12.26 ±0.15 % slower	—
ρ_f x 2	10.03 ±0.15 % slower	0.29
ρ_f	8.69 ±0.15 % slower	0.21
ρ_f / 2	7.94 ±0.15 % slower	0.13
ρ_f / 4	7.50 ±0.15 % slower	0.08
ρ_f / 8	7.35 ±0.15 % slower	0.03

Based on the convergent trend in Table 3.5-7, it is clear that the effect of the ambient fluid density on the results disappears (relative to the other errors) as it is reduced. The results presented in Sections 3.5.1.1, 3.5.1.2, and 3.5.1.4 use an ambient fluid density ρ_f.

3.5.1.4 Effect of changing the Dirac-delta function width

As discussed in Section 3.2, the fluid/structure algorithm of the simulation uses spread Dirac-delta functions to represent the dynamics of a lower dimensional solid on a higher dimensional space. Although this current problem is not a fluid/structure interaction problem, the simulation still solves the two-dimensional plate's linear momentum equations in a three-dimensional space (using the Dirac-delta function form given in Eqns. (3.4-4) and (3.4-5)). In this study, the effect of the spreading width $2\varepsilon_\delta$ of the approximate Dirac-Delta function on the results is examined for the mode shape of Case (b) using 33^3 Eulerian and 15^2 Lagrangian grid points, corresponding to a Lagrangian to Eulerian mesh width ratio of 1.18. Since the formulation uses approximate Dirac-delta functions both in Eqn. (3.2-12) for desingularizing the lower dimensional quantities onto a higher dimensional space and in Eqn. (3.2-13) for approximating the velocities of the Lagrangian points, two different cases are considered:

1) Change ε_δ only in Eqn. (3.2-12) and use $\varepsilon_\delta = 2.0h$ for Eqn. (3.2-13),
2) Use the same ε_δ value for both Eqn. (3.2-12) and (3.2-13).

The results are given in Table 3.5-8 and Table 3.5-9 below.

Table 3.5-8: Effect of changing Dirac-delta function half width ε_δ in Eqn. (3.2-12) on the computed natural frequency for the mode shape of case (b), $\Delta t \approx 1.4\text{x}10^{-4}$ (1/ω)

Dirac-delta function half width ε_δ	Relative error	Stable?
1.5h	19.16 ±0.16 % slower	Yes
2.0h	8.79 ±0.16 % slower	Yes
3.0h	10.07 ±0.16 % slower	No
4.0h	—	No

Table 3.5-9: Effect of changing Dirac-delta function half width ε_δ in both Eqn. (3.2-12) and (3.2-13) on the computed natural frequency for the mode shape of case (b), $\Delta t \approx 1.4\text{x}10^{-4}$ (1/ω)

Dirac-delta function half width ε_δ	Relative error	Stable?
1.5h	6.72 ±0.16 % slower	No
2.0h	8.79 ±0.16 % slower	Yes
3.0h	19.32 ±0.16 % slower	Yes
4.0h	31.60 ±0.16 % slower	Yes

The results in Tables 3.5-8 and 3.5-9 suggest that the simulation is unstable if the Dirac-delta function half width ε_δ in Eqn. (3.2-12) is larger than that in Eqn. (3.2-13). On the other hand, using a large ε_δ in Eqn. (3.2-13) increases the relative error, possibly because approximating the velocity of a Lagrangian point from a higher number of Eulerian points damps-out the results. Not surprisingly, using $\varepsilon_\delta = 1.5h$ in both Eqn. (3.2-12) and Eqn. (3.2-13) gives a more accurate result than using $\varepsilon_\delta = 2.0h$ at the expense of lesser robustness.

From the above results, using $\varepsilon_\delta = 2.0h$ seems the best option and unless stated elsewhere the simulation will use this value.

3.5.2 Matching the static equilibrium position of a deflected beam

The aim of this study is to match the static equilibrium position of a one-dimensional deflected cantilever shaped beam. The main differences of this study compared to the previous one, in which the code was tested against the natural frequencies of a vibrating plate (Section 3.5.1), are: 1) the results of this problem are static shapes, not dynamic behavior, 2) the deformations are not limited to be small anymore, so we can test our solid model at the large deformation zones, 3) the solid is idealized as a one-dimensional beam in a two-dimensional space, and 4) the effect of the ambient fluid is not important on the steady-state results. The physical and numerical setups of this problem are as given in Fig. 3.5-2 below.

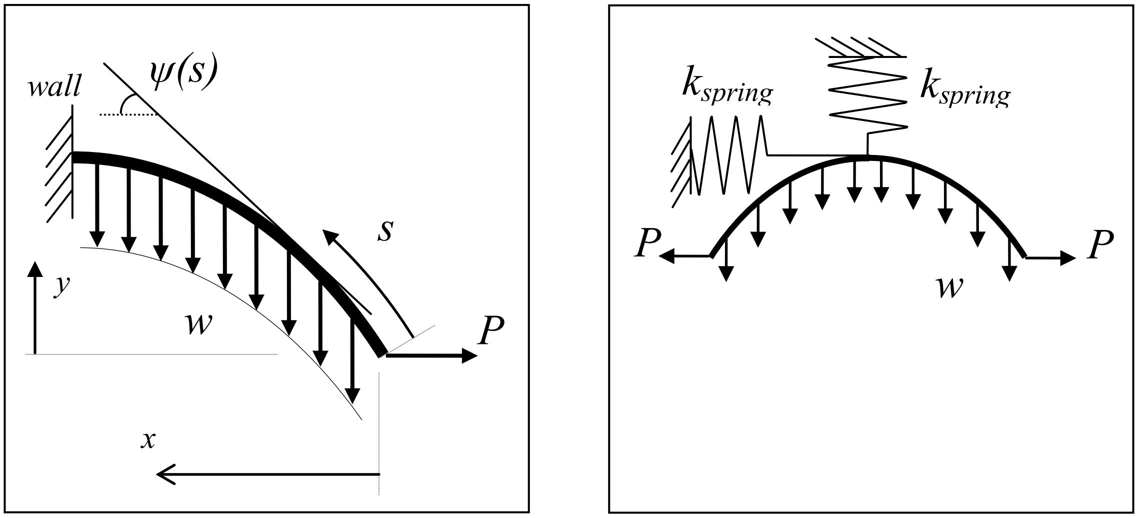

(a) (b)

Figure 3.5-2: Physical (a) and numerical (b) setups of the problem

In Fig. 3.5-2(a) we have a cantilever shaped beam with an arclength parameter *s*, a distributed vertical load *w*, and a horizontal force *P* on the beam's free end. The local slope of this beam is denoted by ψ. Following the derivation given by Bickley (1934), such an inextensible beam's static equilibrium position can be described by the solution of the following differential equations and boundary conditions

$$\begin{aligned}
&K_{bending}\frac{d^2\psi}{ds^2} = P\,sin\psi - w\,s\,cos\,\psi \\
&\frac{dx}{ds} = cos(\psi) \\
&\frac{dy}{ds} = sin(\psi) \\
&\psi(L) = 0, \quad \left.\frac{d\psi}{ds}\right|_{s=0} = 0, \quad x|_{s=0} = 0, \quad y|_{s=0} = 0
\end{aligned} \qquad \textbf{(3.5-5)}$$

In Eqn. (3.5-5) $K_{bending}$ is the bending stiffness of the solid, which is usually proportional to the cube of the beam's thickness (found as $\bar{E}q^3/12$ in Section 3.3.4, where $\bar{E}$ is the solid Young modulus and q is the thickness, but will be treated as a lumped parameter independent from $\bar{E}$ in the simulations), and L is the total length of the cantilever beam. Apart from being inextensible, Eqn. (3.5-5) was derived assuming the beam's internal moment is linearly proportional to its curvature by its bending stiffness, and shear deformations are negligible (Euler-Bernoulli's assumption). These two assumptions agree with the assumptions used in the solid models presented in Sections 3.3.3 and 3.3.4. In practice, the inextensibility can be enforced in the simulation by selecting a large Young's modulus. The first boundary condition states that the beam has a zero slope at the wall, whereas the second one enforces the beam's free-end to have zero curvature and hence moment. Furthermore, using the following dimensionless quantities

$$\begin{aligned} &\sigma = s/c, \quad \xi = x/c, \quad \eta = y/c \\ &\tau_o = P/wc \end{aligned} \qquad \textbf{(3.5-6)}$$

and by defining a 'bending length' c as

$$c = \sqrt[3]{\frac{K_{bending}}{w}} \qquad \textbf{(3.5-7)}$$

Bickley (1934) non-dimensionalizes Eqn. (3.5-5) as

$$\frac{d^2\psi}{d\sigma^2} = \tau_o \sin\psi - \sigma \cos\psi \qquad \textbf{(3.5-8)}$$

$$\psi\left(\sigma\big|_{s=L}\right) = 0, \quad \left.\frac{d\psi}{d\sigma}\right|_{\sigma=0} = 0, \quad \xi\big|_{\sigma=0} = 0, \quad \eta\big|_{\sigma=0} = 0$$

In our computations we use the setup shown in Fig. 3.5-2(b), where the beam is held at its midpoint and the right half is used to compare to the theory in Fig. 3.5-2(a). An initially flat beam is let to deform under the attached loads w and P in a viscous ambient fluid. The viscous fluid helps to damp-out the beam vibrations around its static equilibrium position. The stiffness of the springs shown in Fig. 3.5-2(b) are chosen high enough to restrict the movement of the midpoint, but low enough to let the simulations run with reasonable time steps. The reason for using such an implicit cantilever beam modeling is in the convenience of being able to keep using free end boundary conditions for the whole beam.

Throughout this study, τ_o and $\sigma_L = \sigma|_{s=L}$ are used as the physical control parameters. Using the definitions given in Eqns. (3.5-6) and (3.5-7) one can find

$$\sigma_L{}^3 = \frac{wL^3}{K_{bending}} \tag{3.5-9}$$

For the presentation of results, the 'theoretical' deformed beam shapes are compared to the computed ones. The 'theoretical' deformed shapes are found by numerically solving Eqn. (3.5-8) with MATLAB®'s 'ode45' differential equation solver. The absolute and relative error tolerances of 'ode45' were set to 10^{-15} and the solver was able to find a solution after increasing this error tolerance to $O(10^{-14})$. Since the nature of the differential equations of Eqn. (3.5-8) is a boundary-value problem, the value $\psi(0)$ was iterated to satisfy the first boundary condition given in Eqn. (3.5-8) within an absolute accuracy of $O(10^{-6})$.

As an error measure the root mean square difference between the 'theoretical' and computed deformed beam shapes on all the discrete points of the computations is used. The error is normalized by the length of the beam. In other words,

$$\text{Error} = \frac{1}{L}\left(\frac{1}{N_{beam}}\sum_{N_{beam}}\left(\left(X_{computed} - X_{exact}\right)^2 + \left(Y_{computed} - Y_{exact}\right)^2\right)\right)^{\frac{1}{2}}$$

where N_{beam} is the total number of all the discrete points used on the beam.

In the computations the Lagrangian to Eularian mesh width ratio was approximately 1. Also, the beam's Young's modulus and the midpoint's spring constant, k_{spring}, satisfy

$$\frac{\bar{E}}{wL} = 1.27x10^3, \quad \frac{k_{spring}L}{w} = 2.52x10^3$$

3.5.2.1 Effect of grid resolution on the beam shapes

We studied the effect of grid resolution on the results for the particular case of

$$\sigma_L{}^3 = 10, \quad \tau_o = 0$$

The results are given in Table 3.5-10 and Fig. 3.5-3 below, in which the 'theoretical' shapes are plotted with blue/dashed lines and the computed shapes are shown in red/solid lines. The convergence rate is defined as the slope of the line joining two points with coordinates $\left(\ln(h),\ \ln(\text{Error})\right)$, where h is the Eulerian mesh width.

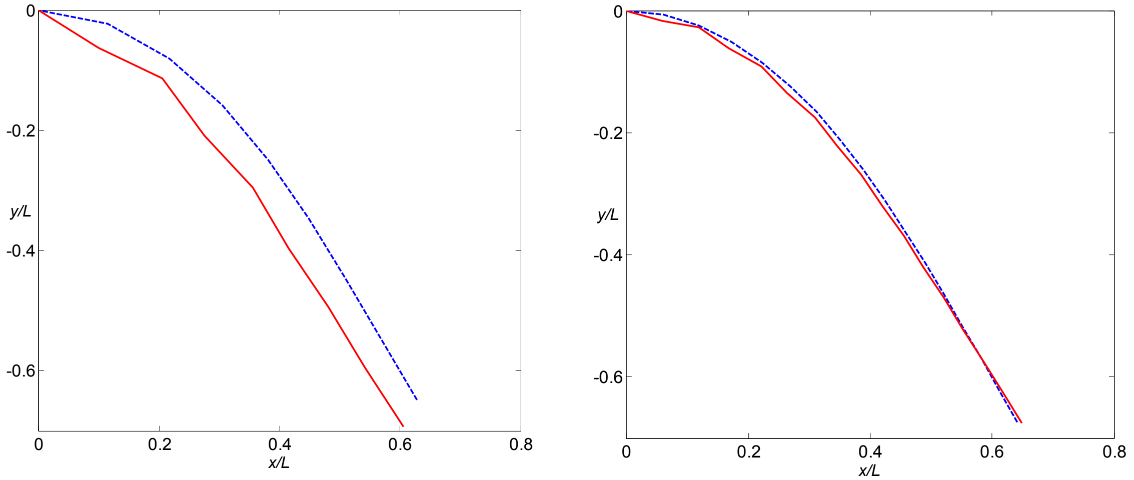

(a) $65^2/9$ (b) $129^2/17$

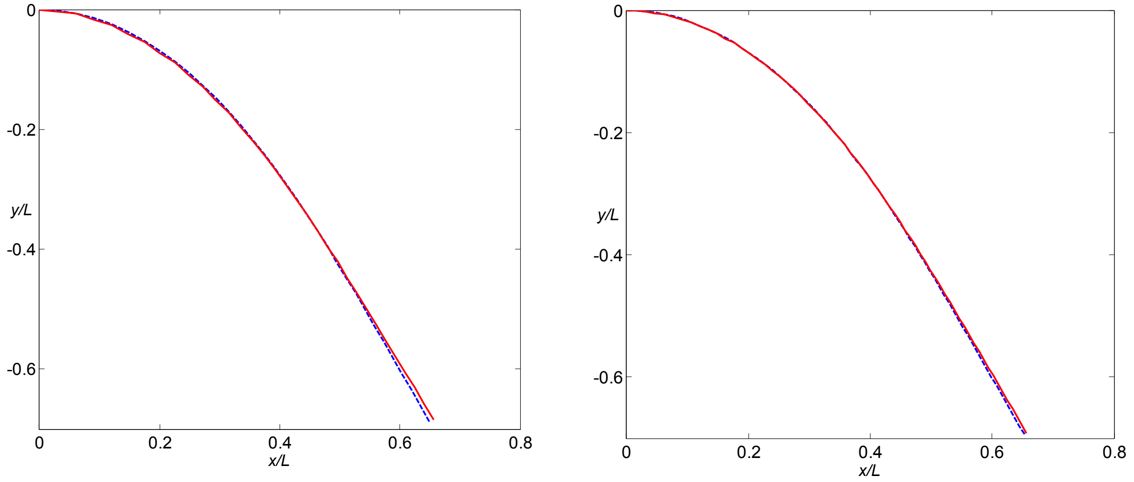

(c) $257^2/33$ (d)$513^2/65$

Figure 3.5-3: Effect of grid resolution on the beam shapes. The 'theoretical' shapes are plotted with blue/dashed and the computed shapes are shown in red/solid lines. The label '$65^2/9$' means the computation was done with 65 x 65 Eulerian and 9 Lagrangian points (on the half-beam, see Fig.3.5-2)

Table 3.5-10: Effect of the grid resolution on the computed beam shapes with σ_L^3 =10, τ_o=0

Eulerian grid size	Lagrangian points	Error	Convergence rate
65^2	9	$5.21\text{x}10^{-2}$	—
129^2	17	$8.5\text{x}10^{-3}$	2.65
257^2	33	$3.2\text{x}10^{-3}$	1.42
513^2	65	$1.9\text{x}10^{-3}$	0.75

As can be seen above, the results converge to the 'theoretical' shape with higher grid resolution.

3.5.2.2 Effect of changing τ_o on the beam shapes

We also studied the effect of choosing different τ_o values while using

$$\sigma_L{}^3 = 10 ,$$

with an Eulerian grid size of 513 x 513 and using 65 Lagrangian points on the half-beam. The results are shown in Fig. 3.5-4 in which the 'theoretical' shapes are plotted with blue/dashed lines and the computed shapes are shown in red/solid lines. As could be seen in the plot and in Table 3.5-11 the theoretical and computed beam shapes compare well. At high enough τ_o values most of τ_o acts as a tension force and the computed beam shapes have a higher elongation. On the other hand, at low τ_o values the beam is largely bent and in this case w is increasingly contributing to the beam tension, again causing higher extension. However, the 'theoretical' solution is based on a perfectly inextensible beam and this is why we think our results have a relatively lower error for intermediate τ_o values. Also note that, this study also benchmarks the coupled nonlinear effects of the bending moment and tension at the large deformation/small strain solid deformations.

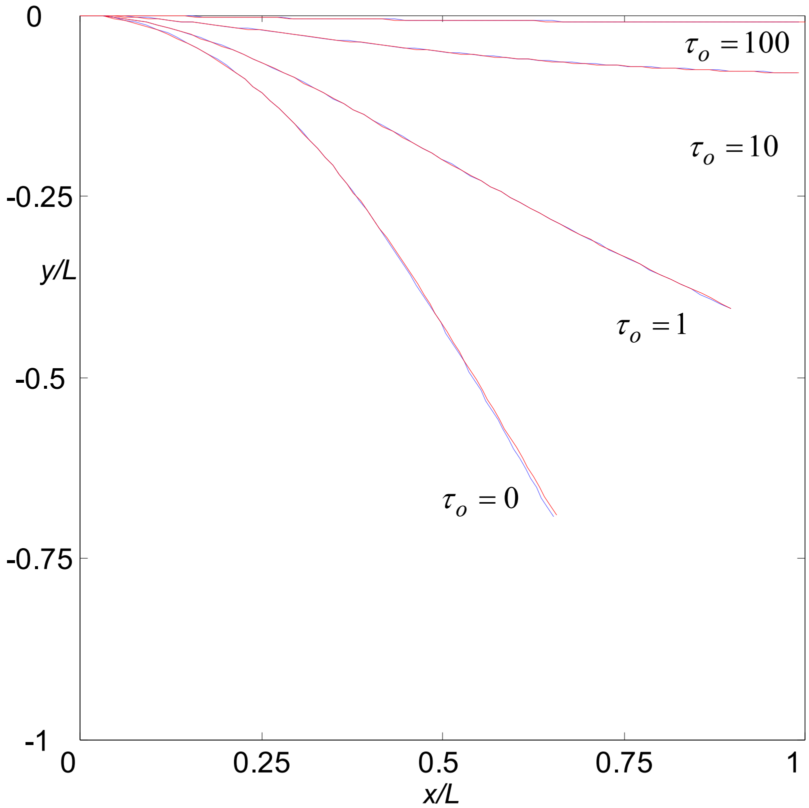

Figure 3.5-4: Effect of changing τ_o on the computed and 'theoretical' beam shapes with σ_L^3 =10. The 'theoretical' shapes are plotted with blue/dashed and the computed shapes are shown in red/solid lines.

Table 3.5-11: Effect of changing τ_o on the errors between the computed and 'theoretical' beam shapes with σ_L^3 =10

τ_o	**Error**
0	$1.9\text{x}10^{-3}$
1	$5\text{x}10^{-4}$
10	$2.15\text{x}10^{-3}$
100	$2.01\text{x}10^{-2}$

3.5.3 Simulating a fluttering plate as it descends in water

Beside the previous verification studies in which the solid model (Section 3.3) of the simulation was being tested, this study aims to test the coupled fluid/structure interaction model (Section 3.2) of the simulation. Unlike the abundant published results for elastic plate and beam behavior, there are fewer cases of a 'simple' coupled fluid/structure interaction that we could test our code. In this section the motion of a thin plate falling under its own weight in water is studied. It is known that light and thin sheets do not fall straight in air, which is the same case for heavier metal sheet in a heavier fluid such as water. Instead, their motion is enriched with fluttering, tumbling, and spinning. Studying this phenomenon has been of interest since the 19th century with Maxwell and it still continues to be. Since then this problem has been approached analytically, experimentally, and numerically. These studies further divide into two major categories. In the first one, researchers have been studying falling objects, whereas in the second category researches have been studying a pinned plate that is free to rotate around its center of mass in an external flow as an analogous but an easier setup. For a detailed literature survey interested readers could refer to the recent paper by Andersen et al. (2005) and the older review paper by Lugt (1983).

Recently, Belmonte et al. (1998) conducted a ‘quasi’ two-dimensional experiment in which they dropped plates between the two narrowly spaced walls of an aquarium. They also attached two rings to the plates’ ends to avoid any out-of-plane motions. In their study they reported a critical Froude number at which the plate switches from fluttering to tumbling. They defined this Froude number as the ratio of a time scale proportional to the period of a freely vibrating pendulum to another time scale proportional to the terminal velocity of a straightly descending object. They also stated that the Reynolds number does not significantly influence the motion above a threshold. Furthermore, they highlighted some universal similarities in phase plots of the plate’s speed components versus the dynamically changing descend angle. Later, Andersen et al. (2005) has conducted a set of experiments and offered a simplified model to describe the plate motion. In their experiments they dropped plates with a very high width to length ratio (more than 17), contrary to the study of Belmonte et al. (1998). As well as to the plate’s aspect ratio, they used the plate’s dimensionless moment of inertia value to characterize their results, which is proportional the square root of Belmonte et al. (1998)’s Froude number.

The setup of this problem is as shown in Fig. 3.5-5 below. This problem could be described by the gravitational constant g, water density ρ_f and viscosity μ, the plate length *l*, (out-of-plane) width *w*, thickness *q*, and excess two-dimensional mass density (with respect to water) ρ_s, whose measurement is as explained in Section 5.3.

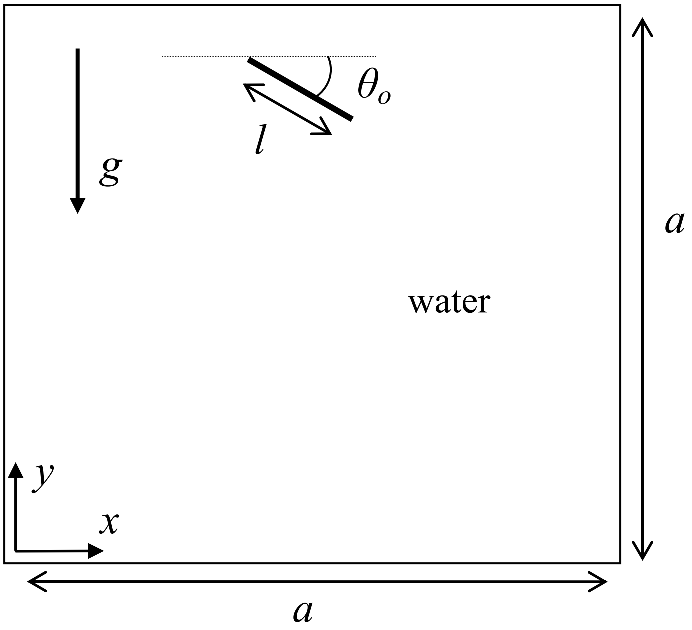

Figure 3.5-5: Initial setup for a plate descending in water

Using these variables Andersen et al. (2005) describes the problem with the following dimensionless parameters

$$Re = \frac{\rho_f l V}{\mu} \tag{3.5-10}$$

$$I = \frac{8}{3\pi}\left(\frac{\rho_s}{\rho_f} + q\right)\left(\frac{1}{l} + \frac{q^2}{l^3}\right) \tag{3.5-11}$$

$$\alpha = \frac{w}{l} \tag{3.5-12}$$

$$\beta = \frac{q}{l} \tag{3.5-13}$$

where

$$V = \sqrt{\frac{2\rho_s g}{\rho_f}} \tag{3.5-14}$$

In this study, an experiment was conducted with the dimensionless values given in Table 3.5-12 below. We used a camera at 15 fps to capture the motion of the plate.

Table 3.5-12: Dimensionless groups used in the experiment

Re	3189
I	0.123
α	3.9
β	0.06

Figure 3.5-6 below illustrates the stroboscopic plot of a two-dimensional simulation result with $h/l = 0.0108$, $a/l = 11.1$, and $\theta_o = 30°$, where h is the uniform Eulerian mesh width, a is as defined in Fig. 3.5-5 above, and θ_o is the initial descend angle from the horizontal. The time step value used in the simulations was such that $V\Delta t/h = 0.009$. The reason for doing the simulation in two-dimensions was the large cost of the three-dimensional simulations. Figure 3.5-7 shows the V_x vs. θ and $-V_y$ vs. θ plots, where V_x and V_y are respectively the horizontal (positive right) and vertical (positive upwards) components of the plate's center of mass velocity and θ is the dynamically changing descend angle of the plate with respect to the horizontal, as shown in Fig. 3.5-5 above.

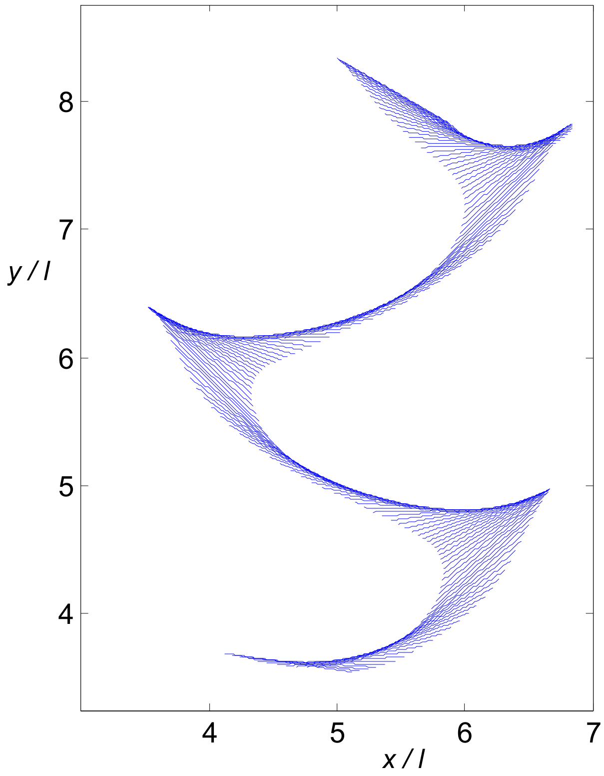

Figure 3.5-6: Stroboscopic plot of the computed motion of a fluttering plate as it descends in water with Re = 3189, I = 0.123, α = 3.9, β = 0.06 and using h/l = 0.0108, a/l = 11.1, θ_o = 30°

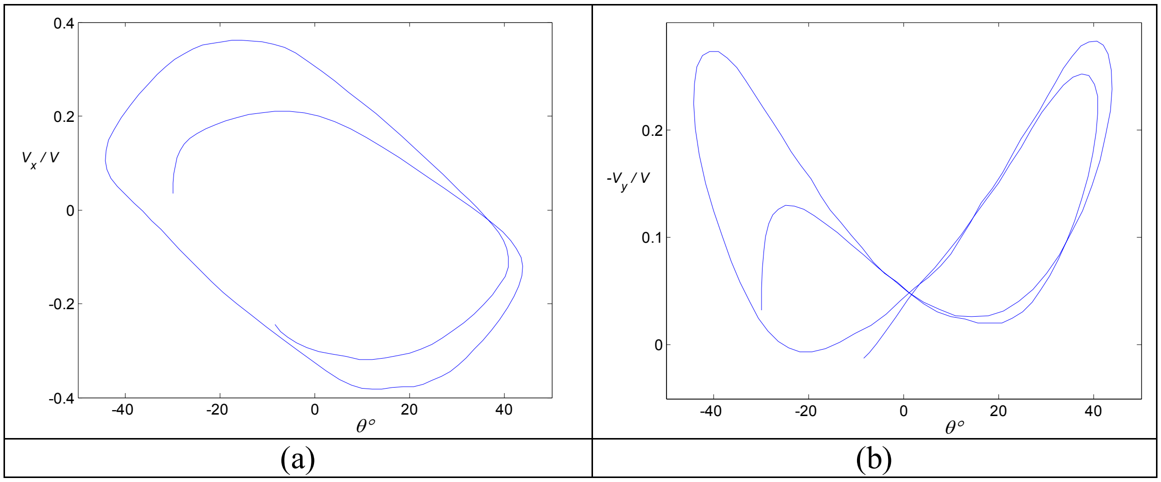

(a)

(b)

Figure 3.5-7: (a) V_x vs. θ , and (b) $-V_y$ vs. θ plots of the computed motion of a fluttering plate as it descends in water with Re = 3189, I = 0.123, α = 3.9, β = 0.06, a/l = 11.1, θ_o = 30° and using a grid resolution of h/l = 0.0108

While in our own experiments we find the half-oscillation period for the fluttering motion as 0.35±0.05 seconds, we found that value as 0.275 s (21 % slower than experiment) in the computations. This half-oscillation period is defined as the elapsed time as the plate moves between its farther right and left positions in Fig. 3.5-6. However, that value was as slow as 0.21 s (40 % slower than experiment) at a two times coarser grid with $h/l = 0.0216$. On the other hand, the shapes of the velocity components vs. θ phase plots (Fig. 3.5-7) agreed with what Belmonte et al. (1998) claim to be universally true shapes for a fluttering plate. Specifically, Belmonte et al. (1998) mention that for fluttering plates with a wide parameter range the minimum velocity components in both graphs approximately occur around 20° descend angle.

It is important mention that the α value used in this experiment (3.9) may not be large enough to compare the experiments with a two-dimensional computation. To address this issue and also to compare the simulation with other reported outputs than the half-oscillation period, we performed another computation to test the simulation with one of the experiments reported by Andersen et al. (2005), using the dimensionless groups given in Table 3.5-13 below.

Table 3.5-13: Dimensionless groups used in the fluttering plate experiment reported in Andersen et al. (2005)

Re	1147
I	0.16
α	16.75
β	0.0714

Figure 3.5-8 below illustrates the stroboscopic plot of the computational result with $h/l = 0.0086$, $a/l = 8.8$, and $\theta_o = 30°$. The time step value used in the simulations was such that $V\Delta t/h = 0.0165$.

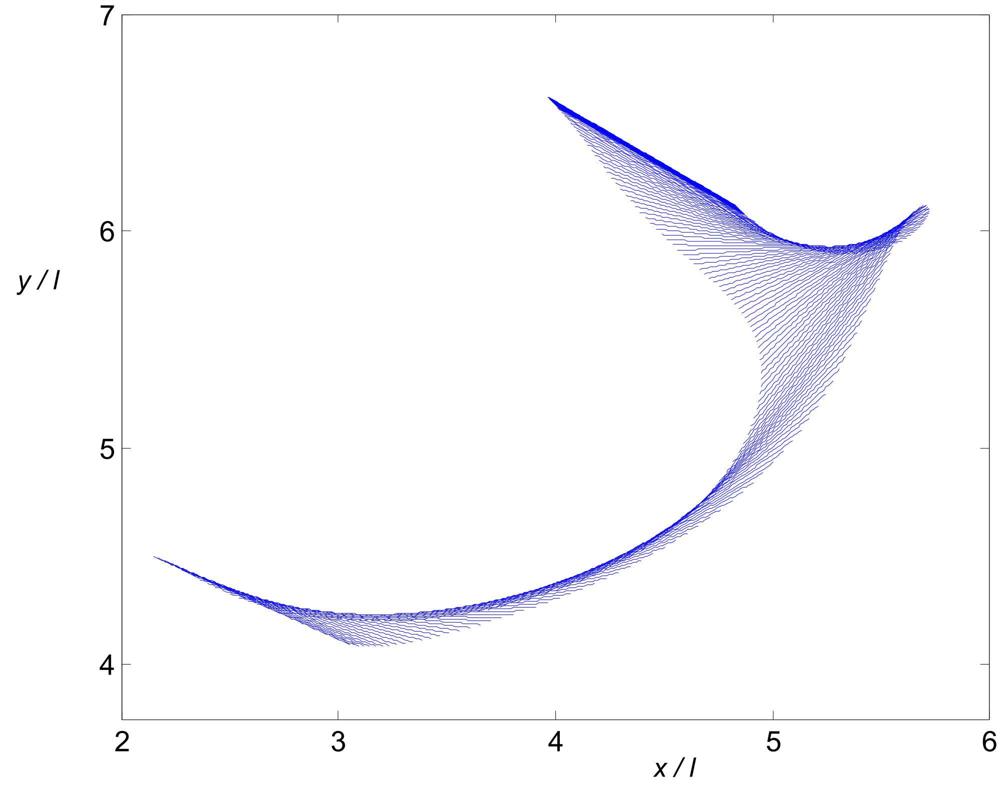

Figure 3.5-8: Stroboscopic plot of the computed motion of a fluttering plate as it descends in water with *Re* = 1147, I = 0.16, α = 16.75, β = 0.0714 and using *h*/*l* = 0.0086, *a*/*l* = 8.8, θ_o = 30°

For this case, time histories of the plate's center of mass velocity components are compared with the plots given in Andersen et al. (2005). Specifically, in the computations the amplitudes of the fluctuations of the horizontal and vertical components of the center of mass velocity were respectively 21 and 14 % slower than the values found in Andersen et al. (2005). However, at a two times coarser grid with *h*/*l* = 0.0172, *a*/*l* = 17.6 the same values were respectively 56 and 39 % slower than the values found in Andersen et al. (2005), showing a first-order convergence trend. On the other hand, the plate did not show a uniform fluttering pattern at coarser grids.

CHAPTER IV
REPRESENTING COMPLEX GEOMETRIES ON CARTESIAN GRIDS

4.1 Introduction

For a fluid domain with complex boundaries, simple structured grids cannot be used to discretize equations of motion without additional care. This is because the domain boundaries do not necessarily coincide with the grid positions. Such a situation is given in Figure 4.1-1, where a fluid domain Ω with an irregular boundary ∂Ω is shown together with a Cartesian grid.

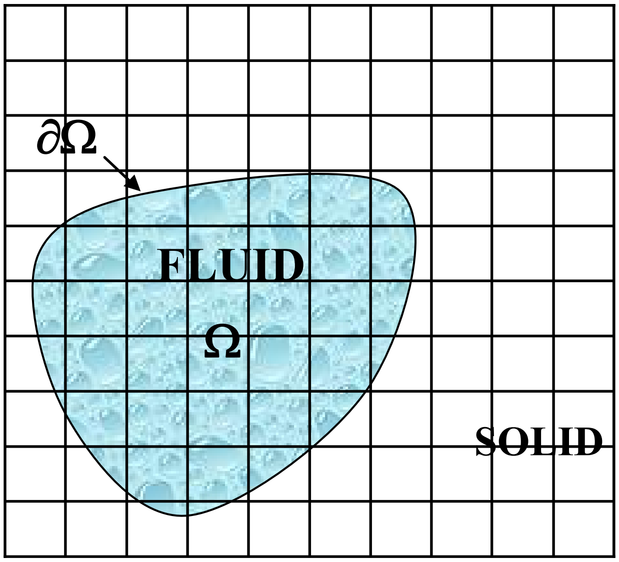

Figure 4.1-1: A fluid domain Ω with irregular boundaries ∂Ω on a Cartesian grid

Traditionally, such complex domains are discretized using unstructured grids with finite-volume or finite-element methods. Using unstructured grids, one can place the grid points in such a way that they coincide with the irregular boundaries. However, there are many non-trivial issues involving their construction as described in Ferziger and Peric (2002). Another traditional method is using curvilinear, boundary-fitted grids, which are also non-trivial to construct and cumbersome to use with multiple moving solid boundaries.

In the context of using structured grids with complex geometries, Morton and Mayers (1994) discusses a technique for general finite-differences that modifies the regular stencils near the complex boundaries at the expense of a restricted stability requirement, which also requires measuring distances from the Cartesian grid points to the boundaries along the horizontal and vertical grid lines. For inviscid flows, DeZeeuw et al. (1993) and Coirier et al. (1995) have attempted to model irregular solid boundaries with Cartesian grids using an adaptive mesh refining technique with a check criteria to decide when the mesh needs to be further refined. Later, Coirier et al. (1996) applied this technique to the Navier-Stokes equations. Ye et al. (1999) and Udaykumar et al. (2001) suggested a method for solving the Navier-Stokes equations that reshapes the structured grid-cells near the solid boundaries and requires performing interpolations to evaluate various fluxes leaving and entering those reshaped grid-cells. However, for complex or 3D geometries reshaping the grid-cells near the solid boundaries might be nontrivial and for problems involving moving boundaries these complex alterations would be repeated at every time step. A similar method formulated by Kirkpatrick et al. (2003) truncates the Cartesian cells near the solid boundaries.

Starting with Goldstein et al. (1993), other researchers have applied the Immersed Boundary method, which was presented in Chapter 3 for flexible solids in fluids, to model rigid irregular domain boundaries. In particular, Goldstein et al. (1993) suggested covering both the fluid and solid regions with the same regular grid and using an excess force field near the boundaries to satisfy the no-slip and no-penetrability condition there. Literally, for the Navier-Stokes equations he offered is

$$
\begin{aligned}
&\rho\left(\frac{\partial \mathbf{u}}{\partial t}+\mathbf{u}\circ\nabla\mathbf{u}\right)=-\nabla p+\mu\nabla^{2}\mathbf{u}+\mathbf{f}\\
&\nabla\circ\mathbf{u}=0\\
&\mathbf{f}=\alpha\int_{0}^{t}\left(\mathbf{u}\big|_{\partial\Omega}-\mathbf{u_b}\right)dt+\beta\left(\mathbf{u}\big|_{\partial\Omega}-\mathbf{u}_b\right)\\
&\alpha,\beta<0
\end{aligned}
\qquad \textbf{(4.1-1)}
$$

where $\mathbf{u}\big|_{\partial\Omega}$ is the actual velocity and $\mathbf{u}_b$ is the desired velocity at the boundary $\partial\Omega$. This formulation resembles a simple spring-damper system and the free constants α and β can be viewed as the solid boundary 'spring' and 'damping' constants. However, as Goldstein et al. (1993) indicate, this formulation needs to be calibrated for each different problem to ensure the numerical natural frequency of the elastic boundary to be as different as possible from the physical flow frequencies. On the other hand, using a stiffer 'spring' constant would add to the numerical stability concerns. Next, Mohd-Yusof (1997) and Fadlun et al. (2000) used the following alternative to Goldstein et al. (1993):

$$
\begin{aligned}
&\rho\left(\frac{\mathbf{u}^{n+1}-\mathbf{u}^{n}}{\Delta t}+\mathbf{u}\circ\nabla\mathbf{u}\right)=-\nabla p+\mu\nabla^{2}\mathbf{u}+\mathbf{f}\\
&\nabla\circ\mathbf{u}=0\\
&\mathbf{f}=\rho\left(\frac{\mathbf{u}_b^{n+1}-\mathbf{u}^{n}}{\Delta t}+\mathbf{u}\circ\nabla\mathbf{u}\right)+\nabla p-\mu\nabla^{2}\mathbf{u}\quad \text{on } \partial\Omega
\end{aligned}
\qquad \textbf{(4.1-2)}
$$

which doesn't require any numerical 'spring' and 'damping' constant values. An exact evaluation of Eqn. (4.1-2) gives

$$
\begin{aligned}
&\rho\left(\frac{\mathbf{u}^{n+1}-\mathbf{u}^{n}}{\Delta t}+\mathbf{u}\circ\nabla\mathbf{u}\right)=-\nabla p+\mu\nabla^{2}\mathbf{u}\quad \text{in } \Omega\\
&\mathbf{u}^{n+1}=\mathbf{u}_b\quad \text{on } \partial\Omega\\
&\nabla\circ\mathbf{u}=0
\end{aligned}
$$

Fadlun et al. (2000) use a linear interpolation scheme to couple the boundary velocity $\mathbf{u}_b$ with the regular structured grid points. However, the interpolation direction choices can be shown to be non-unique. The authors claimed their method to be second-order accurate in space. Kim et al. (2001) offered a technique assigning the mirror image of the fluid velocity near a stationary boundary to the grid points inside the solid, so the fluid velocity on $\partial\Omega$ is zero. For non-stationary boundaries their method extrapolates the fluid velocity to the grid points inside the solid. They also enforced mass conservation near the boundaries with special mass sinks or sources and reported significantly lower errors. For cases with and without enforcing mass conservation near the boundaries, they reported second-order spatial accuracy. In a similar method to Fadlun et al. (2000) and Kim et al. (2001), Tseng et al. (2003) extrapolated the fluid variables to the grid points inside the solid in such a way that both the velocity and pressure boundary conditions are satisfied on the solid surface. Yokoi (2003) published a similar method to Tseng et al. (2003), using level-set representation for the solid boundary to ease the formulation of extrapolations. However, he didn't extend his method for the pressure-correction part of solving the Navier-Stokes equations and he reports first-order accuracy in space. Silva et al. (2003) calculated the force $\mathbf{f}$ in Eqn. (4.1-2) on the discretized boundary surface by interpolating the required quantities from the structured grid to do so and then interpolated $\mathbf{f}$ back to the structured grid points. Recently, Marella et al. (2005) suggested another method, which is claimed to be second-order accurate in space. Their technique uses the level-set formulation to represent the solid boundaries, which in turn enables the convenient computation of the closest distance between the solid boundary and each neighboring structured grid point. Using these closest distances the authors formulated an automated scheme that locally modifies the finite-difference approximations near the solid boundaries.

4.2 Current approach

In this study a spatially less than second-order accurate method (in terms of its convergence properties) has been implemented for representing the complex geometries of the washing machine on Cartesian grids. Note that, it would be meaningless to adopt a spatially second-order accurate method for this problem while the fluid-structure interaction part of the simulation code is first-order accurate. However, as will be discussed later, the currently used method could be modified to be second-order accurate (similar to the technique of Kim et al. (2001)) with little extra effort. Therefore, this work will serve as a useful background for further improvements.

The solid boundary interface is described in such a way that at all times it corresponds to the zero level-set/contour of a scalar function that is defined on all grid points. Using such a description, the shortest distance between every grid point to the solid boundary is computed using Eqn. (4.2-1) as suggested by Sussman et al. (1994).

$$\frac{\partial \phi}{\partial t^*} + |\nabla \phi| \operatorname{sgn}\phi^o = \operatorname{sgn}\phi^o \qquad \textbf{(4.2-1)}$$

where ϕ is the scalar function whose zero level-set is on the solid boundary and also is a distance function. On the other hand, ϕ^o is also a scalar function whose zero level-set is on the solid boundary, but is not necessarily a distance function. ϕ^o is the result of the construction of the level-set function by combining simple geometric shapes. Additionally, t^* is an artificial time variable that serves as an iteration parameter for solving Eqn. (4.2-1) to steady-state. For computing the solution of Eqn. (4.2-1), ϕ^o is set to be the initial condition of ϕ. Lastly, sgnϕ^o is the sign function of ϕ^o, which is equal to 1 if $\phi^o > 0$, -1 if $\phi^o < 0$, and 0 if $\phi^o = 0$. Note that, the steady-state condition of Eqn. (4.2-1) is

$$\left(|\nabla \phi| - 1\right) \operatorname{sgn}\phi^o = 0 \quad \Leftrightarrow \quad |\nabla \phi| = 1 \qquad \textbf{(4.2-2)}$$

which implies ϕ is the signed distance function of the solid boundary. In the simulation, the solution of Eqn. (4.2-1) is computed through a spatially first-order, consistent and monotone scheme that is known to be converging to a unique ‘viscosity solution’, as used by Sussman et al. (1994). Specifically, the simulation solves Eqn. (4.2-1) in 2D, using Russo et al. (2000)'s notation, as

$$\phi_i^{n+1} = \phi_i^n - \Delta t^* G(\phi)_i \operatorname{sgn}\phi_i^o \qquad \textbf{(4.2-3)}$$

where

$$G(\phi)_i = \begin{cases} \sqrt{max\left(a_+{}^2, b_-{}^2\right) + max\left(c_+{}^2, d_-{}^2\right)} - 1 & \text{if } \phi_i^{\text{o}} > 0 \\ \sqrt{max\left(a_-{}^2, b_+{}^2\right) + max\left(c_-{}^2, d_+{}^2\right)} - 1 & \text{if } \phi_i^{\text{o}} < 0 \end{cases}$$

with

$$a = \frac{\phi_{i,j} - \phi_{i-1,j}}{h}, \quad b = \frac{\phi_{i+1,j} - \phi_{i,j}}{h}, \quad c = \frac{\phi_{i,j} - \phi_{i,j-1}}{h}, \quad d = \frac{\phi_{i,j+1} - \phi_{i,j}}{h}$$

$$\alpha_+ = \max\left(\alpha, 0\right), \quad \alpha_- = \min\left(\alpha, 0\right) \quad \text{for any real number } \alpha$$

and $\phi_{i,j}$ denotes the value of ϕ at the $(i, j)^{\text{th}}$ grid point location (see Fig. 2.2-2). As before h is the uniform grid spacing. The 3D formulation is analogous and is not explicitly repeated here. In their paper, Russo et al. (2000) report that the above scheme for solving Eqn. (4.2-1) has a deficiency of shifting the true position of the zero level-set location of ϕ to the nearest grid point, and they suggested an improved scheme. Although it is simple, this fix has not been implemented yet in the current simulation code.

Having described the solid boundary with such a signed distance function, the computational domain is divided into fluid and rigid solid regions as in Fig. 4.1-1. The initial level-set function is chosen such that it is negative inside the rigid solid domain Ω_s and positive inside the fluid domain Ω_f . For the fluid and solid domains one can write

$$\left.\begin{array}{l}\rho\left(\dfrac{\partial \mathbf{u}}{\partial t}+\mathbf{u}\circ\nabla\mathbf{u}\right)=-\nabla p+\mu\nabla^{\mathbf{2}}\mathbf{u}+\mathbf{f}\\ \nabla\circ\mathbf{u}=0\end{array}\right\}\text{ in }\Omega_{\mathrm{f}} \qquad \mathbf{(4.2\text{-}4)}$$

and

$$\left.\begin{array}{l}\mathbf{u}=\mathbf{u}_{solid}\\ \nabla\circ\mathbf{u}=0\end{array}\right\}\text{ in }\Omega_{\mathrm{s}} \qquad \mathbf{(4.2\text{-}5)}$$

Note that $\nabla\circ\mathbf{u}=0$ is true for rigid body motions. In this study, Eqns. (4.2-4) and (4.2-5) are augmented as a single equation for both Ω_s and Ω_f as

$$\left.\begin{array}{l}\left[\rho\left(\dfrac{\partial \mathbf{u}}{\partial t}+\mathbf{u}\circ\nabla\mathbf{u}\right)+\nabla p-\mu\nabla^{\mathbf{2}}\mathbf{u}-\mathbf{f}\right]H(\phi)+k\left[\mathbf{u}\text{-}\mathbf{u}_{solid}\right]\left(1-H(\phi)\right)=\mathbf{0}\\ \nabla\circ\mathbf{u}=0\end{array}\right\}\text{ in }\Omega:\Omega_f\cup\Omega_s$$

(4.2-6)

where $H(\phi)$ is the Heaviside function of ϕ; being 0 if ϕ is negative, 1 if ϕ is positive and 1/2 if ϕ is zero. In Eqn. (4.2-6) k is a free constant having units of mass/ (time x length^3).

In the present simulation k was selected in such a way that the diagonal term of the set of linear equations given in Chapter 2's Eqns. (2.2-22) or (2.2-23) is same in both fluid and solid. As described there, solving Eqn. (2.2-22) is a part of the solving the Navier-Stokes equations and the iterative solver of that set of equations favors the eigenvalues of the matrix to be clustered, which is assured by selecting k as explained above.

The formulation given in Eqn. (4.2-6) with using a discontinuous Heaviside function will result in a stair shaped non-smooth interface, but will converge to the true geometry as the grid is refined. To test if this formulation could be improved by diffusing the solid interface onto a few grid points along the normal direction of the interface, a modified Heaviside function $\tilde{H}(\phi)$ is also used for $H(\phi)$ as

$$\tilde{H}(\phi)=\begin{cases} 0 & \text{if } \phi<-\varepsilon \\ \frac{1}{2}+\frac{1}{2}\left(\frac{\phi}{\varepsilon}+\frac{1}{\pi}\sin\left(\frac{\pi\,\phi}{\varepsilon}\right)\right) & \text{if } |\phi|\le\varepsilon \\ 1 & \text{if } \phi>\varepsilon \end{cases}$$

where 2ε is the width of the smooth interface and is selected to be 4 grid spacings (note that the original $H(\phi)$ uses $\varepsilon = 0$). As will be shown in the next section, the 'diffuse' interface was not any more accurate than the 'sharp' interface, at least for the test cases of Section 4.3.1 and 4.3.2 on coarse grids. Another idea is to set ε to include more and more grid points as the grid is refined. However, test cases showed that it is again no better than that of the 'sharp' interface. Hence, in the washing machine simulations the simulation uses the 'sharp' Heaviside function. Although, the idea of Eqn. (4.2-6) is also in Al-Rawahi et al. (2002) and Son (2005), it was independently developed here.

In the scope of using a fractional step method to solve the Navier-Stokes equations, Eqn. (4.2-6) could be solved through the following steps:

1. Compute $\mathbf{u}^*$ from

$$\left[\rho\left(\frac{\mathbf{u}^*-\mathbf{u}^n}{\Delta t}+\frac{3}{2}\mathbf{u}^n\circ\nabla\mathbf{u}^n-\frac{1}{2}\mathbf{u}^{n-1}\circ\nabla\mathbf{u}^{n-1}\right)+\nabla p^{n-\frac{1}{2}}-\frac{1}{2}\mu\nabla^{\mathbf{2}}\left(\mathbf{u}^*+\mathbf{u}^n\right)-\mathbf{f}\right]H(\phi)$$
$$+k\left[\mathbf{u}^*-\mathbf{u}_{solid}\right]\left(1-H(\phi)\right)=\mathbf{0}$$

(4.2-7)

with the following boundary conditions

$\mathbf{u}^* = \mathbf{u}_b$ on the grid boundaries

2. Observe that

$$\mathbf{u}^* = \mathbf{u}^{n+1} + H(\phi)\frac{\Delta t}{\rho}\nabla\tilde{p} \qquad \textbf{(4.2-8)}$$

where $\nabla \circ \mathbf{u}^{n+1} = 0$. This equation is the generalized Hodge/Helmholtz decomposition and is true because in the solid domain Ω_s Eqn. (4.2-7) sets $\mathbf{u}^* = \mathbf{u}_{solid}$, and $\mathbf{u}^{n+1}$ is also desired to be equal to $\mathbf{u}_{solid}$.

3. Compute $\tilde{p}$ (up to an arbitrary constant) from

$$\nabla \circ \left(\frac{H(\phi)}{\rho} \nabla\tilde{p} \right) = \frac{1}{\Delta t}\nabla \circ \mathbf{u}^* \qquad \textbf{(4.2-9)}$$

by using

$\nabla\tilde{p} \circ \mathbf{n} = 0$

at the grid boundaries if the fluid domain has access to there. If the fluid domain has no access to there, no boundary condition is necessary, but for simplicity the above boundary condition could be retained in the simulation, since it will have no adverse effect.

4. Compute $\mathbf{u}^{n+1}$ from

$$\mathbf{u}^{n+1} = \mathbf{u}^* - H(\phi)\frac{\Delta t}{\rho}\nabla\tilde{p} \qquad \textbf{(4.2-10)}$$

5. Lastly, compute the real pressure p from

$$p^{n+\frac{1}{2}} = p^{n-\frac{1}{2}} + \widetilde{p}^{n+1} - \frac{\Delta t \mu}{2\rho} \nabla^2 \widetilde{p}^{n+1} \tag{4.2-11}$$

Note that, Eqns. (4.2-7) to (4.2-11) are analogous to those presented in Chapter 2 for solving the Navier-Stokes equations in 'all-fluid' domains. Instead of these illustrative differential forms of Eqns. (4.2-7) and (4.2-9), the simulation uses their integral forms in the computations as discussed in Chapter 2, but the main idea is same. It is noteworthy that Eqn. (4.2-9) is the Poisson equation with a non-constant coefficient $H(\phi)/\rho$, changing from 0 to $1/\rho$. Hence, the computational difficulty of solving Eqn. (4.2-9) is equivalent to solving a multiphase flow with an infinite density jump. The computational difficulty of solving elliptic partial differential equations with non-constant coefficients by using Geometric Multigrid methods is discussed in Briggs et al. (2000). To avoid this complication, one could truncate $H(\phi)$ at a positive small value inside the solid domain for Eqn. (4.2-9) and (4.2-10), before it reaches to zero. Due to the computational difficulty of solving Eqn. (4.2-9), even with truncating $H(\phi)$ at a positive small value, the simulation rather solves the following equations instead of Eqn. (4.2-9) and (4.2-10) for the washing machine simulations:

$$\nabla \circ \left(\frac{1}{\rho} \nabla \tilde{p} \right) = \frac{1}{\Delta t} \nabla \circ \mathbf{u}^* \tag{4.2-12}$$

with

$\nabla \tilde{p} \circ \mathbf{n} = 0$ at the grid boundaries

and

$$\mathbf{u}^{n+1} = \mathbf{u}^* - \frac{\Delta t}{\rho} \nabla \tilde{p} \tag{4.2-13}$$

which are the original fractional step sequence equations that are used to solve the Navier-Stokes equations in 'all-fluid domains' as presented in Chapter 2. Using Eqns. (4.2-12) and (4.2-13) rather than Eqns. (4.2-9) and (4.2-10) is substantially cheaper. Although $\mathbf{u}^* = \mathbf{u}_{solid}$ is implied by Eqn. (4.2-7), $\mathbf{u}^{n+1} = \mathbf{u}_{solid}$ is not explicitly implied anymore by using Eqns. (4.2-12) and (4.2-13). However, as long as $\mathbf{u}_{solid}$ is constructed in such a way that $\nabla \circ \mathbf{u}_{solid} = 0$, Eqn. (4.2-12) would imply $\nabla \tilde{p} = 0$ in Ω_s and hence Eqn. (4.2-13) would implicitly give $\mathbf{u}^{n+1} = \mathbf{u}_{solid}$ in Ω_s.

4.3 Verification

4.3.1 Simulating 2D circular Couette flow

In this verification study, the simulation's method of representing complex geometries on Cartesian grids is tested against steady, axisymmetric Couette flow. The setup is as shown in Fig. 4.3-1, where the Cartesian grid is also plotted. In this flow, a fluid is enclosed between two circular and concentric inner and outer walls whose radii are respectively r_i and r_o. In addition, the inner and outer walls are rotating counterclockwise with angular speeds of Ω_i and Ω_o, respectively. θ is the angle measured counterclockwise from the x-axis, which spans horizontally right from the common center of the cylinders. The exact solution is

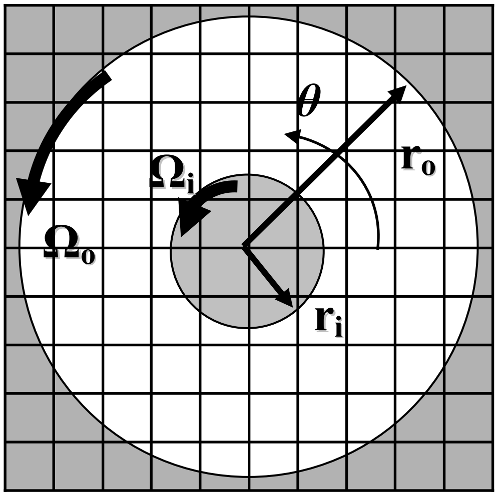

Figure 4.3-1: 2D circular Couette flow with a Cartesian grid

$$\mathbf{u} = u_\theta \mathbf{e_\theta}$$
$$u_\theta = Ar + \frac{B}{r} \qquad \textbf{(4.3-1)}$$

where

$$A = \frac{\Omega_i r_i^2 - \Omega_o r_o^2}{r_i^2 - r_o^2}, \quad B = \frac{r_i^2 r_o^2}{r_i^2 - r_o^2}\left(\Omega_o - \Omega_i\right)$$

In Eqn. (4.3-1) u_θ and $\mathbf{e_\theta}$ are respectively the velocity component and unit vector in the positive θ direction. This result is from the simplified form of the Navier-Stokes equations

$$\frac{\partial^2 u_\theta}{\partial r^2} + \frac{1}{r}\frac{\partial u_\theta}{\partial r} - \frac{u_\theta}{r^2} = 0 \qquad \textbf{(4.3-2)}$$

The constants *A* and *B* are determined by applying the no-slip boundary conditions at the inner and outer walls. It is noteworthy that Eqn. (4.3-2) contains only the diffusive terms of the Navier-Stokes equation.

We choose the following length, time and mass scales to non-dimensionalize this problem

$$l^o = r_o - r_i, \quad t^o = \frac{r_o - r_i}{r_o \omega_o}, \quad M^o = \rho_f \left(r_o - r_i\right)^3 \tag{4.3-3}$$

The Navier-Stokes equations for the 2D circular Couette flow geometry is written in the following dimensionless form

$$\begin{aligned} &\frac{\partial \mathbf{u}}{\partial t} + \mathbf{u} \circ \nabla \mathbf{u} = -\nabla p + \frac{1}{Re} \nabla^2 \mathbf{u} \\ &\nabla \circ \mathbf{u} = 0 \end{aligned} \tag{4.3-4}$$

where the Reynolds number *Re* is defined as

$$Re = \frac{\rho \, (r_o \omega_o)(r_o - r_i)}{\mu} \tag{4.3-5}$$

This form of the Navier-Stokes equations includes all the terms excluded in Eqn. (4.3-2), since this is what the simulation solves for. Specifically, in the simulations the inner and outer walls' angular velocities are suddenly applied at $t = 0$ as

$$\Omega_i = \bar{\Omega}_i H(t), \quad \Omega_o = \bar{\Omega}_o H(t) \tag{4.3-6}$$

where H is a Heaviside function and the simulation marches towards the steady-state solution given in Eqn. (4.3-1). The other dimensionless scales defining this problem are

$$\frac{\Omega_i}{\Omega_o} \text{ and } \frac{r_i}{r_o}$$

In this study, in addition to testing the general validity of the method of representing complex solid boundaries on Cartesian grids, the effect of the Heaviside function thickness ε (see Section 4.2) will also be assessed on the accuracy of the results.

4.3.1.1 Effect of the Heaviside function thickness 2ε

In this test case, the effect of the modified Heaviside function thickness 2ε in Eqn. (4.2-6) is tested. The following physical and numerical parameters are used:

$$Re = 131, \quad \frac{\Omega_i}{\Omega_o} = 6.13, \quad \frac{r_i}{r_o} = 0.34, \quad \Delta t = 2.5x10^{-3}$$

The maximum CFL number at the finest grid was 0.6156. Using the definitions of the maximum and the rms errors as in Eqn. (4.3-7) and (4.3-8) below, where N is the total number of grid points in the fluid domain, Tables 4.3-1 and 4.3-2 report the results with $\varepsilon = 0$ and $\varepsilon = 2h$, respectively. The convergence rate is defined as the slope of the line joining two points with coordinates $\left(\ln(h),\ \ln(\text{Error})\right)$, where h is the Eulerian mesh width.

$$\text{Maximum error: } max\left(\frac{u_\theta^{computed} - u_\theta^{exact}}{u_\theta^{exact}}\right) \tag{4.3-7}$$

$$\text{Rms error: } \left(\frac{1}{N}\sum_{\mathrm{i}=1}^{N}\left(\frac{u_\theta^{computed} - u_\theta^{exact}}{u_\theta^{exact}}\right)_i^2\right)^{\frac{1}{2}} \tag{4.3-8}$$

Table 4.3-1: Effect of the grid resolution on the accuracy of the 2D steady, laminar, and circular Couette flow with $\varepsilon = 0$

Eulerian grid size	h/r_i	Maximum error	Convergence Rate	Rms error	Convergence Rate
129^2	0.0646	0.0365	–	0.0105	–
257^2	0.0324	0.0309	0.24	$7.95\text{x}10^{-3}$	0.40
513^2	0.0162	0.012	1.4	$3.47\text{x}10^{-3}$	1.2

Table 4.3-2: Effect of the grid resolution on the accuracy of the 2D steady, laminar, and circular Couette flow with $\varepsilon = 2h$

Eulerian grid size	h/r_i	Maximum error	Convergence Rate	Rms error	Convergence Rate
129^2	0.0646	0.1133	–	0.0469	–
257^2	0.0324	0.04	1.5	0.0167	1.5
513^2	0.0162	0.01	2.0	$4.0\text{x}10^{-3}$	2.1

In Tables 4.3-1 and 4.3-2 above, h/r_i is the ratio between the grid size and the maximum radius of curvature of the solid boundaries. Note that the overall convergence rate with $\varepsilon = 2h$ appears higher than that of $\varepsilon = 0$. On the other hand, on coarser grids the method with $\varepsilon = 0$ produces significantly lower errors.

4.3.1.2 Comparison with method of Yokoi (2003)

In this study the method of Yokoi (2003) was also coded and tested against the current formulation. It is worth mentioning that starting from the current formulation it is possible to adapt the formulations of Yokoi (2003) and Kim et al. (2001) with a very little extra effort. The method of Yokoi (2003) can be summarized as

1. Identify an Eulerian grid point in the solid domain Ω_s,
2. Compute the vector $\nabla\phi/|\nabla\phi|$ between the closest point on the solid/fluid interface and the grid point,
3. Originating from the same grid point in solid, mark a point in the fluid domain Ω_f that is $|\phi| + h$ away from the grid point along the $\nabla\phi/|\nabla\phi|$ direction ,
4. Using bilinear (in 2D) or trilinear (in 3D) interpolations compute the velocity at the marked point in fluid,

5. Finally, using the velocities of the marked fluid point and the solid/fluid interface, extrapolate the fluid velocity field to the solid grid point along the $\nabla\phi/|\nabla\phi|$ vector direction.

Using the method of Yokoi (2003), the maximum error defined in Eqn. (4.3-7) was 0.0215 and the rms error defined in Eqn. (4.3-8) was 0.0040 on a 129 x 129 Eulerian grid. Observe that these errors are significantly lower than those computed with the current method using Heaviside functions in Tables 4.3-1 and 4.3-2. However, the method of Yokoi (2003) is not being used in the simulation for the washing machine simulations. This is because Yokoi's method uses the interface normal vector $\nabla\phi/|\nabla\phi|$, but for the three-dimensional washing machine simulations using coarse-grids this interface normal vector estimate was poor causing fictitious oscillations in the velocity field near the solid boundary (See Chapter 5, Figure 5.5-4 for this geometry).

4.3.2 Simulating a 2D flow past a circular cylinder

Unlike the 2D, steady, laminar and axisymmetric Couette flow, the fluid flow past a circular cylinder bears the coupled effects of pressure, diffusion and convection in its physics. In this problem, using a Reynolds number *Re* based on the cylinder diameter, Ye et al. (1999) mentions that for flows with *Re* greater than approximately 46 the wake behind the cylinder is unstable and vortices are shed at a certain frequency. The numerical setup of this problem is as given in Fig. 4.3-2 below.

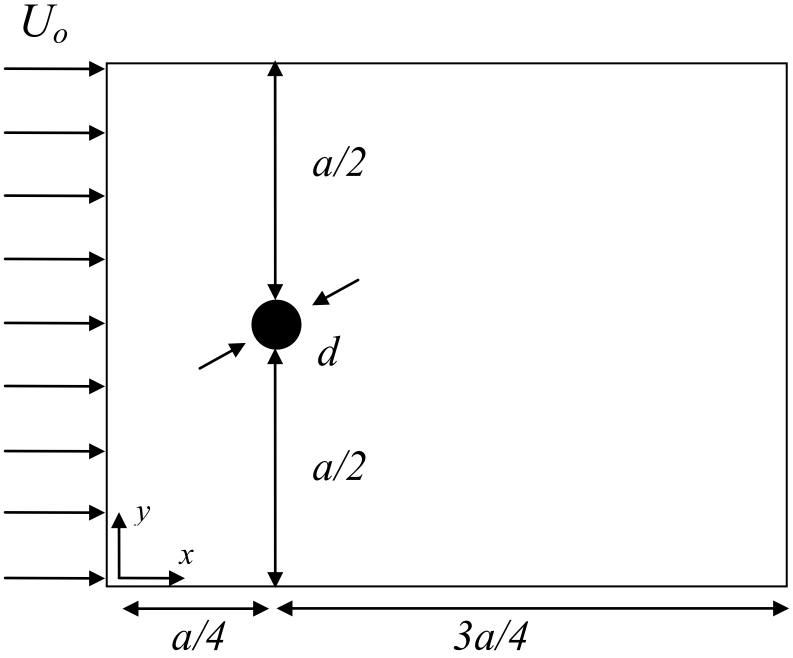

Figure 4.3-2: Numerical setup of the simulations of a 2D flow past a circular cylinder

This problem is nontrivial because the numerical domain has a finite size and appropriate far-field boundary conditions should be specified. Appropriate choices of the far-field boundary conditions have been a topic of interest in the literature including the report of Sani et al. (1994). To minimize the effect of these far-field boundary conditions on the accuracy, it is desirable to place the boundaries as far as possible from the cylinder. Moreover, as discussed in Chapter 2, numerically solving the Navier-Stokes equations by using fractional step methods requires the application of the Hodge/Helmholtz decomposition, but for problems with open-boundaries the Hodge/Helmholtz decomposition may not be unique. However, in the scope of assessing the simulation's performance of handling irregular rigid solid boundaries on Cartesian grids, the results of this test case can be compared with the other numerical computations in the literature, since the same difficulties apply to them as well.

In this work the following velocity boundary conditions are selected:

1. $u = U_o$ and $v = 0$ on the upstream-end of the domain,

2. $\frac{\partial \mathbf{u}}{\partial t}+c_e\frac{\partial \mathbf{u}}{\partial x}=\mathbf{0}$ on the downstream-end of the domain, where c_e is the space averaged horizontal velocity component u on a column of grid points that are one mesh space inside from the downstream-end, as suggested by Kim et al. (2001),
3. a. $\frac{\partial v}{\partial t}+c_n\frac{\partial v}{\partial y}=0$ for the convection terms on the top-side of the domain, where c_n is the space-averaged vertical velocity field v on a row of grid points that are one mesh space inside from the top-side,

   b. such a velocity field for the diffusion terms on the top-side that the fluid viscous stresses are continuous,
4. a. $\frac{\partial v}{\partial t}-c_s\frac{\partial v}{\partial y}=0$ for the convection terms on the bottom-side of the domain, where c_s is the space averaged vertical velocity field $-v$ on a row of grid points that are one mesh space inside from the bottom-side,

   b. such a velocity field for the diffusion terms on the bottom-side that the viscous stresses are continuous.

As for the boundary conditions for the pseudo-pressure variable $\tilde{p}$ (see Chapter 2 for its definition), $\nabla\tilde{p}\circ\mathbf{n}=0$ is used on all boundaries of the computational domain, where $\mathbf{n}$ is the outward normal vector of each boundary. As could be verified in Chapter 2's Eqn. (2.2-10), such a pseudo-pressure boundary condition is not necessarily compatible with the non-Dirichlet velocity boundary conditions. However, since this point has been overlooked in the similar studies of the literature and the only goal of conducting this study is to verify the simulation's capability of representing irregular solid boundaries on Cartesian grids through comparing the results with the other reported studies in the literature, no attempt was made to seek a more suitable pseudo-pressure boundary condition.

In reporting the results of the simulations the following outputs are used: i) drag coefficient C_D, lift coefficient C_L, and Strouhal number St. Their definitions together with the definition of the Reynolds number are as given below.

$$C_D = \frac{F_x}{\frac{1}{2}\rho {U_o}^2 d}, \quad C_L = \frac{F_y}{\frac{1}{2}\rho {U_o}^2 d}, \quad St = \frac{f}{U_o/d}, \quad Re = \frac{\rho U_o d}{\mu} \tag{4.3-9}$$

where F_x and F_y are respectively the horizontal and vertical forces applied on the fluid by the solid cylinder, while f is the time-frequency of the vortex-shedding. These forces are measured by drawing rectangular control volumes around the cylinder and using the integral form of the linear momentum part of the Navier-Stokes equation given in Eqn. (4.3-10) below with the previously computed velocity and pressure fields.

$$\int_V \rho \frac{\partial \mathbf{u}}{\partial t} dV + \int_A \rho\, \mathbf{u}(\mathbf{u} \circ \mathbf{n})\, dA = -\int_A p\mathbf{n} dA + \frac{1}{2}\int_A \mu \nabla \mathbf{u} \circ \mathbf{n} dA + \mathbf{F} \tag{4.3-10}$$

In Eqn. (4.3-10) A and V denotes the surface areas and volumes of the control-volumes and $\mathbf{n}$ is the unit outward vector from the surfaces of the control-volumes. To verify the consistency, the C_D, C_L, and St numbers were separately computed on three different control volumes in different sizes. Note that, the control volume for Eqn. (4.3-10) includes the volume inside the solid cylinder as well. However, since $\mathbf{u} = \mathbf{u}_{solid}$ is specified inside the solid cylinder via Eqn. (4.2-6) and it implies $\frac{\partial \mathbf{u}}{\partial t} = 0$, the inclusion of the solid cylinder in the control volume will not effect the measurement of the drag and lift forces through Eqn. (4.3-10).

4.3.2.1 Effect of the location of the far-field domain boundaries on the results

As discussed above, appropriate far-field boundary conditions are required for the numerical simulations of this problem. This test case attempts to assess the effect of the location of the far-field boundaries on the accuracy of the results. Tables 4.3-3 and 4.3-4 report the maximum C_L and time averaged C_D values with different domain sizes at $Re = 100$ and using $d/h \approx 34.2$ with using sharp ($\varepsilon = 0$) and smooth ($\varepsilon = 2h$) Heaviside functions, respectively. Note that, h is the uniform Eulerian mesh width.

Table 4.3-3: Effect of the location of the far-field domain boundaries on the results with $\varepsilon = 0$ at $Re = 100$ (See Fig. 4.3-2 for the definition of a)

a/d	$\bar{C}_D$	C_L
15	1.53	±0.38
30	1.39	±0.35
60	1.34	±0.33

Table 4.3-4: Effect of the location of the far-field domain boundaries on the results with $\varepsilon = 2h$ at $Re = 100$ (See Fig. 4.3-2 for the definition of a)

a/d	$\bar{C}_D$	C_L
15	1.63	±0.45
30	1.48	±0.40
60	1.41	±0.37

Tables 4.3-3 and 4.3-4 suggest a convergence trend in the results as the far-field boundaries are pulled away from the cylinder. As will be shown later, these *a/d* values are sufficient to compare the results with the other studies in the literature.

4.3.2.2 Effect of the grid resolution on the results

In this part, the effect of the grid resolution on the results is studied at $Re = 100$ and using $a/d = 30$. The converging results are given in Tables 4.3-5 and 4.3-6 below. Interestingly, the results with $\varepsilon = 0$ converge from lower C_D and C_L values to higher values, while the results with $\varepsilon = 2h$ converge from higher C_D and C_L values to lower values. Again, h is the uniform Eulerian mesh width.

Table 4.3-5: Effect of the grid resolution on the results with $\varepsilon = 0$ at $Re = 100$

Eulerian grid size	d/h	$\bar{C}_D$	C_L
513^2	17.1	1.33	±0.29
1025^2	34.2	1.39	±0.35
2049^2	68.3	1.40	±0.35

Table 4.3-6: Effect of the grid resolution on the results with $\varepsilon = 2h$ at *Re* = 100

Eulerian grid size	d/h	$\bar{C}_D$	C_L
513^2	17.1	1.59	±0.45
1025^2	34.2	1.48	±0.40
2049^2	68.3	1.43	±0.37

4.3.2.3 Effect of the time step on the results

To confirm the results above are insensitive to the time step value used in the simulations, one of the cases was computed again by using half of the original time step Δt^*. The results given below in Table 4.3-7 suggest that further reducing the previously used time step value does not change the results, at least using the same number of significant figures as in Sections 4.3.2.1 and 4.3.2.2.

Table 4.3-7: Effect of the time step on the results with *Re* = 100, *a/d* = 30, *d/h* = 34.2, and $\varepsilon = 0$

Time step	$\bar{C}_D$	C_L
Δt^*	1.39	±0.35
$\Delta t^*/2$	1.39	±0.35

4.3.2.4 Comparison with the other results in the literature

In Table 4.3-8 below, the present results are compared with the other results in the literature.

Table 4.3-8: Comparison of the present results with the others in the literature at *Re* = 100

	$\bar{C}_D$	C_L	*St*	Domain size
Present ($\varepsilon = 0$)	1.40	±0.35	0.166±0.0098	30*d* x 30*d*
Present ($\varepsilon = 0$)	1.34	±0.33	0.166±0.0098	60*d* x 60*d*
Present ($\varepsilon = 2h$)*	1.43	±0.37	0.166±0.0098	30*d* x 30*d*
Present ($\varepsilon = 2h$)*	1.41	±0.37	0.166±0.0098	60*d* x 60*d*
Williamson (1996)	—	—	0.163	experiment
Kim et al. (2001)	1.33	±0.32	0.165	70*d* x 100*d*
Silva et al. (2003)	1.39	—	0.16	30*d* x 15*d*
Tseng et al. (2003)	1.42	0.29 (rms)	0.164	32*d* x 16*d*
Le et al. (2006)	1.37	±0.323	0.160	30*d* x15*d*
Su et al. (2007)	1.40	±0.34	0.166	29.9*d* x 16.7*d*

* Note that, the results with $\varepsilon = 2h$ presented here were yet to converge with respect to the grid size (a grid size of 1025 x 1025 was used for a domain size of 60*d* x 60*d* and a grid size of 2049 x 2049 was used for a domain size of 30*d* x 30*d*), but the results presented here with $\varepsilon = 0$ are converged, as could be seen in Sections 4.3.2.1 and 4.3.2.2.

Table 4.3-8 suggests that the results with $\varepsilon = 0$ are within the range of the others. On the other hand by using the same grid resolutions with the results of $\varepsilon = 0$, the C_D and C_L values computed with $\varepsilon = 2h$ are rather higher than most of the other results in the literature, and also they were still not fully converged.

4.3.3 Simulating a cloth draped on a solid prism in 3D

In this verification study an initially flat, horizontal, and square cloth is released on top of a solid prism, whose top surface is also a square, and the cloth final draped shape on the prism is visually examined. The cloth mechanical model and the fluid/cloth interaction models are presented in Chapter 3, while the cloth/fluid mixture interaction with the solid prism is modeled by the method in Section 4.2 using a sharp Heaviside function ($\varepsilon = 0$). The cloth elastic parameters were selected to be consistent with those of the real clothes in their principal axes, but anisotropy effects are neglected. The physical and numerical parameters used in this problem are given in Table 4.3-9 below. Doing so, following the standard convention, the elastic constants of thin fabrics are reported as lower dimensional quantities. For instance, the cloth extensional stiffness (K_e) is proportional to cloth's Young's modulus times cloth thickness q (i.e. $\bar{E}q$). This study uses a two times finer Eulerian grid along the solid prism's height direction than its lateral directions.

Table 4.3-9: Physical and numerical parameters used in the simulations

Cloth extensional stiffness (K_e)	8×10^2 N/m
Cloth bending stiffness (K_b)	1×10^{-5} N.m
Cloth mass density	0.97 kg/m^2
Initial square dimension of the cloth	50 cm x 50 cm
Dimensions of the top square surface of the prism	25 cm x 25 cm
Fluid density (ρ_f)	0.01 kg/m^3
Fluid dynamic viscosity (μ)	1×10^{-5} kg/(m.s)
Dirac-delta function half width (ε_δ)	$2h_{lateral}$ or $2h_{height}$
Heaviside function half width (ε)	0
Minimum Lagrangian to Eulerian mesh size ratio	1.08
$h_{lateral} / h_{height}$	2

Even though, it is desirable to conduct this study without the fluid, due to the similar reason mentioned in Chapter 3, Section 3.5.1, small but nonzero values are used for the fluid density and viscosity values. Figure 4.3-3 below shows the result of this study with three different grid resolutions.

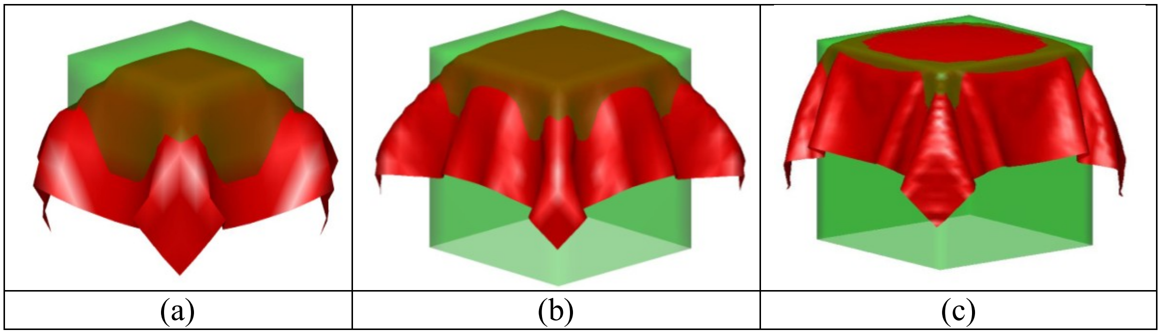

(a) (b) (c)

Figure 4.3-3: Effect of grid resolution on the shape of a draped cloth on a solid prism; a) 15^3 Eulerian/15^2 Lagrangian points, b) 33^3 Eulerian/30^2 Lagrangian points, and c) 65^3 Eulerian/60^2 Lagrangian points

Figure 4.3-3 clearly shows the improvement of the draped cloth shape with grid refinement as evidenced by the decreasing penetration into the solid prism with refinement. The reason for the cloth penetration into the rigid solid could be explained as follows. As discussed in Chapter 3, Section 3.2, in the context of the Immersed Boundary method, cloth inherits its velocity field from the Eulerian grid points by using a weighted-averaging via the discrete form of Eqn. (3.2-13) as it deforms into its static equilibrium position under its own weight from an initially horizontal and flat configuration. However, since the neighboring Eulerian grid points close to the rigid solid may have velocities pointing into the solid prism and the Eulerian grid points in the solid have zero velocities (by definition), the cloth may also inherit a velocity that points into the solid causing it to penetrate. This is also the reason why the penetration is more severe near the corners and edges; the corners and edges are exposed to more neighboring Eulerian grid points with nonzero velocities than the other faces of the prism. Naturally, such a penetration will scale by the Eulerian grid resolution. Specifically, in this study the maximum penetration was estimated to be approximately $0.3h$.

CHAPTER V
NUMERICAL SIMULATIONS OF WASHING MACHINE PROCESSES

5.1 Introduction

This chapter presents washing machine simulations with multiple cloth pieces. The previous chapters on the numerical solution of the Navier-Stokes equations (Chapter 2), modeling the fluid/structure interaction and cloth mechanics (Chapter 3), and representing complex geometries on Cartesian grids (Chapter 4) serve as the foundation for this application study as well as an aid to verify the simulations under simplistic conditions. Since it is nontrivial to conduct a washing machine experiment to assess the accuracies of the results (due to difficulties in controlling the initial conditions and visualization) and this research timeline lacked the dedicated time to perform such experiments, only numerical results will be given in this chapter. On the other hand, based on the previous simple verification studies it may now be possible to expect the washing machine simulations to model the washing processes provided that the individual fluid and cloth models are appropriate and the massive required computational resources are available.

Actual washing machine processes involve mechanical agitation of many cloths with different mechanical properties in various different geometries (e.g. trousers, shirts, bed sheets, etc.) in a detergent/water mixture. The wash-fluid does not fill the whole washtub, so the washtub includes a dynamically evolving wash-fluid/air interface. In general, there are two types of washing machines: vertical and horizontal-axis washing machines. The vertical-axis washing machines use a mechanical agitator to drive the wash-fluid/cloth mixture, where on the other hand the horizontal-axis washing machines drive the fluid/cloth mixture by basket rotation and gravity.

The present simulation capabilities are as follows. The simulation uses an elastic, and nonporous thin cloth model with an incompressible, viscous, and Newtonian fluid model. The cloth elastic model includes extensional, in-plane shear, bending, and torsional stiffness. Cloth deformation can be large, but cloth strains are assumed to stay small. Detailed information on the cloth elastic model is given in Chapter 3. The simulation solves the coupled dynamical equations of the fluid and the cloth pieces on a fixed structured Cartesian grid and uses moving Lagrangian points to trace the cloth pieces as explained in Chapter 3. Due to the nature of the fluid/cloth modeling technique used in the simulation, the cloth inherits the same local velocity field of the fluid, so unphysical inter-penetration between two different cloth pieces as well as any self-penetration within a single cloth piece can be avoided with well-resolved simulations. However, as will be discussed later, the nature of the fluid/cloth modeling technique makes the cloth pieces artificially ‘sticky’ for the poorly resolved simulations. As for the wash-fluid/air interface, the simplified simulation presented here uses a fixed, impenetrable slip-free surface. Hence, this research only studies vertical-axis washing machines. Doing so, a mechanical agitator, presently used by the Whirlpool Corporation in some of their modern washing machines, is incorporated into the simulations using the technique described in Chapter 4.

For actual washing machine processes the Reynolds number (Re) based on the washing machine agitator radius, maximum agitator speed, and single phase water properties is in the order of 10^5. For turbulent flows, the ratio of the largest eddy scale to the smallest flow scale where energy is dissipated is proportional to $Re^{3/4}$ as explained in Pope (2000). Assuming the largest eddy size in a washtub is the washtub diameter, this result suggests that fully capturing the flow details (without cloth) requires an approximate grid size of 10^4 x 10^4 x 10^4 points. As a practical alternative to the direct numerical simulations, ‘shortcut’ turbulence models simulate large Re flows such as the Large Eddy Simulation (LES) methods and Reynolds Averaged Navier-Stokes (RANS) approaches. Unfortunately, their performances are problem-dependent and their development is an active topic of research. The present simulation is not equipped with any turbulence models and due to the computational constraints mentioned above it is unlikely to give accurate results at the parameter range of the realistic washing machine processes. However, the present simulation may simulate lower *Re* washing machine processes and even these simulations may be able to provide ideas to washing machine designers, while anticipating upgrades to the simulation and the computational hardware that it runs on. Also note that, the Reynolds number based on the tight inter-cloth spacing might be much lower than the previous estimate based on the washing machine agitator radius, supporting the values of the coarse grid simulations.

A second way to evaluate grid requirements is to consider the direct numerical simulations with imbedded cloth pieces. A fully resolved computation requires a fine scale grid spacing on the order of the cloth separation spacing. This is almost certainly approaching molecular distances, especially when permeable cloth is considered that can allow cloth surfaces to merge more easily. This is further complicated by our computational technique that distributes the cloth effect of several grid points. Obviously, this is well beyond any computation resources for some time to come.

This chapter is organized as follows. First, different measures to characterize the simulation outputs will be given. This will be followed by the presentation of the two- and three-dimensional simulations.

5.2 Characterization of outputs

The most important output one may get from a washing machine simulation is the typical motion of the cloth pieces. To describe the cloth motion for a given washing machine operating condition, this study uses: the trajectories of cloth pieces' center of mass positions, the average tumbling rate of the cloth pieces (i.e. how often does a specially-colored cloth piece rise and then sink), and visual observations on the average distance between cloth pieces to describe whether or not if they get clustered or remain well-dispersed.

As mentioned in Chapter 3, cloth pieces are described in a Lagrangian manner, i.e. all the deformations are measured with respect to a reference configuration. For convenience, this reference configuration is selected as a flat and stress-free state. As described there, at this reference configuration the cloth is parameterized by two orthogonal and straight constant *s* and *r* lines as shown below in Fig. 5.2-1. By measuring and reporting the statistics of their dynamically changing arclengths, normal curvatures, and their intersecting angles, it is possible to build insightful global deformation measures for each cloth.

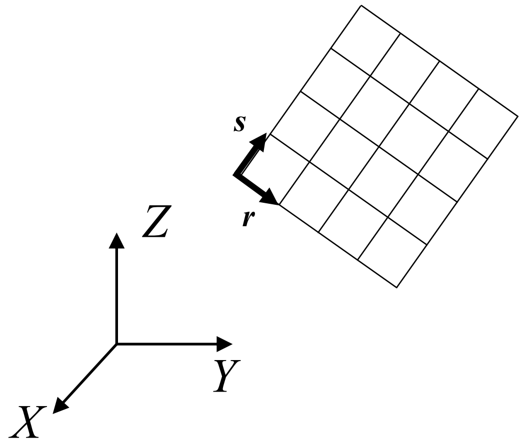

Figure 5.2-1: Constant *r* and *s* lines on a cloth piece at its undeformed reference state

It may also be of interest to report loading statistics of the cloth pieces. As derived in Chapter 3, Section 3.3.3, the Eulerian strains are given as

$$\begin{aligned}
e_{ss} &= \frac{1}{2}\left(1 - 1\Big/\left|\frac{\partial \mathbf{X}}{\partial s}\right|^2\right) - z\kappa_s \\
e_{rr} &= \frac{1}{2}\left(1 - 1\Big/\left|\frac{\partial \mathbf{X}}{\partial r}\right|^2\right) - z\kappa_r \\
e_{sr} &= \frac{1}{2}\left(\frac{\partial \mathbf{X}}{\partial s} \circ \frac{\partial \mathbf{X}}{\partial r}\right)\Big/\left|\frac{\partial \mathbf{X}}{\partial s}\right|\left|\frac{\partial \mathbf{X}}{\partial r}\right| - z\left\{\left(\frac{\partial^2 \mathbf{X}}{\partial r \partial s} \circ \mathbf{e_3}\right)\Big/\left|\frac{\partial \mathbf{X}}{\partial s}\right|\left|\frac{\partial \mathbf{X}}{\partial r}\right|\right\}
\end{aligned} \qquad \textbf{(5.2-1)}$$

where **X** denotes the coordinates of a point on cloth, κ_s and κ_r are respectively the normal curvatures of the constant r and s lines, and z is a local cloth coordinate along thickness direction, which is zero at cloth's mid-plane. The form of Eqn. (5.2-1) suggests that the maximum strains will occur at either $z = \pm q/2$, where q is the cloth thickness. So the absolute largest strains could be predicted as

$$\begin{aligned}
\left|e_{ss}\right|_{\max} &= \left|\frac{1}{2}\left(1 - 1\Big/\left|\frac{\partial \mathbf{X}}{\partial s}\right|^2\right)\right| + \left|\frac{q}{2}\kappa_s\right| \\
\left|e_{rr}\right|_{\max} &= \left|\frac{1}{2}\left(1 - 1\Big/\left|\frac{\partial \mathbf{X}}{\partial r}\right|^2\right)\right| + \left|\frac{q}{2}\kappa_r\right| \qquad \textbf{(5.2-2)} \\
\left|e_{sr}\right|_{\max} &= \left|\frac{1}{2}\left(\frac{\partial \mathbf{X}}{\partial s} \circ \frac{\partial \mathbf{X}}{\partial r}\right)\Big/\left|\frac{\partial \mathbf{X}}{\partial s}\right|\left|\frac{\partial \mathbf{X}}{\partial r}\right|\right| + \left|\frac{q}{2}\left\{\left(\frac{\partial^2 \mathbf{X}}{\partial r \partial s} \circ \mathbf{e_3}\right)\Big/\left|\frac{\partial \mathbf{X}}{\partial s}\right|\left|\frac{\partial \mathbf{X}}{\partial r}\right|\right\}\right|
\end{aligned}$$

Note that, there is a slight theoretical complication for estimating the absolute maximum cloth stresses using the strains given in Eqn. (5.2-2): the absolute maximum strains $\left|e_{ss}\right|_{\max}$ or $\left|e_{rr}\right|_{\max}$ may not occur at the same point ($z = q/2$ or $z = -q/2$) if κ_s and κ_r has different signs. However, for a cloth with relatively high membrane stiffness, the deformed geometry will always be developable, assuring the Gaussian curvature (the product of κ_s and κ_r) to be always zero and avoiding this situation (Ventsel et al. (2001)). So one might use the following relation to estimate the absolute maximum cloth stresses

$$\begin{pmatrix} \left|\sigma_{ss}\right|_{max} \\ \left|\sigma_{rr}\right|_{max} \\ \left|\sigma_{sr}\right|_{max} \end{pmatrix} = \frac{\bar{E}}{1-\nu^2} \begin{pmatrix} 1 & \nu & 0 \\ \nu & 1 & 0 \\ 0 & 0 & 1-\nu \end{pmatrix} \begin{pmatrix} \left|e_{ss}\right|_{max} \\ \left|e_{rr}\right|_{max} \\ \left|e_{sr}\right|_{max} \end{pmatrix} \qquad \textbf{(5.2-3)}$$

where $\bar{E}$ is the cloth Young's modulus and ν is the cloth Poisson's ratio. For a one-dimensional fiber this relation reduces to

$$\left|\sigma_{ss}\right|_{max} = \bar{E}\left|e_{ss}\right|_{max} \tag{5.2-4}$$

For estimating cloth stresses, we define stiffness constants associated with each different type of deformation. Specifically, we define

$$K_e \equiv \frac{\bar{E}q}{1-\nu^2}, \quad K_s \equiv \frac{\bar{E}q}{1+\nu}, \quad K_b \equiv \frac{\bar{E}q^3}{12\left(1-\nu^2\right)}, \quad K_t \equiv \frac{\bar{E}q^3}{12\left(1+\nu\right)}$$

which are respectively the cloth extensional, in-plane shear, bending, and torsion stiffness. For each of them, we use representative values similar to the reported constants in the textile journals.

In some of the simulation results of this chapter, the statistics of the absolute maximum cloth stresses will be discussed. Doing so, these statistics are taken for all the cloth pieces' all discrete points as in

$$\overline{\left|\sigma_{ij}\right|_{max}} = \frac{1}{N_{cloth}} \sum_{k=1}^{N_{cloth}} \frac{1}{A_k} \int_{A_k} \overline{\left|\sigma_{ij}\right|_{max}^{k}} dA_k \tag{5.2-5}$$

where N_{cloth} is the total number of cloth pieces, A is each cloth's surface area, and $\overline{\left|\sigma_{ij}\right|_{max}^{k}}$ is the time average of the absolute maximum cloth stress σ_{ij}.

5.3 Estimating the cloth's average thickness q and excess mass density ρ_s

To estimate the cloth average thickness q and excess mass density ρ_s with respect to the fluid we conducted a simple measurement as explained below:

1. Fill a test tube with water and record the water volume.

2. After recording their total dry mass and surface area, immerse several small cloth pieces into this test tube, stir the mixture to let any trapped air to escape, and then note the new steady water level in the tube to calculate the displaced water volume.

3. Use this displaced water volume, to estimate the mass of the displaced water.

4. Divide the displaced water volume by the total cloth surface area to find the 'average' cloth thickness q.

5. Divide the difference between the total dry mass of the cloth pieces and the mass of the displaced water to the total surface area of cloth pieces and estimate the cloth excess mass density ρ_f.

Specifically, for a sample polyester cloth in water within two digits of accuracy we measured:

$$\rho_s = 9.3x10^{-2} \quad \left[\mathrm{kg/m^2}\right] \tag{5.3-1}$$

$$q = 2.4x10^{-4} \quad [\mathrm{m}] \tag{5.3-2}$$

5.4 Two-dimensional simulations

This study on the two-dimensional washing machine simulations is intended to be only illustrative, because two-dimensional simulations cannot capture the vertical tumbling motion of the cloth pieces in a vertical-axis washing machine, recognized to be highly correlated with effectiveness of the washing processes[2]. However, compared to the three-dimensional simulations these simulations can cheaply verify some aspects of the simulation development.

---

[2] Private communication - Whirlpool Corporation's technical personnel

5.4.1 Washtub and the initial cloth placements

The numerical setup of the two-dimensional simulations is as given in Fig. 5.4-1 below. The washtub consists of an outer nonmoving cylinder and a rotating agitator. This geometry is represented on a Cartesian grid using the method given in Chapter 4. Figure 5.4-2 shows the initial placement of twenty cloth pieces, whose lengths are either 25.92 cm or 17.28 cm. In all two-dimensional simulations shown here, the geometry of the washtub and the initial cloth placements are same.

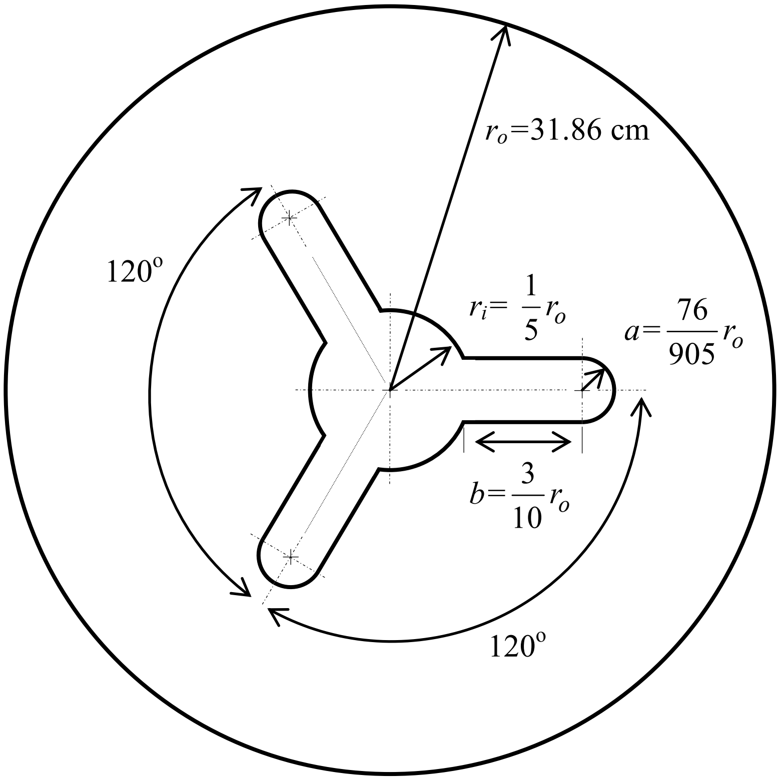

Figure 5.4-1: The washtub geometry used for the two-dimensional simulations

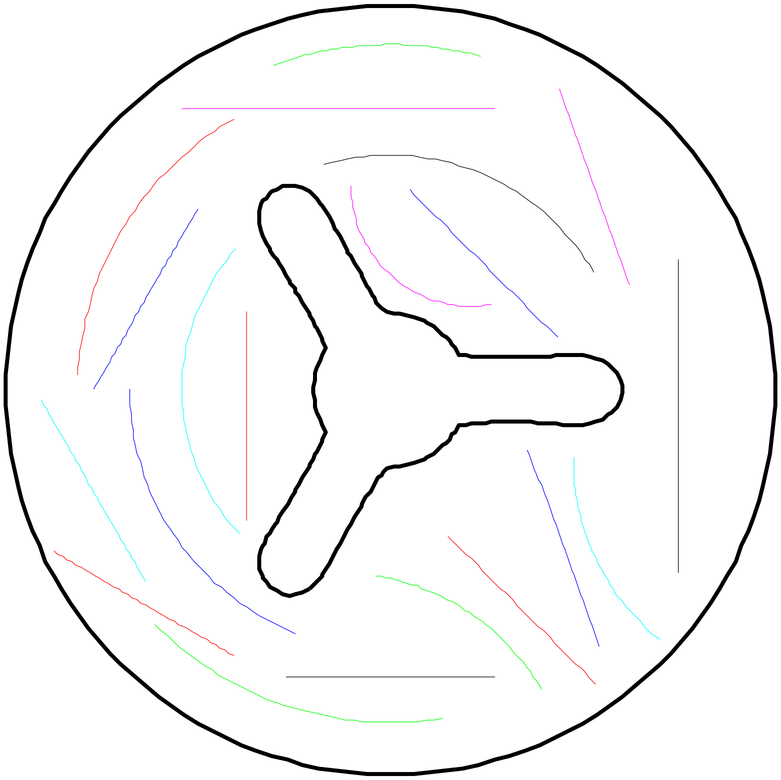

Figure 5.4-2: The initial placements of twenty cloth pieces inside the washtub, whose lengths are either 25.92 cm or 17.28 cm

5.4.2 Operating conditions, physical properties and numerical parameters used in the simulations

Unless noted elsewhere the operating conditions[3], physical and numerical properties given in Table 5.4-1 are used in the simulations. The elastic constants of thin fabrics are reported as lower dimensional quantities following the standard convention. For instance, the cloth extensional stiffness (K_e) is proportional to cloth's Young's modulus times thickness q (i.e. $\bar{E}q$). As mentioned in Chapter 3, Section 3.4.1, the simulation uses the implicit Broyden's method to numerically solve Eqn. (3.2-14).

---

[3] The operating conditions of the agitator are as suggested by the Whirlpool Corporation.

Table 5.4-1: Operating conditions, physical and numerical parameters used in the simulations

Peak impeller rotation speed of the agitator (ω_{max})	120 rpm
Number of agitator revolutions in each direction before reversing	1
Cloth extensional stiffness (K_e)	8×10^3 N/m
Cloth bending stiffness (K_b)	1×10^{-5} N.m
Cloth excess mass density (ρ_s) (with respect to water)	9.3×10^{-2} kg/m^2
Length of the cloth pieces	25.92 or 17.28 cm
Average cloth thickness (q)	2.4×10^{-4} m
Water density (ρ_f)	1×10^3 kg/m^3
Water dynamic viscosity (μ)	1×10^{-3} kg/(m.s)
Number of cloth pieces	20
Dirac-delta function half width (ε_δ)	$2h$
Heaviside function half width (ε)	0
Average Lagrangian to Eulerian mesh size ratio	1

The Lagrangian mesh size mentioned in Table 5.4-1 is measured on the unstreched cloth. With a simple calculation, the operating conditions of the agitator given in Table 5.4-1 can be implied by the following form of angular velocity

$$\omega = \omega_{max} \, sin\left(2\pi f\, t\right) \quad \textbf{(5.4-1)}$$

with

$$\omega_{max} = 4\pi \quad \left[\text{rad/s}\right] \quad \textbf{(5.4-2)}$$

$$f = \frac{\pi}{2} \quad \left[1/\text{s}\right] \quad \textbf{(5.4-3)}$$

where ω is the angular velocity of the agitator, f is the frequency of agitator's rotation cycle, and t is time. In Eqn. (5.4-1) ω and t respectively have the units of rad/s and s, if using Eqns. (5.4-2) and (5.4-3).

5.4.3 Dimensionless groups

To describe the physics of the two-dimensional washing machine processes the following length, time and mass scales are selected:

$$l^o = r_o, \quad t^o = 1/\omega_{max}, \quad M^o = \rho_f r_o^{\,3} \tag{5.4-4}$$

Note that, especially for such a complex geometry these choices are non-unique. Using these basic scales, the following velocity and pressure scales are defined

$$u^o = \omega_{max} r_o, \quad p^o = \rho_f \omega_{max}^{\;\;2} r_o^{\,2} \tag{5.4-5}$$

As a reminder, the mathematical model presented in Chapter 3, Section 3.2 assumes the solids are infinitesimally thin and uses Dirac-delta functions δ to formulate the fluid/structure interaction. The units of these Dirac-delta functions are inverse length, but an appropriate choice to non-dimensionalize this length is unclear. To work around this difficulty, we step back from assuming cloth pieces to be infinitesimally thin and use the average cloth thickness q to scale δ, whose measurement is described in Section 5.3. So in this development, the desingularized cloth quantities (Chapter 3, Eqn. 3.2-12) will be scaled by inverse q.

Using these characteristic scales, the dimensionless equations are given below. For sake of clearness, all the non-dimensional variables are kept in their previous dimensional notations. In the equations below $\mathbf{x} = (x, y)$ is a non-moving point in space, $\mathbf{X} = (X, Y)$ is a material point moving with a cloth piece, s is the cloth's unstreched arclength parameter, and p is the fluid pressure.

$$\frac{\partial \mathbf{u}}{\partial t} + \mathbf{u} \circ \nabla \mathbf{u} = -\nabla p + \frac{1}{\mathbf{Re}} \nabla^2 \mathbf{u} + \mathbf{f} \tag{5.4-6}$$

$$\nabla \circ \mathbf{u} = 0 \tag{5.4-7}$$

$$\mathbf{f}(\mathbf{x},t)=\int\left(\mathbf{F}(s,t)-\mathbf{In}\frac{D\mathbf{U}(s,t)}{Dt}\right)\delta\big(x-X(s,t)\big)\delta\big(y-Y(s,t)\big)\,ds \tag{5.4-8}$$

$$\mathbf{U}(s,t)=\int\mathbf{u}(\mathbf{x},t)\,\delta\big(x-X(s,t)\big)\delta\big(y-Y(s,t)\big)\,dx\,dy \tag{5.4-9}$$

$$\frac{D\mathbf{X}(s,t)}{Dt}=\mathbf{U}(s,t) \tag{5.4-10}$$

$$\mathbf{F}(s,t)=\mathbf{F_e}(s,t)+\mathbf{F_b}(s,t) \tag{5.4-11}$$

$$\mathbf{F_e}=\frac{\partial}{\partial s}\left(\frac{1}{2}\mathbf{Te}\left(\frac{\partial\mathbf{X}}{\partial s}\circ\frac{\partial\mathbf{X}}{\partial s}-1\right)\frac{\partial\mathbf{X}}{\partial s}\right) \tag{5.4-12}$$

$$\mathbf{F_b}=-\frac{\partial}{\partial s}\left(\frac{1}{\left|\partial\mathbf{X}/\partial s\right|}\mathbf{e_3}\frac{\partial}{\partial s}\left(\mathbf{Be}\;\kappa_s\right)\right) \tag{5.4-13}$$

$$\kappa_s=\left(\frac{\partial\mathbf{e_1}}{\partial s}\circ\mathbf{e_3}\right)\Big/\left|\frac{\partial\mathbf{X}}{\partial s}\right|,\quad \mathbf{e}_1=\frac{\partial\mathbf{X}}{\partial s}\Big/\left|\frac{\partial\mathbf{X}}{\partial s}\right|,\quad \mathbf{e}_3=\mathbf{e_1}\times(0,0,1) \tag{5.4-14}$$

$$\omega=sin\left(\mathbf{St}\,2\pi t\right) \tag{5.4-15}$$

where

$$Re=\frac{\rho_f {r_o}^2\omega_{max}}{\mu} \tag{5.4-16}$$

$$Te=\frac{K_e}{\rho_f\left(\omega_{max}r_o\right)^2 q} \tag{5.4-17}$$

$$Be = \frac{K_b}{\rho_f \omega_{max}^2 r_o^4 q} \tag{5.4-18}$$

$$In = \frac{\rho_s}{\rho_f q} \tag{5.4-19}$$

$$St = \frac{f}{\omega_{max}} \tag{5.4-20}$$

with a predefined washtub geometry. The dimensional values given in Section 5.4.1 and 5.4.2 correspond to the dimensionless values given in Table 5.4-2, which are used in the simulations unless noted elsewhere.

Table 5.4-2: Dimensionless groups used in the simulations unless reported elsewhere

Re	1.3 x 10^6
Te	2.1 x 10^3
Be	2.6 x 10^{-5}
In	0.3875
St	0.125

5.4.4 Results

5.4.4.1 Effect of changing the Eulerian mesh size *h*

Aref (1984) argues that the advection of particles even within laminar flows is chaotic as long as the velocity field is unsteady. Chaotic systems have different resulting details with slightly different initial conditions. However, their statistics can be well-defined. Since finite-difference approximations of the differential equations give truncation errors proportional to the time-step and mesh-width, the effect of lowering time-step or mesh-width may be enough to trigger a slight difference to yield a totally different result as explained by Teixeira et al. (2007). As expected, the present washing machine simulations gave different cloth locations with a successive lowering of the time-step and mesh-size.

Keeping a constant Lagrangian to Eulerian mesh width ratio, Table 5.4-3 shows the effect of changing the uniform Eulerian mesh size h on the statistics of the absolute cloth stresses of all the discrete points of all the cloth pieces (as defined in Section 5.2) with $Re = 1.3 \times 10^3$ and $\Delta t = 9.45 \times 10^{-5}$. The statistics are given up to the first 1.5 agitator rotation cycles, due to the limited data available at the finest grid resolution. On the electronic pdf version of this document, click **here** to view the cloth motion with $h/2r_o = 4.2 \times 10^{-3}$ as an embedded movie file.

Table 5.4-3: Effect of changing the Eulerian mesh size on the statistics of the absolute cloth stresses up to the first 1.5 agitator rotation cycles with $Re = 1.3 \times 10^3$ and $\Delta t = 9.45 \times 10^{-5}$

$h/2r_o$	Average absolute cloth stress [MPa]	Standard deviation [MPa]
3.39×10^{-2}	1.492	0.511
1.70×10^{-2}	0.386	0.171
8.5×10^{-3}	0.135	0.034
4.2×10^{-3}	0.087	0.017

Table 5.4-3 shows that the average cloth stresses decrease with refining the resolution, while converging to a finite value. This might be due to the more accurate capture of the complex shapes of the cloth pieces by increasing the grid resolution, in turn decreasing the effect of the unresolved wrinkles on the cloth bending stresses.

Using the same grid sizes as that used here, one might expect to have larger errors in the average cloth stresses at higher Re numbers, because of the more complex fluid mixing. The reason for conducting this study in such a low Re is the robustness of the simulations. At high Re the deformed cloth shapes get very complex, challenging the robustness of the simulation without using small time steps or without allowing more numerical iterations (see Chapter 2, Sections 2.2.5, 2.2.6 and Chapter 3, Section 3.4.1 for the use of numerical iterations in the simulation).

5.4.4.2 Effect of changing the time step Δt

Table 5.4-4 shows the effect of changing the time step on the statistics of the absolute cloth stresses up to the first 1.5 agitation cycles with $Re = 1.3 \times 10^3$, defining $\Delta t^* = 1.885 \times 10^{-4}$, and using $h/2r_o = 8.5 \times 10^{-3}$, where h is the uniform Eulerian mesh-width.

Table 5.4-4: Effect of changing the time step on the statistics of the absolute cloth stresses with $Re = 1.3 \times 10^3$, $h/2r_o = 8.5 \times 10^{-3}$, and defining $\Delta t^* = 1.885 \times 10^{-4}$

Time step	Average absolute cloth stress [MPa]	Standard deviation [MPa]
Δt^*	0.137	0.042
$\Delta t^*/2$	0.135	0.034
$\Delta t^*/4$	0.147	0.048

As can be seen in Table 5.4-4, within two digits of accuracy, the results were not very sensitive to changing the time step, at least for the time step values used here. Note that, the errors due to the spatial grid resolution might be big enough to mask the sensitivity of the results to time step.

5.4.4.3 Effect of using a sharp vs. a smooth Heaviside function

In this part, the effect of using a sharp ($\varepsilon = 0$) versus a smooth ($\varepsilon = 2h$) Heaviside function is examined by using $Re = 1.3 \times 10^3$, $h/2r_o = 8.5 \times 10^{-3}$, and $\Delta t = 1.885 \times 10^{-4}$. As a reminder, the simulation uses Heaviside functions to represent the agitator and the outer drum on a Cartesian Eulerian grid as explained in Chapter 4. The sharp Heaviside function appeared to provide better results in the verification studies of Chapter 4. On the electronic pdf version of this document, click **here** to view the cloth motion using a sharp and click **here** to view the motion using a smooth Heaviside function as an embedded movie file. In particular, note that the cloth pieces come very close to the agitator if using a sharp Heaviside function. Figure 5.4-3 illustrates regularly taken snapshots from these two different cases, where the snapshots in the left column are for a sharp and the snapshots in the right column are for a smooth Heaviside function. The time duration between each snapshot is approximately a quarter period of the agitator rotation cycle, which means the agitator rotates 180° between each snapshot. The sequence could be followed by the sequence number at the right bottom corner of each snapshot.

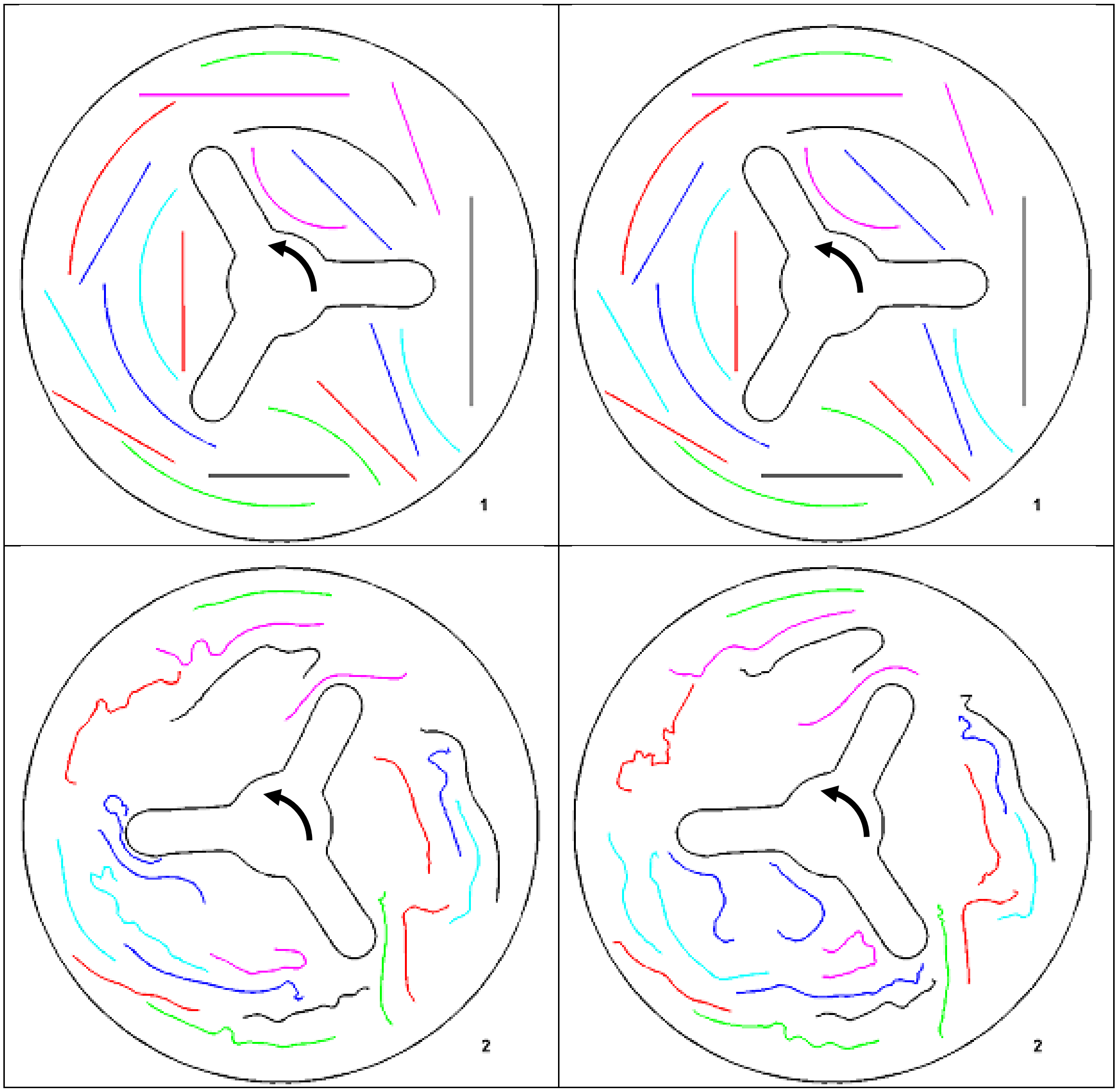

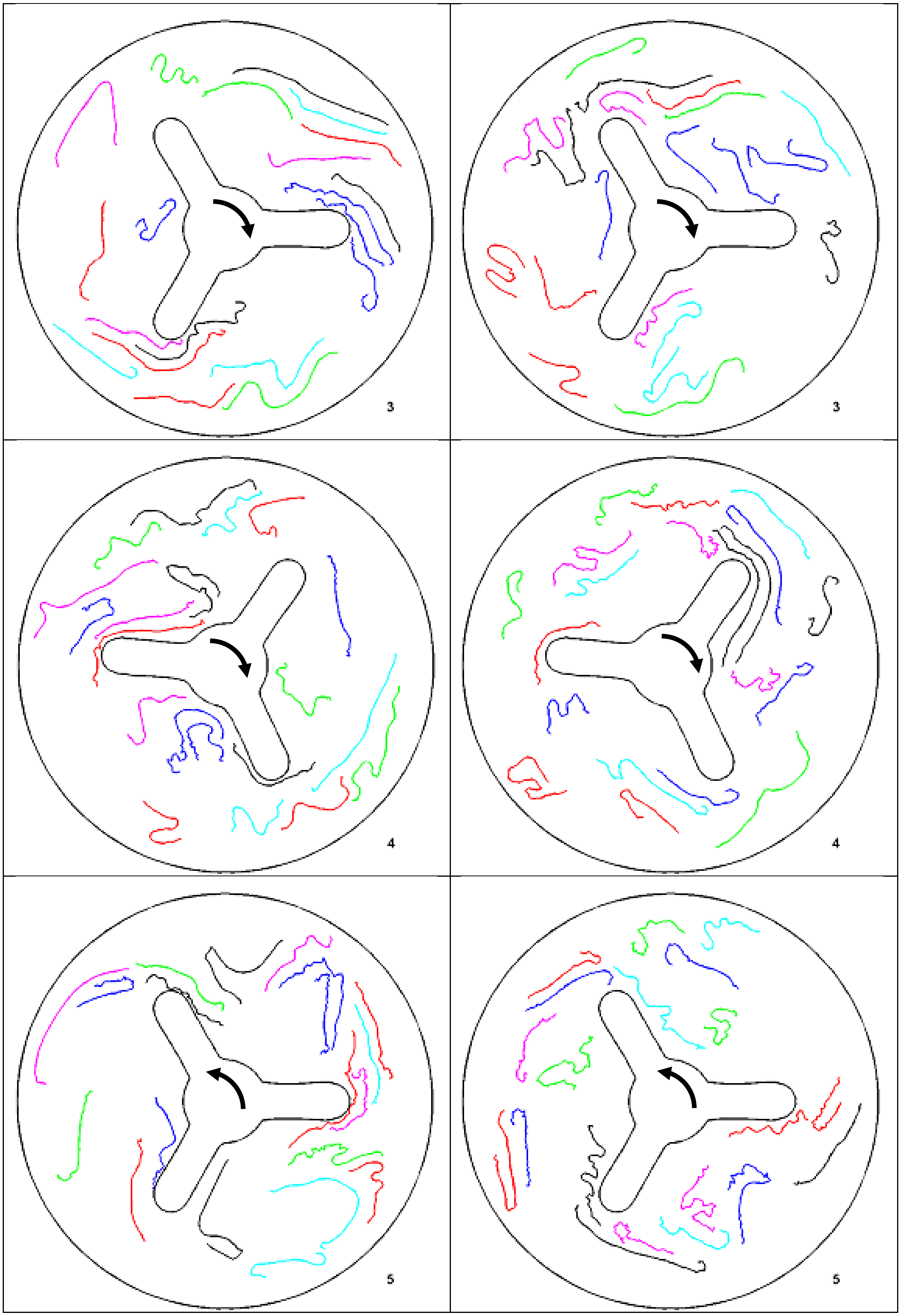
3
3
4
4
5
5

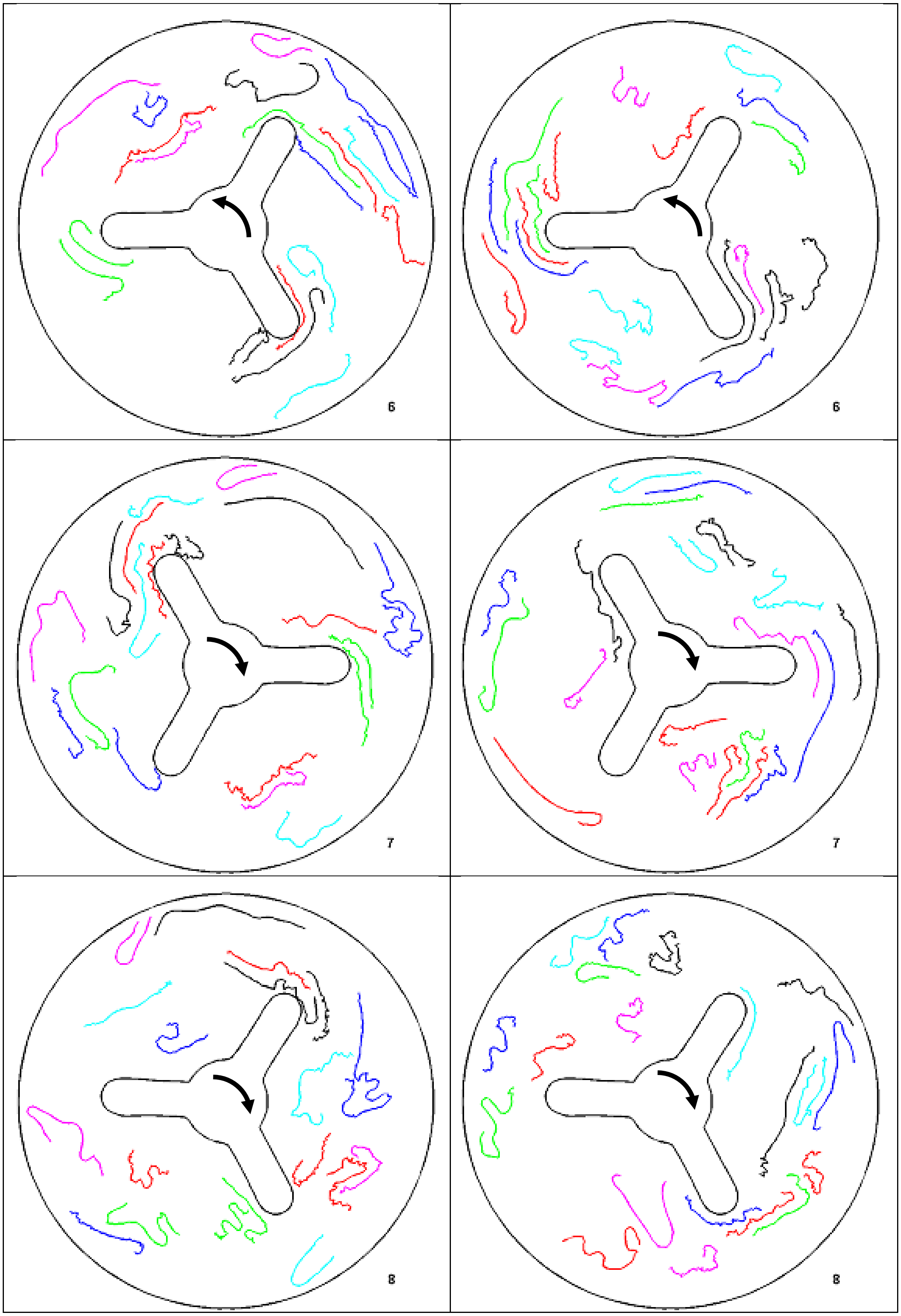
6
6
7
7
8
8

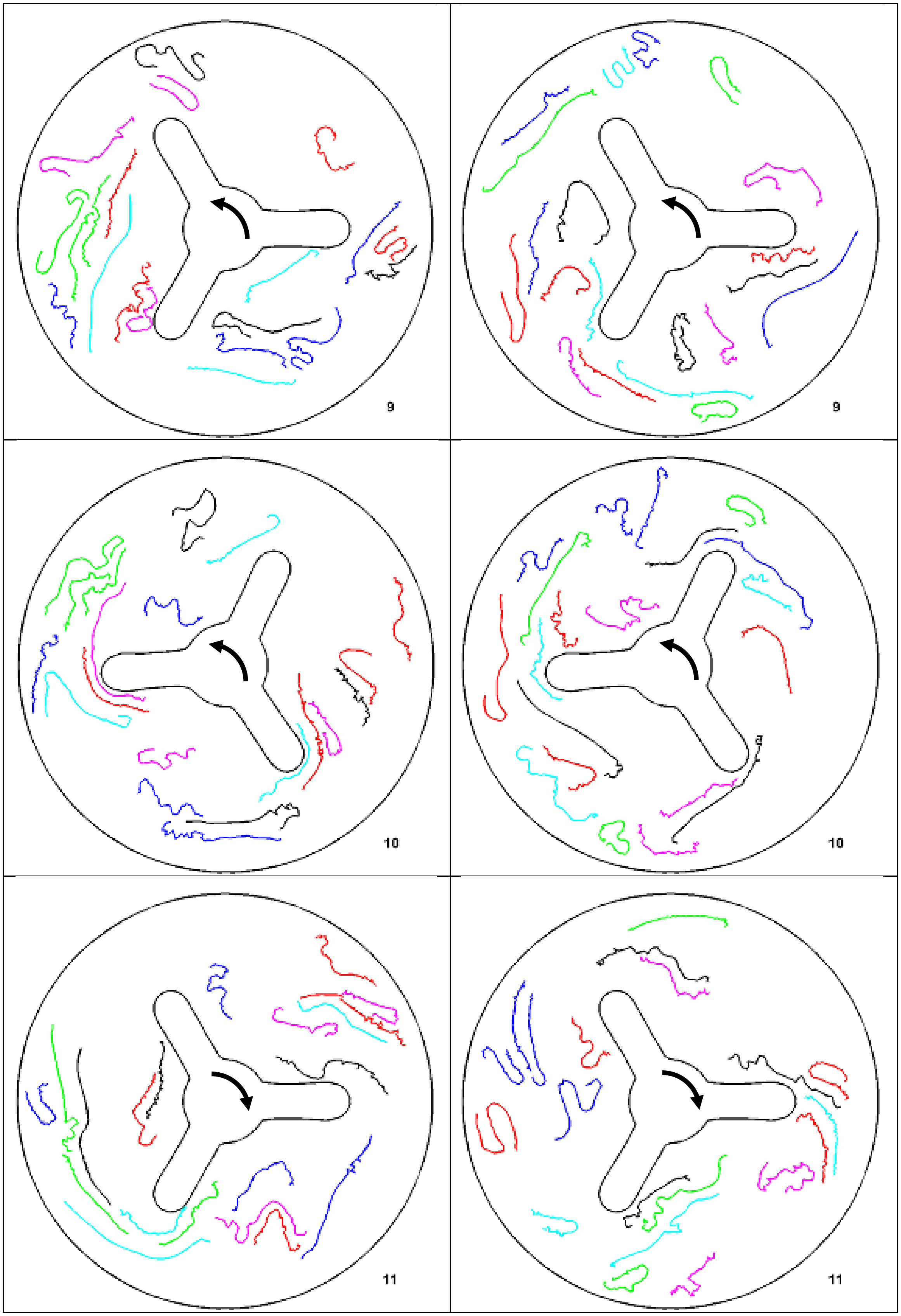
9
9
10
10
11
11

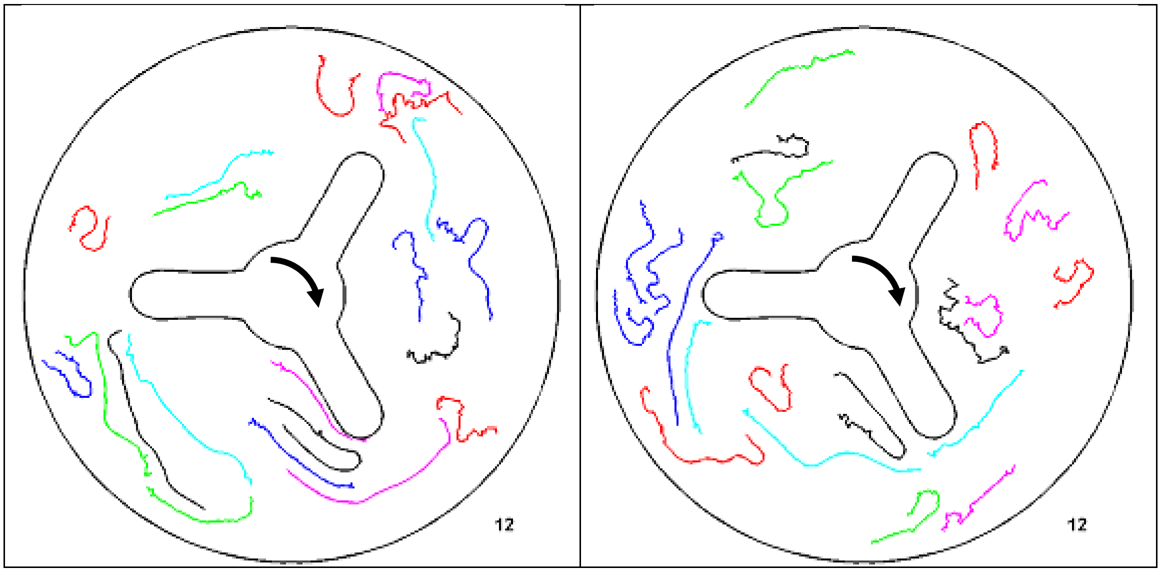

Figure 5.4-3: Effect of using a sharp ($\varepsilon = 0$) and a smooth ($\varepsilon = 2h$) Heaviside function on cloth motion with $Re = 1.3 \times 10^3$, $h/2r_o = 8.5 \times 10^{-3}$ and $\Delta t = 1.885 \times 10^{-4}$. The snapshots in the left column are for a sharp ($\varepsilon = 0$) and the snapshots in the right column are for a smooth ($\varepsilon = 2h$) Heaviside function. Snapshots differ by a quarter period of the agitator cycle corresponding to 180° rotation

The snapshots in Fig. 5.4-3 illustrate that using a smooth ($\varepsilon = 2h$) Heaviside function, cloth pieces do not come as close to the tip of the agitator as in the case of using a sharp ($\varepsilon = 0$) Heaviside function, where they sometimes accidentally slightly penetrate into the agitator. The reason why cloth pieces can escape from the agitator after a slight penetration is due to the numerical form of Eqn. (5.4-9), which is a weighted averaging to estimate the velocities of the cloth pieces from the velocities of the Eulerian grid points.

5.4.4.4 Effect of changing the cloth bending stiffness

In this study, the effect of changing cloth bending stiffness on the motion of the solids is examined with $Re = 1.3 \times 10^3$, $h/2r_o = 8.5 \times 10^{-3}$ and $\Delta t = 1.885 \times 10^{-4}$. On the electronic pdf version of this document, click **here** to view the cloth motion with $Be = 2.6 \times 10^{-2}$ and click **here** to view the motion with $Be = 2.6 \times 10^{-5}$ as an embedded movie file. In particular, note the relative smoothness of the solid shapes with higher Be. The left column of Fig. 5.4-4 illustrates the shapes of the solid fibers in the washtub with $Be = 2.6 \times 10^{-2}$, which can be compared to the snapshots in the right column with $Be = 2.6 \times 10^{-5}$. Again, the time duration between each snapshot is approximately a quarter period of the agitator rotation cycle, so the agitator rotates 180° between each snapshot.

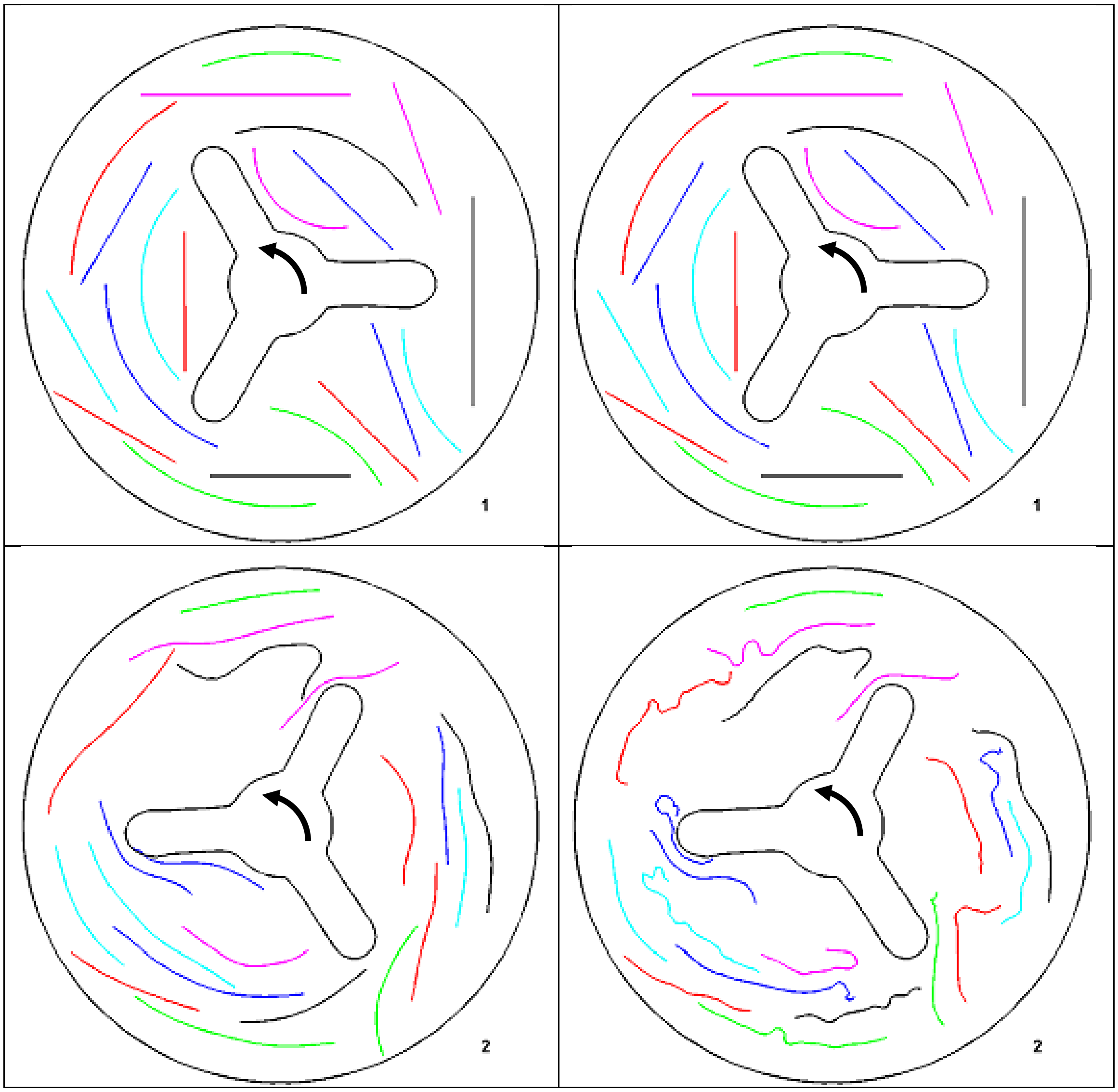

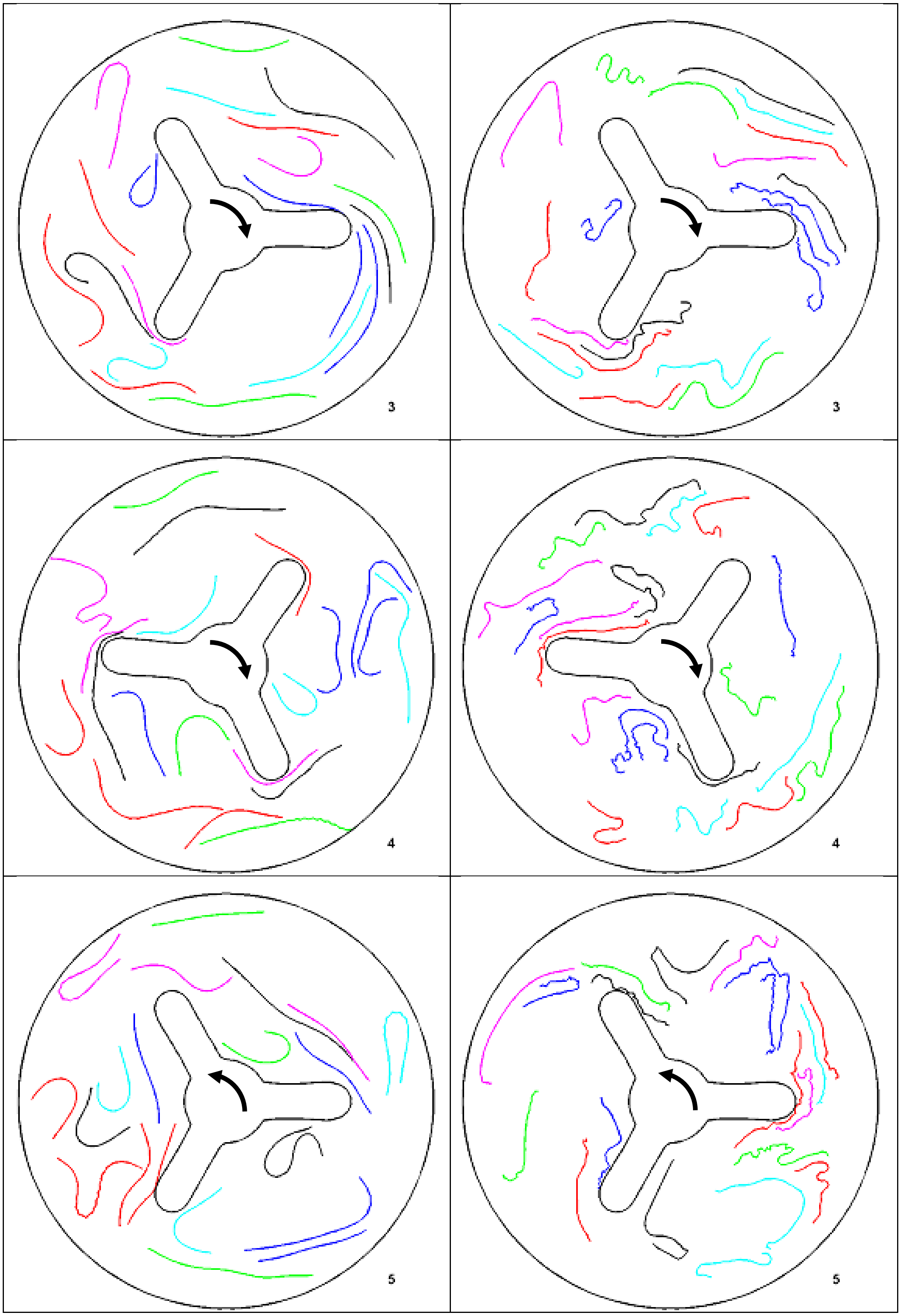
3
3
4
4
5
5

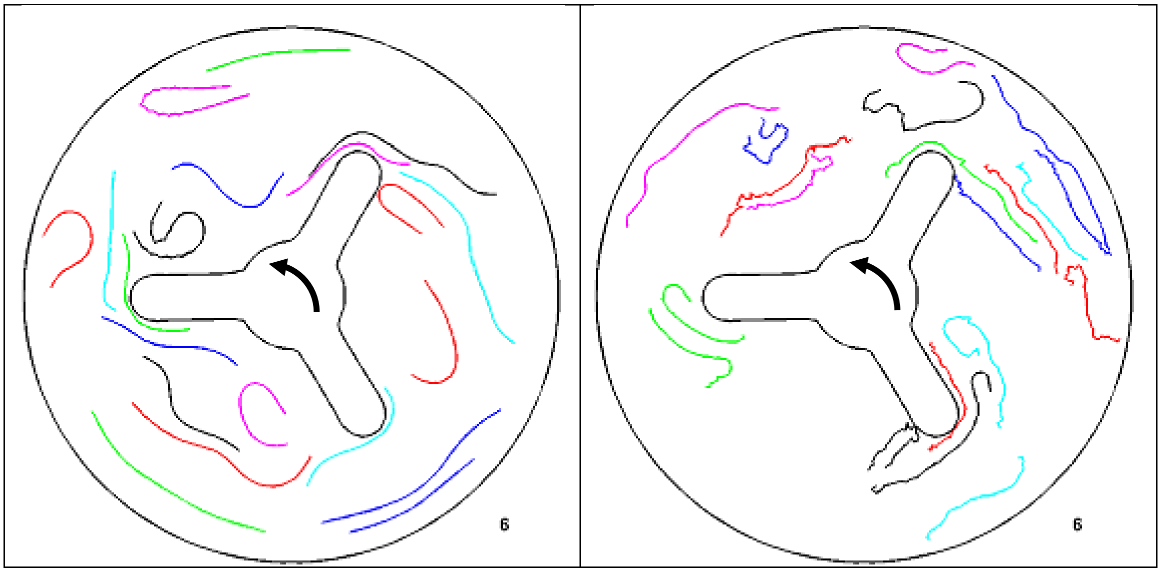

Figure 5.4-4: Effect of changing bending stiffness on cloth motion with $Re = 1.3 \times 10^3$, $h/2r_o = 8.5 \times 10^{-3}$ and $\Delta t = 1.885 \times 10^{-4}$. The snapshots in the left column are for $Be = 2.6 \times 10^{-2}$ and the snapshots in the right column are for $Be = 2.6 \times 10^{-5}$. Snapshots differ by a quarter period of the agitator cycle corresponding to 180° rotation

5.5 Three-dimensional simulations

Unlike the previously presented two-dimensional simulations, the three-dimensional simulations are the ultimate goal of this study. As said before in Section 5.1, this study so far involves only vertical-axis washing machines. As also noted in Section 5.1, the Reynolds number estimate of the washing machine processes based on the washtub drum radius requires a very fine grid to resolve all the rich physical details (including the length scale where energy is dissipated), and this current study lacks the required computing power for using such a fine grid or a shortcut turbulence model to be used with coarse grids. Note that, the Reynolds number prediction based on the tight inter-cloth spacings might be orders of magnitude lower than the estimate based on the washtub drum radius. The expected operation count of the simulation is of order $n\log n+m$, where n is the number of the grid points of the fixed Eulerian grid and m is the total number Lagrangian points of all the cloth pieces in the washtub. This suggests that for $n >> m$ (which may not be true in general) doubling the Eulerian grid resolution slows the simulation almost 8 times. So the following simulations are done by using a coarse grid size of 33 x 33 x 33, but as will be shown later, even these simulations reveal some of the intuitive characteristics of the washing machine processes.

Also as will be shown later, with dense cloth loads cloth pieces tend to move together, lacking individual motions. Part of the reason for this is the cloth pieces' 'artificial stickiness' due to the nature of the Immersed Boundary method, as will be discussed later.

5.5.1 Washtub geometry

Figure 5.5-1 below illustrates the washing machine agitator geometry that this simulation approximates and uses in the following studies. This agitator is currently used in modern Whirlpool washing machines. Unlike many other agitators, this agitator model is almost totally submerged in water. Note that, the agitator shown in Fig. 5.5-1 has a three-fold symmetry. The approximate shape and dimensions of this agitator are given in the projected views of Fig. 5.5-2 and 5.5-3, where z denotes the height from the bottom of the washtub, and $x'y'$ are local Cartesian axes on the one-third symmetric part, orthogonally spanning the horizontal plane with an origin at the radial center of the agitator. To simplify its description, only one-third of this symmetric geometry is plotted in the simplified drawings of Figs. 5.5-2 and 5.5-3.

For simplicity, the present simulation neglects the fillets and details with large curvatures. Due to the nature of the numerical method used for representing complex geometries on Cartesian grids (Chapter 4), the simulation cannot accurately represent geometries with relatively large curvatures on coarse grids. The holes on the agitator are also neglected. Also, a half sphere is added to the top-pole of the agitator to simplify the geometry.

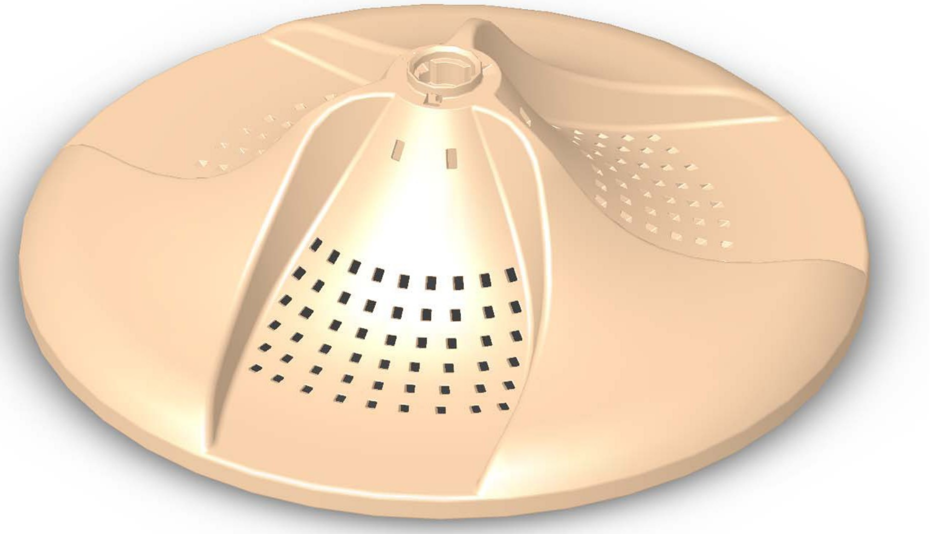

Figure 5.5-1: A mechanical agitator the Whirlpool Corporation uses in its modern washing machines

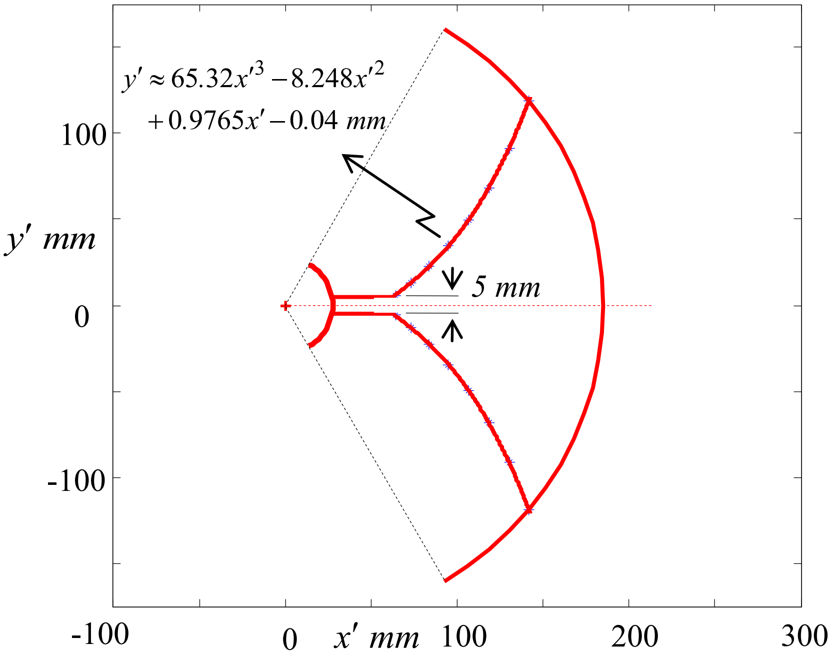

Figure 5.5-2: 120° partial simplified top view of the agitator shown in Fig. 5.5-1, with most of the small details and holes neglected. All dimensions are in millimeters. See Fig. 5.5-3 for any missing dimensions. The blue crosses denote the actual position of the surface edges that are approximated by a polynomial fit.

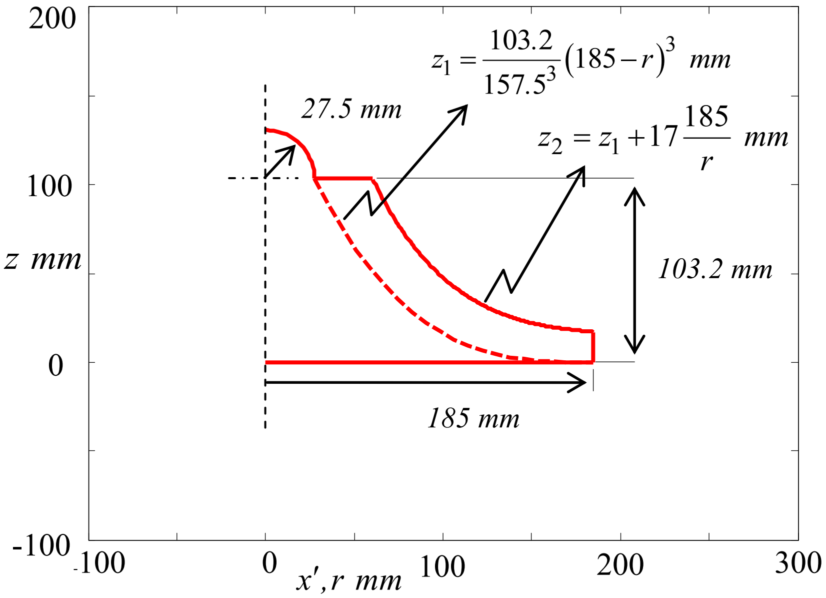

Figure 5.5-3: A partial simplified front view of the agitator shown in Fig. 5.5-1, with most of the small details and holes neglected. All dimensions are in millimeters. A half sphere with a radius of 27.5 mm is added to the top-pole of the agitator.

In addition to the agitator, the washtub has an outer nonmoving (except for the spin cycle not modeled here) cylinder with a radius of 31 cm.

The form of the washtub used in the simulations is as shown in Fig. 5.5-4 below. As shown there, the water height is assumed be fixed at a distance 23.76 cm away from the bottom wall of the washtub.

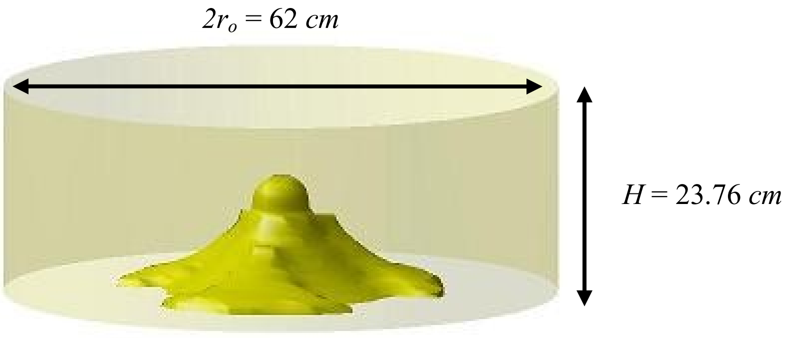

Figure 5.5-4: The form of the washtub used in the simulations

5.5.2 Initial cloth positions

Figure 5.5-5 shows the initial cloth positions in all the reported simulations of this study. The square cloth pieces are positioned in a radial arrangement with respect to the center of the washtub. The reason for choosing such an arrangement is in its simplicity to automate the cloth positioning mechanism, while ensuring them to not cross into each other or into the washtub geometry. However, to quickly obtain individual cloth motions this symmetric position is slightly perturbed by shifting the radial centers of the cloth pieces and tilting them across a normal axis through their centroids.

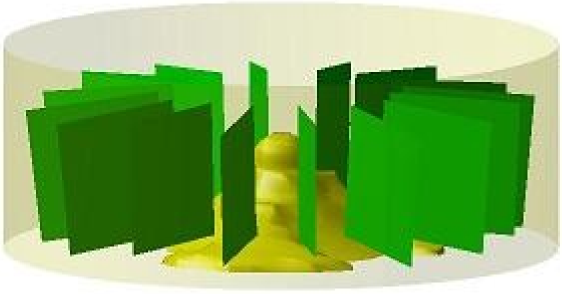

Figure 5.5-5: Initial cloth positions in all the simulations of this study

5.5.3 Operating conditions, physical properties, numerical parameters, and other numerical details used in the simulations

Table 5.5-1 below tabulates the operating conditions[4], physical and numerical properties used in the simulations, unless noted elsewhere. The computational domain is much wider in its lateral directions than its height direction. For this reason, the simulation uses a three times denser Eulerian grid in the washtub height direction. In Table 5.5-1 $h_{lateral}$ denotes to the Eulerian mesh width along the washtub lateral directions, whereas h_{height} is the mesh width along the washtub height direction. Note that, as mentioned in Briggs et al. (2000), using such a non-uniform grid slows down the convergence characteristics of the Geometric Multigrid solver used to solve the pressure-correction part of the Navier-Stokes equations solver, - the bottleneck part of the simulation as explained in Chapter 2, Section 2.2.6.

---

[4] The operating conditions of the agitator are as suggested by the Whirlpool Corporation.

Table 5.5-1: Operating conditions, physical and numerical parameters used in the simulations

Peak impeller rotation rate (ω_{max})	120 rpm
Number of revolutions in each direction before reversing	1
Cloth extensional stiffness (K_e)	$8\text{x}10^5$ N/m
Cloth in-plane shear stiffness (K_s)	$3\text{x}10^2$ N/m
Cloth Poisson's ratio (ν)	0
Cloth bending stiffness (K_b)	$1\text{x}10^{-5}$ N.m
Cloth torsional stiffness (K_t)	$1\text{x}10^{-5}$ N.m
Cloth excess mass per unit surface area (ρ_s) (with respect to the density of water)	$9.3\text{x}10^{-2}$ kg/m^2
Cloth dimensions (L x L)	15 cm x 15 cm (square)
Average cloth thickness (q)	2.4 x 10^{-4} m
Water density (ρ_f)	$1\text{x}10^3$ kg/m^3
Water dynamic viscosity (μ)	$1\text{x}10^{-3}$ kg/(m.s)
Dirac-delta function half width (ε_δ)	$2h_{lateral}$ and $2h_{height}$
Heaviside function half width (ε)	0
Minimum Lagrangian to Eulerian mesh size ratio on the undeformed cloth	1.15
$h_{lateral} / 2r_o$	3.48 x 10^{-2}
$h_{lateral} / h_{height}$	3

The Lagrangian mesh size mentioned in Table 5.5-1 is measured along the constant *r* and *s* lines defined in Section 5.2. To follow the standard convention, the material constants are reported as lower-dimensional quantities. For instance, the cloth extensional stiffness (K_e) is proportional to cloth's Young's modulus times thickness *q* (i.e. $\bar{E}q$). Again, with a simple calculation the operating conditions of the agitator given in Table 5.5-1 can be implied by the following form of angular velocity

$$\omega = \omega_{max} \, sin\left(2\pi f \, t\right) \tag{5.5-1}$$

with

$$\omega_{max} = 4\pi \quad \left[\text{rad/s}\right] \tag{5.5-2}$$

$$f = \frac{\pi}{2} \quad [1/\mathrm{s}] \tag{5.5-3}$$

where ω is the angular velocity of the agitator, f is the frequency of agitator's rotation cycle, and t is time. In Eqn. (5.5-1) ω and t respectively have the units of rad/s and s, if using Eqn (5.5-2) and (5.5-3).

In all the simulations the upper surface of the washtub (Fig. 5.5-4) is modeled as a nonmoving, slip-free, and impermeable boundary to approximate a free surface. As shown in Fig. 5.5-5, for simplicity, all the cloth pieces are modeled as squares. The simulation uses the forward Euler method to numerically solve Eqn. (3.2-14).

5.5.4 Dimensionless groups

The dimensionless groups describing the three-dimensional washing machine processes will be deduced from the lower dimensional development of Section 5.4.3. Doing so, the following length, time, and mass scales are used

$$l^o = r_o, \quad t^o = 1/\omega_{max}, \quad M^o = \rho_f r_o^3 \tag{5.5-4}$$

where $2r_o$ is the washtub diameter as shown in Fig. 5.5-4. As before, the average cloth thickness q, whose definition and measurement is as given in Section 5.3, is used to scale the desingularized cloth properties.

Using these scales, the following dimensionless groups could be deduced using the results given in Section 5.4.3.

$$Re = \frac{\rho_f r_o^2 \omega_{max}}{\mu} \tag{5.5-5}$$

$$Te = \frac{K_e}{\rho_f \left(\omega_{max} r_o\right)^2 q} \tag{5.5-6}$$

$$Se = \frac{K_s}{\rho_f \left(\omega_{max} r_o\right)^2 q} \tag{5.5-7}$$

$$Be = \frac{K_b}{\rho_f \omega_{max}^2 r_o^4 q} \tag{5.5-8}$$

$$To = \frac{K_t}{\rho_f \omega_{max}^2 r_o^4 q} \tag{5.5-9}$$

$$In = \frac{\rho_s}{\rho_f q} \tag{5.5-10}$$

$$St = \frac{f}{\omega_{max}} \tag{5.5-11}$$

In above, *Se* and *To* are dimensionless groups related to the cloth in-plane shear and torsional stiffness. The dimensional values given in Section 5.5.1 and 5.5.3 correspond to the dimensionless values given in Table 5.5-2 below, which are used in the simulations unless noted elsewhere.

Table 5.5-2: Dimensionless groups used in the simulations unless reported elsewhere

Re	1.2×10^{6}
Te	2.2×10^{5}
Se	82.4
Be	2.9×10^{-5}
To	2.9×10^{-5}
In	0.3875
St	0.125

5.5.5 Results

5.5.5.1 Effect of changing the time step Δt

In this study the effect of changing the simulation time step on the statistics of the absolute cloth stresses and the stability of the code is examined. Tables 5.5-3 to 5.5-5 respectively tabulate the statistics of $|\sigma_{ss}|_{max}$, $|\sigma_{rr}|_{max}$, $|\sigma_{sr}|_{max}$ (as defined in Section 5.2) up to the first 2 agitation cycles. The results are given for 16 cloth pieces, $Re = 1.2 \times 10^4$, and defining $\Delta t^* = 1.01 \times 10^{-3}$.

Table 5.5-3: Effect of changing the time step on $|\sigma_{ss}|_{max}$ during the first 2 agitation cycles for 16 cloth pieces with $Re = 1.2 \times 10^4$ and defining $\Delta t^* = 1.01 \times 10^{-3}$

Time step	Average $\|\sigma_{ss}\|_{max}$ [MPa]	Standard deviation [MPa]
Δt^*	0.418	0.242
$\Delta t^*/2$	0.615	0.317
$\Delta t^*/4$	0.699	0.366

Table 5.5-4: Effect of changing the time step on $|\sigma_{rr}|_{max}$ during the first 2 agitation cycles for 16 cloth pieces with $Re = 1.2 \times 10^4$ and defining $\Delta t^* = 1.01 \times 10^{-3}$

Time step	Average $\|\sigma_{rr}\|_{max}$ [MPa]	Standard deviation [MPa]
Δt^*	0.424	0.244
$\Delta t^*/2$	0.630	0.307
$\Delta t^*/4$	0.747	0.358

Table 5.5-5: Effect of changing the time step on $|\sigma_{sr}|_{max}$ during the first 2 agitation cycles for 16 cloth pieces with $Re = 1.2 \times 10^4$ and defining $\Delta t^* = 1.01 \times 10^{-3}$

Time step	Average $\|\sigma_{sr}\|_{max}$ [MPa]	Standard deviation [MPa]
Δt^*	0.0375	0.0169
$\Delta t^*/2$	0.0409	0.0188
$\Delta t^*/4$	0.0441	0.0208

The above tables show that the average absolute cloth stresses increase with lowering the time step, but with a hint of convergence for $|\sigma_{ss}|_{max}$ and $|\sigma_{rr}|_{max}$. In all the simulation results reported here the cloth shapes were very crumpled, suggesting the effect of the unresolved wrinkles on the cloth bending stresses can get significantly lower with using a higher spatial resolution to better capture the complex deformed cloth geometries.

Furthermore, the simulations using Δt^* and $\Delta t^*/2$ crashed after the 2.9th and 5.3rd agitation cycle, respectively, but on the other hand the simulation using $\Delta t^*/4$ was still running at the end of its 7.4th cycle. The reason why these simulations crashed seems to be a ‘geometric’ problem and is explained using the representative pathlines of the motion of the cloth pieces inside the washtub as plotted in Fig. 5.5-6 below. The inertial effect of the agitator pushes the cloth pieces towards the outer drum at the bottom of the washtub (1). However, mass continuity requires these same cloth pieces to elevate near the outer drum and then to move towards the center of the washtub (2). While the cloth pieces descend towards the bottom center of the washtub, if the time step is not small the cloth pieces accidentally come very close to the agitator and sometimes slightly penetrate into it (3). Since the agitator is moving relatively fast compared to the surrounding fluid, the agitator may cause the cloth to deform very irregularly, which in turn leads to very high cloth elastic forces crashing the simulation. This problem will be referred as the ‘geometric’ instability, since it is caused by the cloth pieces movements inside the washtub.

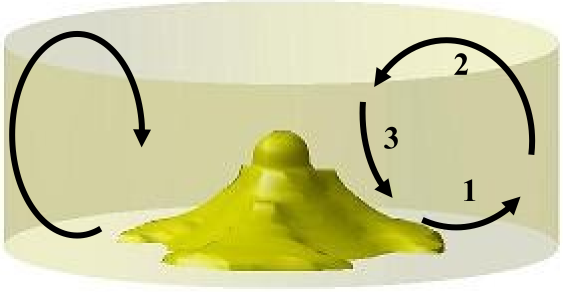

Figure 5.5-6: The representative pathlines of the cloth pieces inside the washtub

5.5.5.2 Effect of changing the Reynolds number

This study examines the effect of changing the Reynolds number Re on the cloth motion using the same Eulerian grid size. On the electronic pdf version of this document click on the blue colored Re value to view the cloth motion as an embedded movie file: **$Re = 1.2 \times 10^{2}$**, **$Re = 1.2 \times 10^{3}$**, **$Re = 1.2 \times 10^{4}$**, **$Re = 1.2 \times 10^{5}$**, and **$Re = 1.2 \times 10^{6}$**. Specifically, look for the relative speed of the tumbling motion. These simulations use 16 cloth pieces and $\Delta t = 5.03 \times 10^{-4}$, except for the case $Re = 1.2 \times 10^{4}$ with $\Delta t = 2.51 \times 10^{-4}$.

Figure 5.5-7 shows snapshots of the cloth motion for $Re = 1.2 \times 10^{4}$ (left column), $Re = 1.2 \times 10^{3}$ (middle column), and $Re = 1.2 \times 10^{2}$ (right column). The snapshots differ by a half agitation cycle, corresponding to the full rotation of the agitator in one direction. As mentioned above, look for the relative speed of the tumbling motion (as described in Fig. 5.5-6) of the two dark colored cloth pieces.

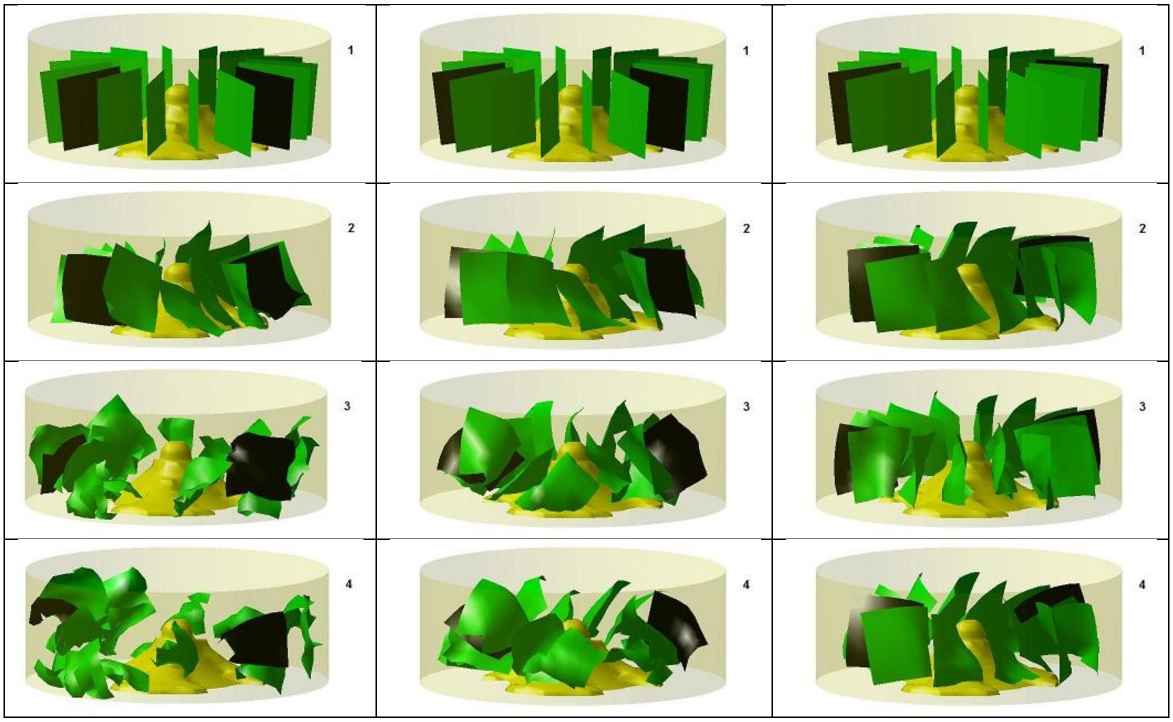

5	5	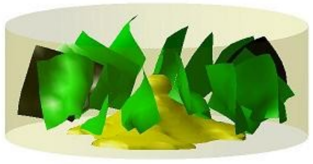5
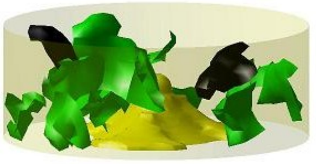6	6	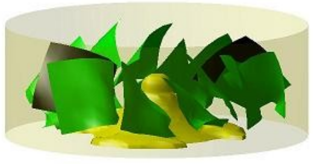6
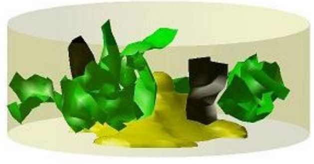7	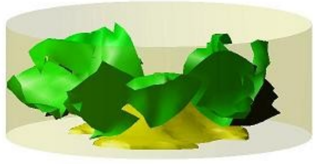7	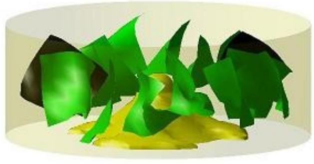7
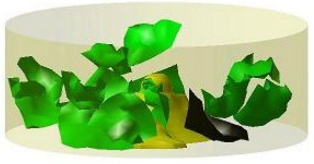8	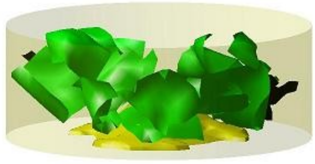8	8
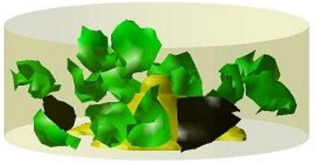9	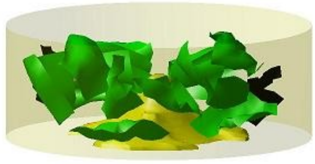9	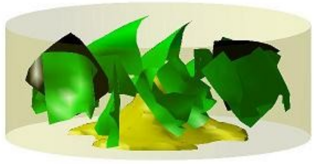9
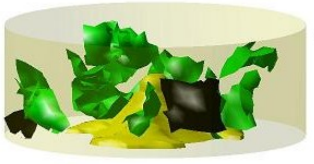10	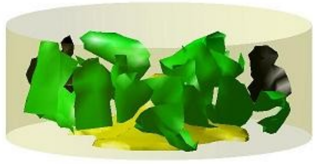10	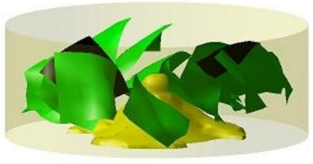10
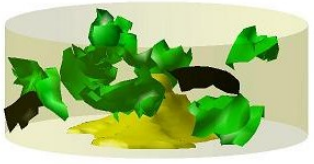11	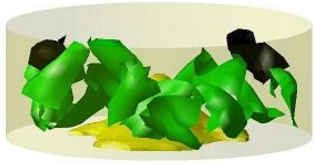11	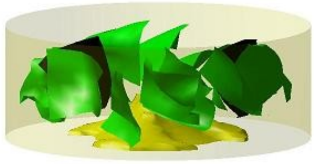11
12	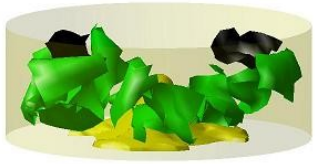12	12
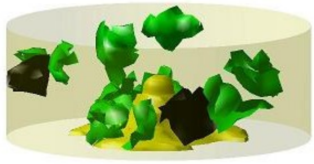13	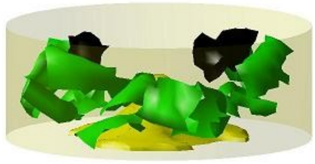13	

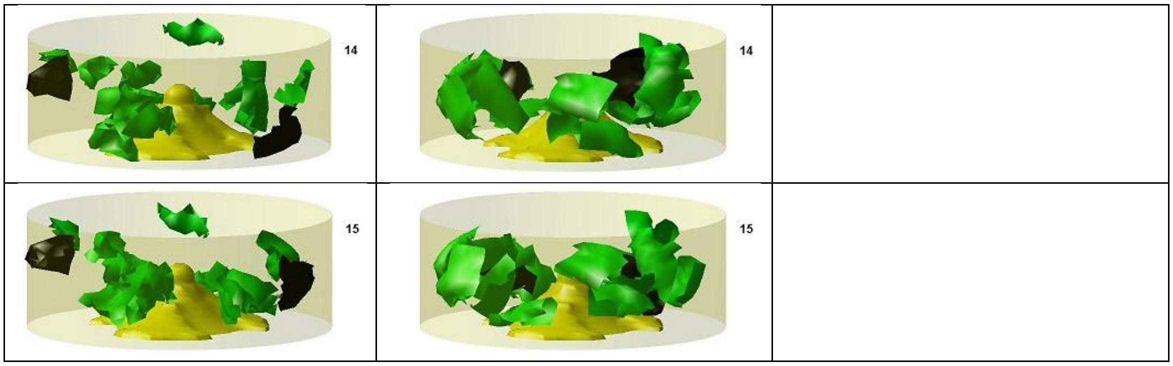

Figure 5.5-7: Illustrative snapshots of the motion of 16 cloth pieces with *Re* = 1.2 x 10^4 (left column), 1.2 x 10^3 (middle column), and 1.2 x 10^2 (right column). Snapshots differ by a half agitation cycle, corresponding to the full rotation of the agitator in one direction.

It is visually apparent from the snapshots and their accompanying movies that with higher *Re* the tumbling motion of the cloth pieces gets slower, while they show a more pronounced rotational motion with the agitator. This is not surprising, since the local agitator motion will diffuse farther away in a more viscous fluid. In addition, Figs. 5.5-8 to 5.5-12 illustrate the trajectories of : i) all the cloth pieces' common center of mass position (left column) and ii) each of the 16 cloth pieces' center of mass position (right column) on a plane spanned by the height z from the bottom of the washtub and the horizontal radius r_{xy}. This horizontal radius is defined as

$$r_{xy} = \sqrt{x^2 + y^2} \qquad \textbf{(5.5-12)}$$

where x and y are the horizontal Cartesian coordinates of the center of mass positions measured from the radial center of the agitator (Fig. 5.5-4).

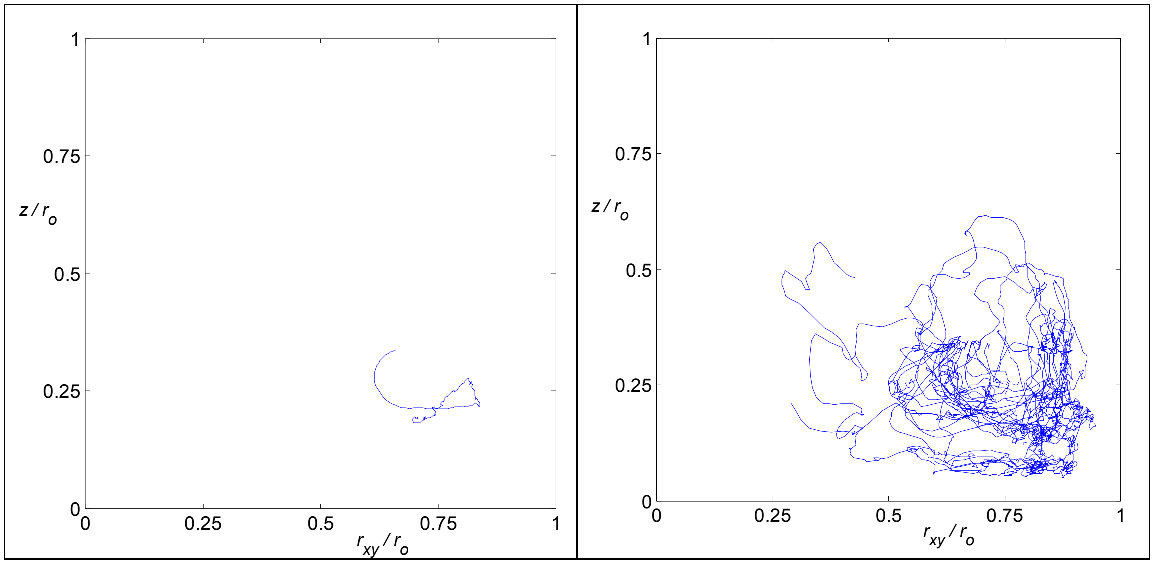

Figure 5.5-8: All the cloth pieces' (left column) and each cloth piece's (right column) center of mass trajectories up to 5.5 agitation cycles at *Re* = 1.2 x 10^6

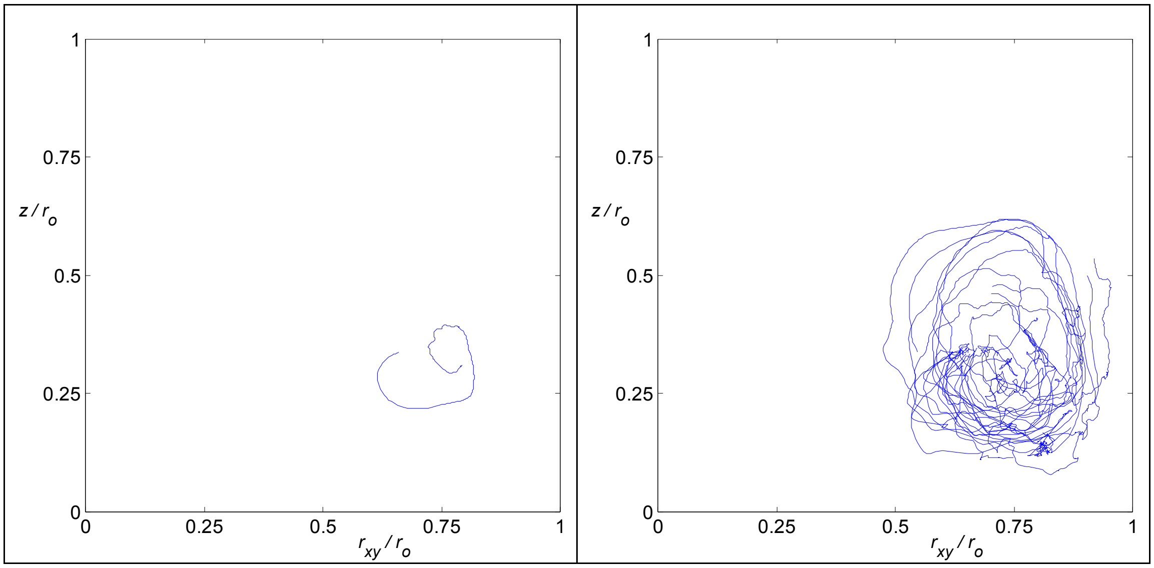

Figure 5.5-9: All the cloth pieces' (left column) and each cloth piece's (right column) center of mass trajectories up to 5.5 agitation cycles at *Re* = 1.2 x 10^5

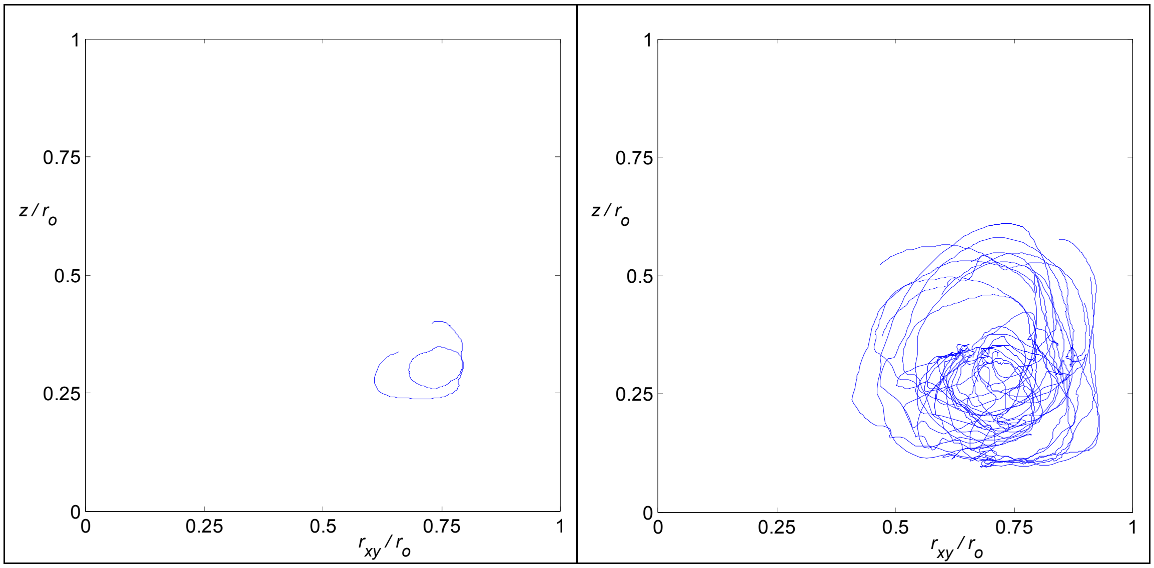

Figure 5.5-10: All the cloth pieces' (left column) and each cloth piece's (right column) center of mass trajectories up to 5.5 agitation cycles at *Re* = 1.2 x 10^4

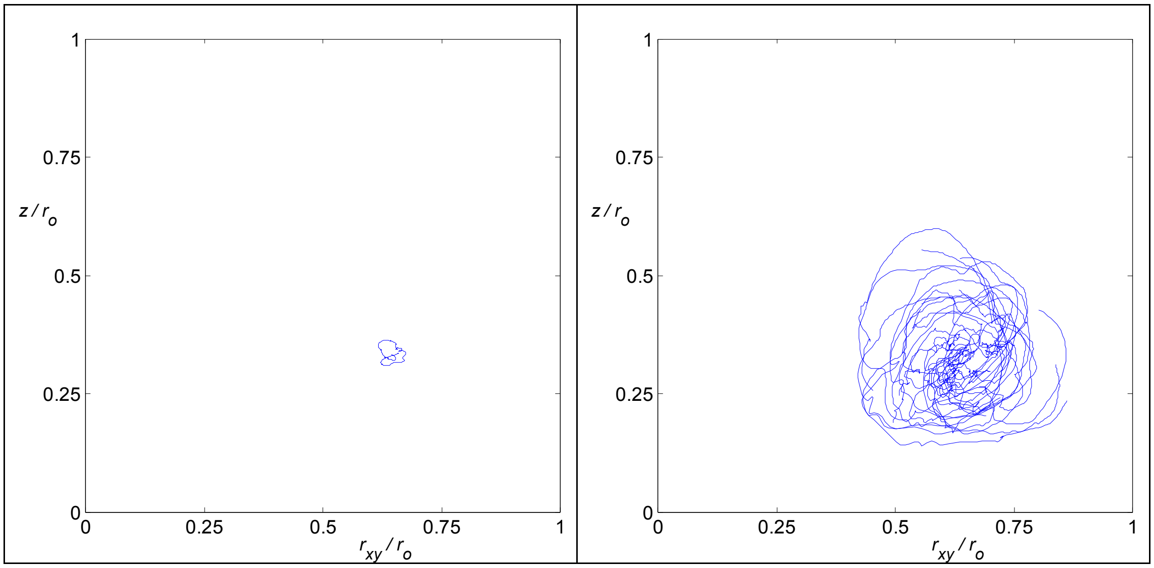

Figure 5.5-11: All the cloth pieces' (left column) and each cloth piece's (right column) center of mass trajectories up to 5.5 agitation cycles at *Re* = 1.2 x 10^3

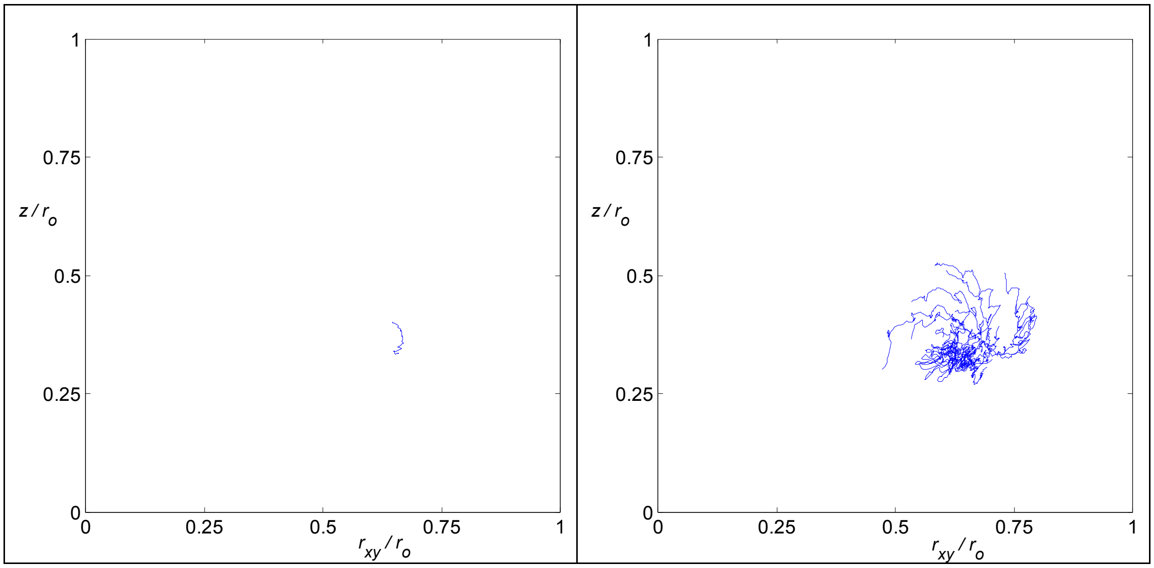

Figure 5.5-12: All the cloth pieces' (left column) and each cloth piece's (right column) center of mass trajectories up to 5.5 agitation cycles at *Re* = 1.2 x 10^2

At *Re* = 1.2 x 10^6 some of the cloth pieces stayed at the bottom of the washtub or at the corner between the bottom wall and the outer drum for most of the simulation time (possibly due to the insufficient simulation resolution). Observe in the left column of Figs. 5.5-8 to 5.5-12 that all the cloth pieces' center of mass positions move across a significantly wider area at higher *Re* (1.2 x 10^6, 1.2 x 10^5, and 1.2 x 10^4) compared to the trajectory at *Re* = 1.2 x 10^3. At *Re* = 1.2 x 10^3 the cloth pieces still tumbled, but they moved around tight rings formed of multiple cloth pieces as illustrated in Fig. 5.5-13 below, where the cloth pieces were at a different phase position and the average center of mass position of all the cloth pieces was approximately stagnant. These rings were still present at *Re* = 1.2 x 10^4, but they were not as dominant on the overall cloth motion. On the other hand, at *Re* = 1.2 x 10^2 the cloth pieces had a very low tumbling rate and the center of mass positions of most of the cloth pieces were aligned with respect to each other (for at least up to the first 11 agitation cycles).

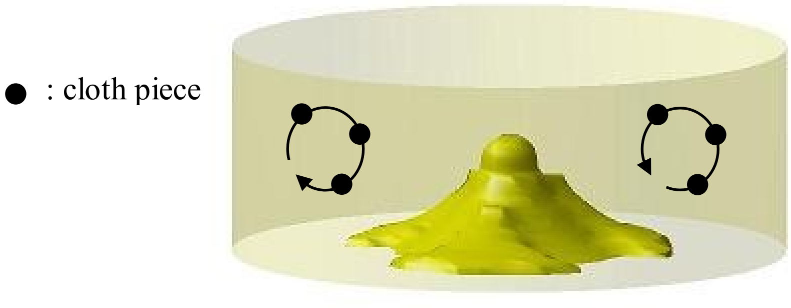

Figure 5.5-13: Cloth pieces moving in different phases around circular rings at *Re* = 1.2 x 10^3

Tables 5.5-6 to 5.5-8 tabulate the statistics of $|\sigma_{ss}|_{max}$, $|\sigma_{rr}|_{max}$, and $|\sigma_{sr}|_{max}$ (defined in Section 5.2) up to 8 agitation cycles using the same grid size.

Table 5.5-6: Effect of changing *Re* on the statistics of $|\sigma_{ss}|_{max}$ after 8 agitation cycles for 16 cloth pieces using the same Eulerian grid size and *Δt* = 5.03 x 10^{-4} (except the case *Re* = 1.2 x 10^4, which uses *Δt* = 2.51 x 10^{-4})

Re	Average $|\sigma_{ss}|_{max}$ [MPa]	Standard deviation [MPa]
1.2 x 10^2	0.069	0.021
1.2 x 10^3	0.160	0.096
1.2 x 10^4	0.651	0.345
1.2 x 10^5	1.022	0.286

Table 5.5-7: Effect of changing *Re* on the statistics of $|\sigma_{rr}|_{max}$ after 8 agitation cycles for 16 cloth pieces using the same Eulerian grid size and *Δt* = 5.03 x 10^{-4} (except the case *Re* = 1.2 x 10^4, which uses *Δt* = 2.51 x 10^{-4})

Re	Average $|\sigma_{rr}|_{max}$ [MPa]	Standard deviation [MPa]
1.2 x 10^2	0.061	0.018
1.2 x 10^3	0.153	0.079
1.2 x 10^4	0.847	0.340
1.2 x 10^5	1.067	0.836

Table 5.5-8: Effect of changing *Re* on the statistics of $|\sigma_{sr}|_{max}$ after 8 agitation cycles for 16 cloth pieces using the same Eulerian grid size and *Δt* = 5.03 x 10^{-4} (except the case *Re* = 1.2 x 10^4, which uses *Δt* = 2.51 x 10^{-4})

Re	Average $|\sigma_{sr}|_{max}$ [MPa]	Standard deviation [MPa]
1.2 x 10^2	0.0280	0.0084
1.2 x 10^3	0.0268	0.0086
1.2 x 10^4	0.0516	0.0171
1.2 x 10^5	0.0723	0.0178

At high *Re* (especially higher than 1.2 x 10^4) the cloth pieces showed a very noisy motion. In particular, for *Re* = 1.2 x 10^6 the stress statistics were discontinuous after the 2nd agitation cycle. For this reason the statistical results are repeated in Tables 5.5-9 to 5.5-11 for the first two agitation cycles (but this time including *Re* = 1.2 x 10^6).

Table 5.5-9: Effect of changing *Re* on the statistics of $|\sigma_{ss}|_{max}$ after 2 agitation cycles for 16 cloth pieces using the same Eulerian grid size and *Δt* = 5.03 x 10^{-4} (except the case *Re* = 1.2 x 10^4, which uses *Δt* = 2.51 x 10^{-4})

Re	Average $|\sigma_{ss}|_{max}$ [MPa]	Standard deviation [MPa]
1.2 x 10^2	0.077	0.028
1.2 x 10^3	0.096	0.055
1.2 x 10^4	0.699	0.366
1.2 x 10^5	1.119	0.477
1.2 x 10^6	1.308	0.571

Table 5.5-10: Effect of changing *Re* on the statistics of $|\sigma_{rr}|_{max}$ after 2 agitation cycles for 16 cloth pieces using the same Eulerian grid size and *Δt* = 5.03 x 10^{-4} (except the case *Re* = 1.2 x 10^4, which uses *Δt* = 2.51 x 10^{-4})

Re	Average $|\sigma_{rr}|_{max}$ [MPa]	Standard deviation [MPa]
1.2 x 10^2	0.062	0.022
1.2 x 10^3	0.103	0.049
1.2 x 10^4	0.748	0.358
1.2 x 10^5	1.608	1.535
1.2 x 10^6	1.294	0.532

Table 5.5-11: Effect of changing *Re* on the statistics of $\left|\sigma_{sr}\right|_{max}$ after 2 agitation cycles for 16 cloth pieces using the same Eulerian grid size and Δt = 5.03 x 10^{-4} (except the case *Re* = 1.2 x 10^{4}, which uses Δt = 2.51 x 10^{-4})

Re	Average $\left\|\sigma_{sr}\right\|_{max}$ [MPa]	Standard deviation [MPa]
1.2 x 10^2	0.0270	0.0093
1.2 x 10^3	0.0197	0.0073
1.2 x 10^4	0.0441	0.0208
1.2 x 10^5	0.0525	0.0201
1.2 x 10^6	0.0697	0.0307

In the above results, the average absolute cloth stresses increased with increasing *Re*. However, as a note of caution, the low *Re* results were better resolved thanks to the straightforwardness of the fluid motion, which in turn leads to smoother cloth geometries resulting into lower bending stresses.

5.5.5.3 Effect of changing the cloth loading

In this case study, the effect of changing the cloth loading in the washtub on the cloth motion and statistics of the cloth stresses is examined using a fixed Eulerian grid size at *Re* = 1.2 x 10^3, and Δt = 5.03 x 10^{-4}. The ratio of the total dry mass of the cloth pieces to the mass of the water in the washtub is approximately 1.7 x 10^{-3}, 3.3 x 10^{-3}, and 6.6 x 10^{-3} for the simulations with 16, 32, and 64 cloth pieces, respectively. This suggests that the heaviest cloth loading studied here is roughly ten times lighter than a real laundry load. On the electronic pdf version of this document click on the blue colored cloth load in the washtub to view the cloth motion as an embedded movie file: **16 cloth pieces**, **32 cloth pieces**, and **64 cloth pieces**. In particular, compare the relative speeds of the cloth pieces' tumbling motion.

The left, middle, and right columns of Fig. 5.5-14 respectively show snapshots from the motion of 16, 32 and 64 cloth pieces. The snapshots differ by a half agitation cycle, corresponding to the full rotation of the agitator in one direction. In particular, compare the relative speeds of the two dark colored cloth pieces' tumbling motion.

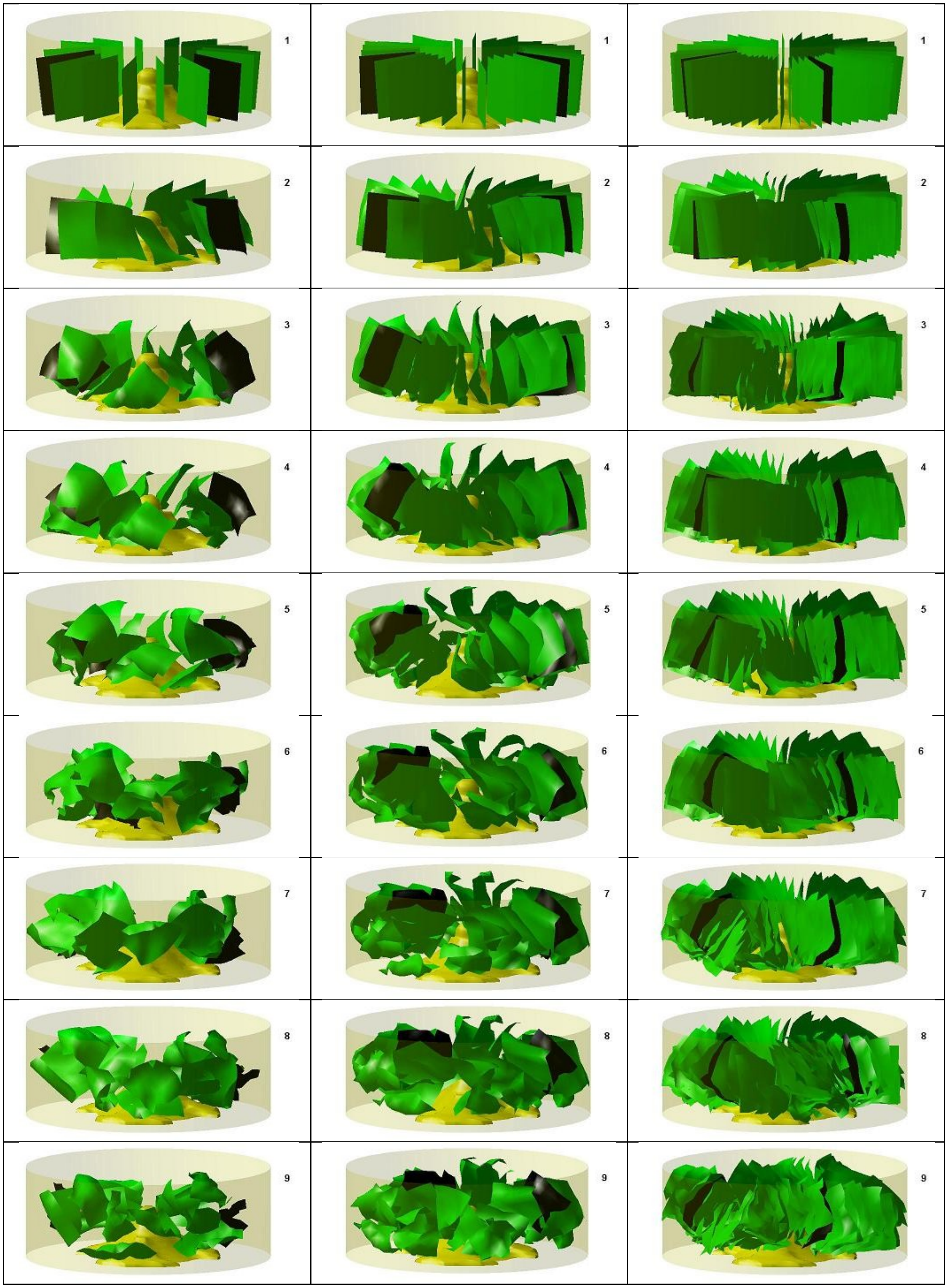
1
1
1
2
2
2
3
3
3
4
4
4
5
5
5
6
6
6
7
7
7
8
8
8
9
9
9

Figure 5.5-14: Illustrative snapshots of the motion of 16 (left column), 32 (middle column), and 64 (right column) cloth pieces with *Re* = 1.2 x 10^3, Δt = 5.03 x 10^{-4}. Snapshots differ by a half agitation cycle, corresponding to the full rotation of the agitator in one direction.

Also, Figs. 5.5-15 to 5.5-17 illustrate the trajectories of: i) all the cloth pieces' common center of mass position (left column) and ii) each cloth piece's center of mass position (right column) on a plane spanned by the height z from the bottom of the washtub and the horizontal radius r_{xy} up to the first 6 agitation cycles. This horizontal radius was defined in Eqn. (5.5-12). Since all these trajectories span the same time period, one can compare their shapes to estimate the relative tumbling rates, which is easier by using the trajectories of all the cloth pieces' common center of mass positions (left column). In particular observe that, the trajectory for the case with 64 cloth pieces completes a quarter tumbling cycle, while the trajectory completes more than one tumbling cycle for the case with 16 cloth pieces.

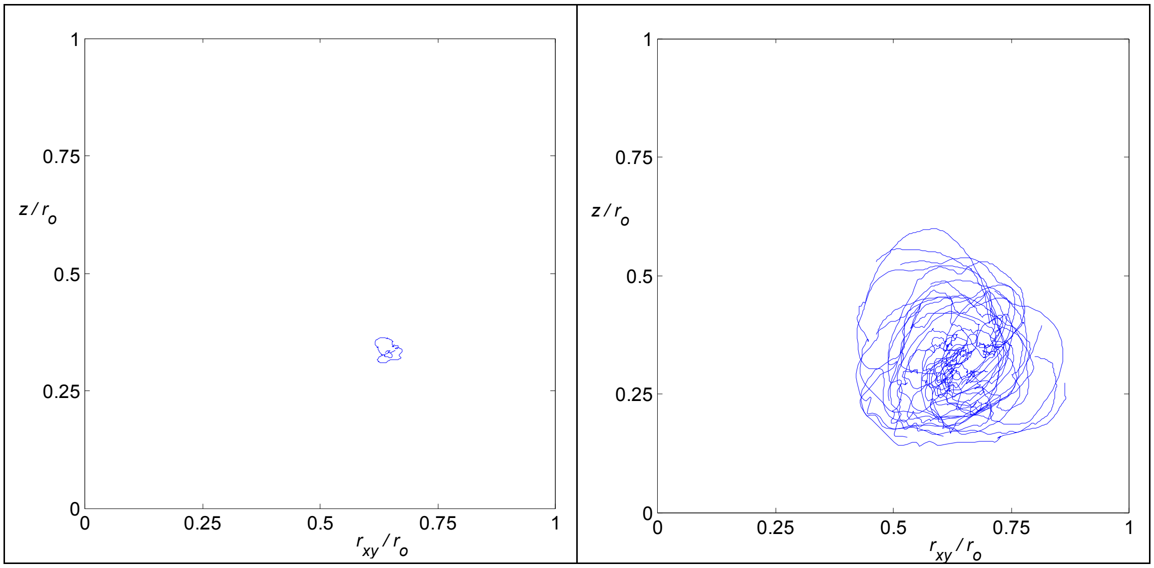

Figure 5.5-15: All the cloth pieces' (left column) and each cloth piece's (right column) center of mass trajectories for a cloth loading of 16 pieces at *Re* = 1.2 x 10^3, up to the first 6 agitation cycles

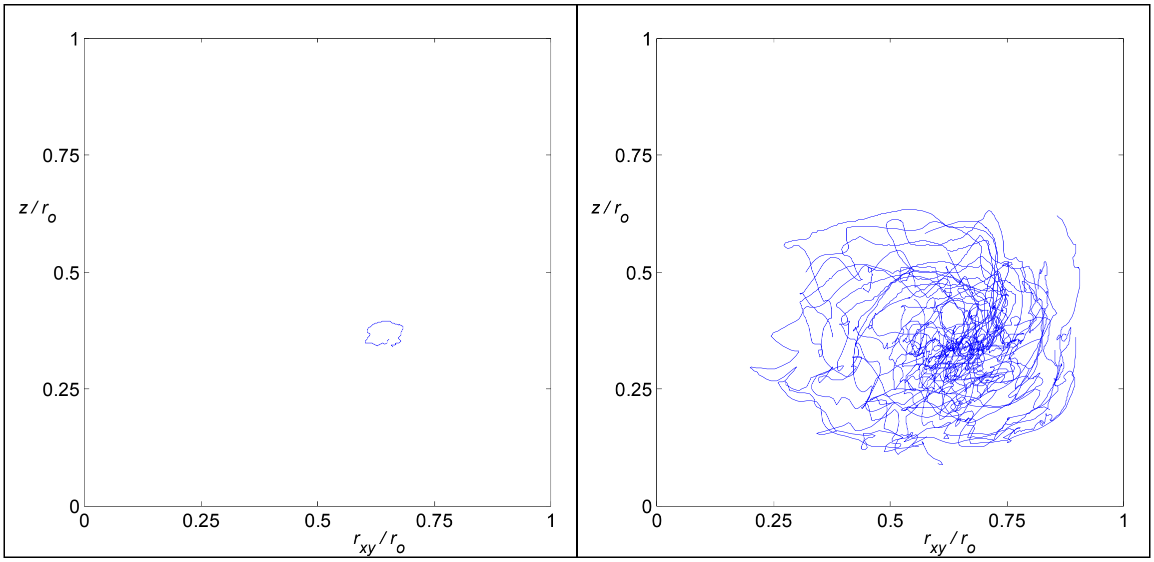

Figure 5.5-16: All the cloth pieces' (left column) and each cloth piece's (right column) center of mass trajectories for a cloth loading of 32 pieces at *Re* = 1.2 x 10^3, up to the first 6 agitation cycles

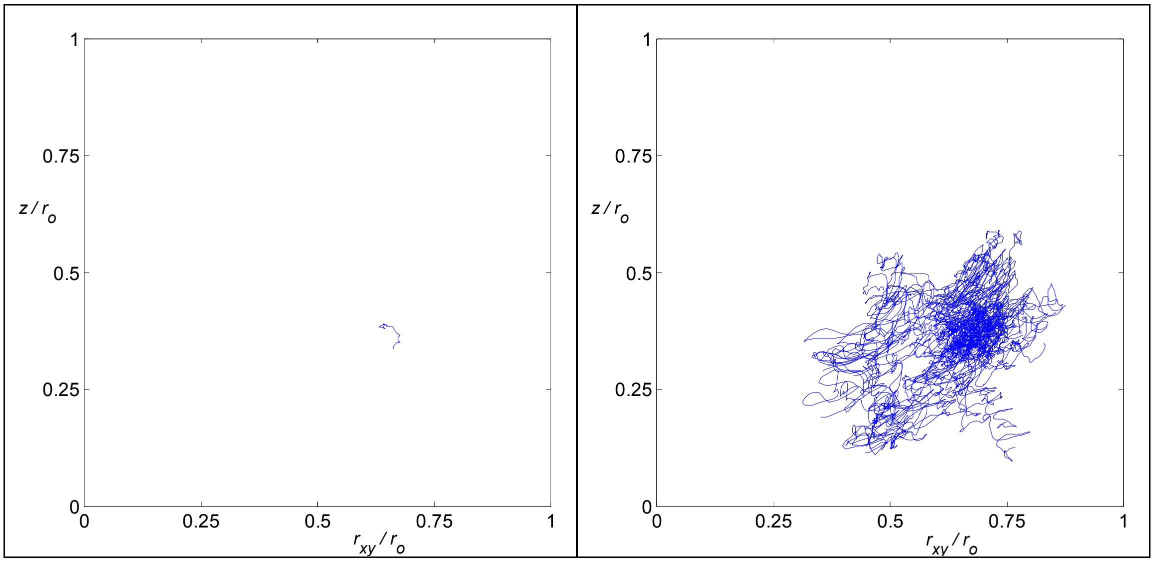

Figure 5.5-17: All the cloth pieces' (left column) and each cloth piece's (right column) center of mass trajectories for a cloth loading of 64 pieces at *Re* = 1.2 x 10^3, up to the first 6 agitation cycles

Also, by comparing the snapshot sequences in Fig. 5.5-14 and by viewing the movies, it is clear that the cloth pieces move together, lacking individual motions, when the cloth loading is increased in the washtub with a fixed grid resolution. Although part of the reason for this might be the increased viscous effects that occur with smaller cloth spacings, another reason is the effect of the artificial cloth stickiness due to the overlapping Dirac-delta function approximations used in the formulation of the simulation. This will be further discussed in the next section. The use of the Dirac-delta functions in the mathematical formulation of the fluid/structure interaction algorithm was given in Chapter 3, Section 3.2 and their numerical implementation in the simulation was given in Chapter 3, Section 3.4.2.

Tables 5.5-12 to 5.5-14 tabulate the statistics of the maximum absolute stresses. The statistics are for the first 5 agitation cycles.

Table 5.5-12: Effect of the cloth loading on the statistics of $\left|\sigma_{ss}\right|_{max}$ after 5 agitation cycles with *Re* = 1.2 x 10^3, *Δt* = 5.03 x 10^{-4}, and using the same Eulerian grid size

Number of cloth pieces	Cloth to water mass fraction	Average $\left\|\sigma_{ss}\right\|_{max}$ [MPa]	Standard deviation [MPa]
16	1.7 x 10^{-3}	0.119	0.069
32	3.3 x 10^{-3}	0.143	0.080
64	6.6 x 10^{-3}	0.163	0.119

Table 5.5-13: Effect of the cloth loading on the statistics of $\left|\sigma_{rr}\right|_{max}$ after 5 agitation cycles with *Re* = 1.2 x 10^3, *Δt* = 5.03 x 10^{-4}, and using the same Eulerian grid size

Number of cloth pieces	Cloth to water mass fraction	Average $\left\|\sigma_{rr}\right\|_{max}$ [MPa]	Standard deviation [MPa]
16	1.7 x 10^{-3}	0.127	0.066
32	3.3 x 10^{-3}	0.131	0.077
64	6.6 x 10^{-3}	0.170	0.114

Table 5.5-14: Effect of the cloth loading on the statistics of $\left|\sigma_{sr}\right|_{max}$ after 5 agitation cycles with *Re* = 1.2 x 10^3, *Δt* = 5.03 x 10^{-4}, and using the same Eulerian grid size

Number of cloth pieces	Cloth to water mass fraction	Average $\left\|\sigma_{sr}\right\|_{max}$ [MPa]	Standard deviation [MPa]
16	1.7 x 10^{-3}	0.023	0.007
32	3.3 x 10^{-3}	0.027	0.012
64	6.6 x 10^{-3}	0.028	0.014

The results in the above tables show a very slight increase in the cloth average absolute stresses with increased cloth loading using the same Eulerian grid size.

5.5.5.4 Effect of changing the Dirac-delta function width

As explained in Chapter 3, Section 3.5.1.4 there are two possible places to alter the Dirac-delta function width, $2\varepsilon_\delta$, in the formulation: 1) in Eqn. (3.2-12) for desingularizing the infinitesimally thin cloth model onto the Eulerian grid, and 2) in Eqn. (3.2-13) for approximating the velocities of the Lagrangian cloth points from the Eulerian grid. Also, as examined in the verification study for capturing the natural frequencies of a vibrating plate, using smaller Dirac-delta function widths for desingularization gives more accurate but less stable results. On the other hand, using the same or a larger delta function width for the velocity approximation than the width used for desingularization yielded to more stable but less accurate results.

The effect of changing the Dirac-delta function width, 2ε, was also examined in the washing machine simulations. Similar to the conclusions of Chapter 3, using $2\varepsilon_\delta = 2h$ and $3h$ (h is the Eulerian mesh size) gave unstable results, likely because the desingularized forces were too discontinuous. However, using $2\varepsilon_\delta = 3h$ for the case of 64 cloth pieces with $Re = 1.2 \times 10^3$, $\Delta t = 5.03 \times 10^{-4}$, the cloth pieces hinted an increased individual mobility compared to the result with $2\varepsilon_\delta = 4h$ in Section 5.5.5.3 until the simulation crashed in the manner described in Section 5.5.5.1. This improvement might also be evidenced from Figs. 5.5-18 and 5.5-19 below, which plots the trajectories of: i) all cloth pieces' common center of mass position (left column) and ii) each cloth piece's center of mass position (right column) on a plane spanned by the height z from the bottom of the washtub and the horizontal radius r_{xy} (defined in Eqn. 5.5-12) for the first agitation cycle. Since all these trajectories span the same time period, one can compare their relative lengths to verify the increased mobility of the cloth pieces with a narrower Dirac-delta function width.

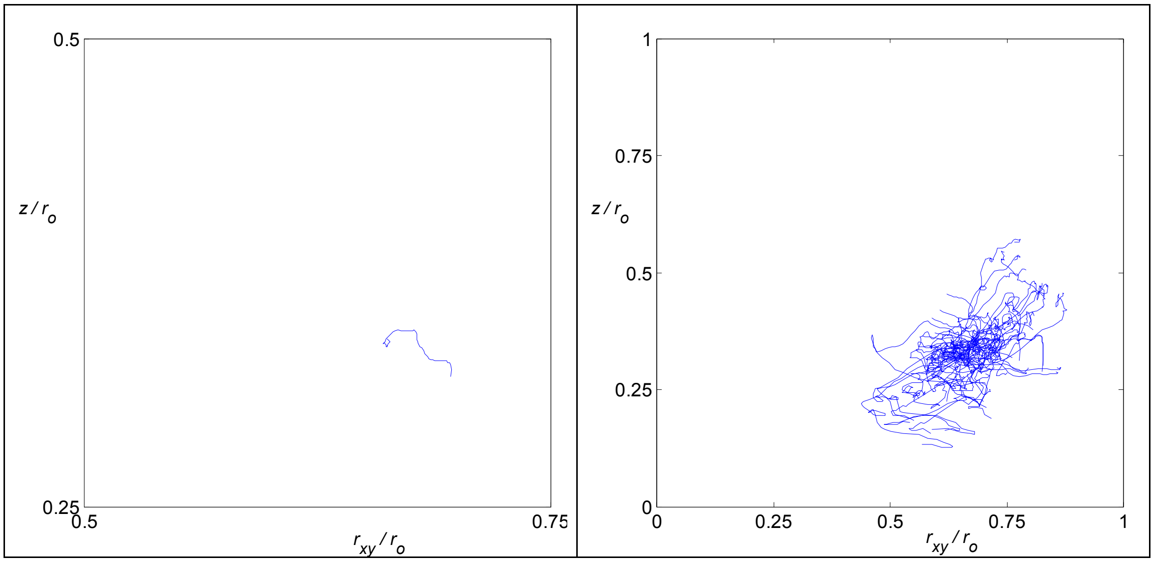

Figure 5.5-18: All cloth pieces' (left column) and each cloth piece's (right column) center of mass trajectories with $\varepsilon_\delta = 1.5h$, 64 cloth pieces, $Re = 1.2 \times 10^3$ and up to the first agitation cycle

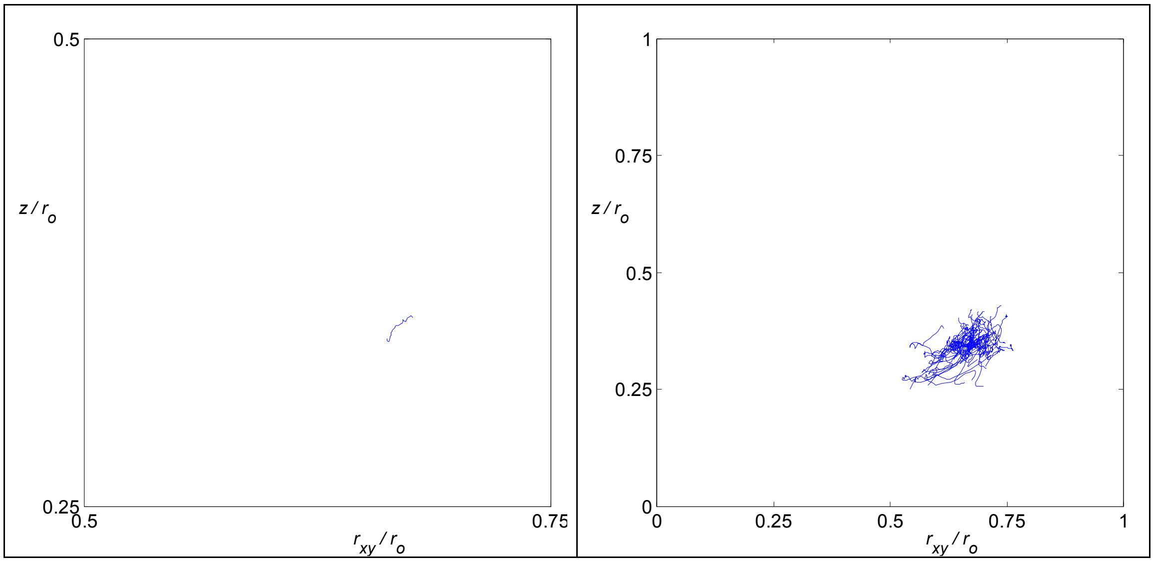

Figure 5.5-19: All cloth pieces' (left column) and each cloth piece's (right column) center of mass trajectories with $\varepsilon_\delta = 2h$, 64 cloth pieces, *Re* = 1.2 x 10^3 and up to the first agitation cycle

Additionally, the simulation using $2\varepsilon_\delta = 3h$ with 16 cloth pieces at *Re* = 1.2 x 10^3 crashed after the first agitation cycle, possibly due to numerical instability of the 'traditional' manner, in which the unbounded errors amplified in time and destroyed the simulation.

5.5.5.5 Effect of changing the Lagrangian to Eulerian mesh width ratio

As shown in Chapter 3, Section 3.5.1.2, predicting the natural frequencies of a vibrating plate's bending modes requires the Lagrangian to Eulerian mesh width ratio to be greater than or equal to unity. However, the same study showed that the predictions of the extensional vibrations were not adversely affected by using a Lagrangian to Eulerian mesh width ratio lower than unity.

In this study, by using a 1:2 Lagrangian to Eulerian mesh width ratio for a simulation with 16 cloth pieces, *Re* = 1.2 x 10^4, *Be* = 2.9 x 10^{-8}, *To* = 2.9 x 10^{-8}, and Δt = 5.03 x 10^{-4}, the motion of the cloth pieces showed an ambiguous pattern (with lesser tumbling motion) compared to the reference solution using a minimum 1:1 Lagrangian to Eulerian mesh width ratio up to the first 3 agitation cycles. On the electronic pdf version of this document click on the blue colored Lagrangian to Eulerian mesh width ratio to view the cloth motion as an embedded movie file: **1:2** and **1:1**.

In addition, Figs. 5.5-20 and 5.5-21 plot the trajectories of: i) all cloth pieces' common center of mass position (left column) and ii) each cloth piece's center of mass position (right column) on a plane spanned by the height z from the bottom of the washtub and the horizontal radius r_{xy} (defined in Eqn. 5.5-12) for the first three agitation cycles. Specifically, note in the right column of these figures that by using a minimum 1:1 Lagrangian to Eulerian mesh width ratio the center of mass trajectories of each cloth piece draw circular orbits in the way shown in Fig. 5.5-6, but the same trajectories show a more complex pattern with irregular cusps by using a ratio of 1:2. This verifies the previous observation on using the minimum ratio between the Lagrangian to Eulerian grid spacings as unity.

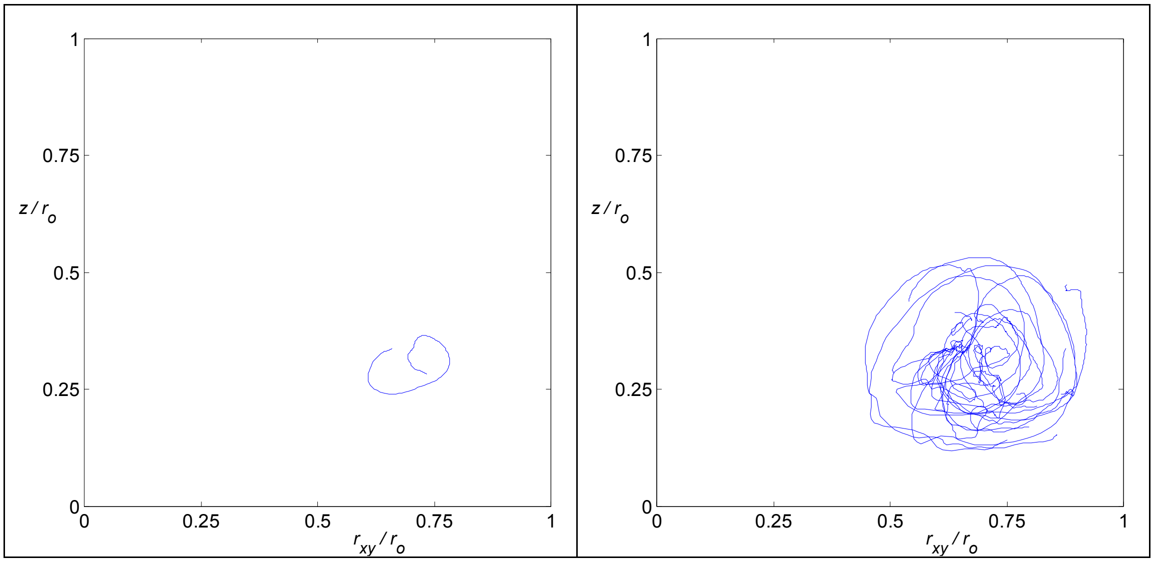

Figure 5.5-20: All cloth pieces' (left column) and each cloth piece's (right column) center of mass trajectories using a minimum 1:1 Lagrangian to Eulerian mesh width ratio with 16 cloth pieces, *Re* = 1.2 x 10^4, *Be* = 2.9 x 10^{-8}, *To* = 2.9 x 10^{-8} and up to the first 3 agitation cycles

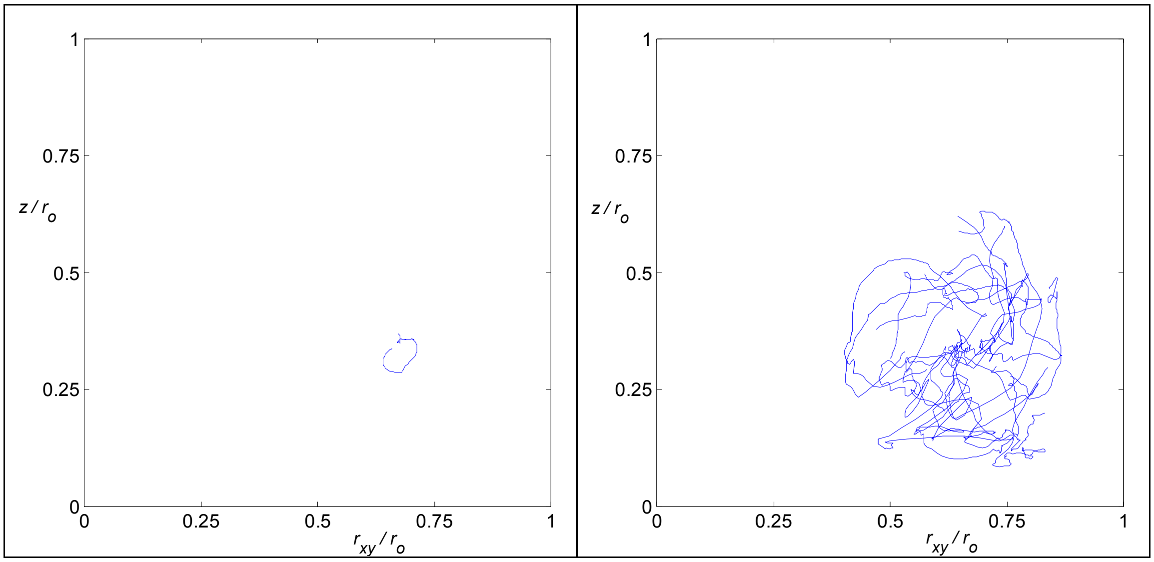

Figure 5.5-21: All cloth pieces' (left column) and each cloth piece's (right column) center of mass trajectories using a minimum 1:2 Lagrangian to Eulerian mesh width ratio with 16 cloth pieces, *Re* = 1.2 x 10^4, *Be* = 2.9 x 10^{-8}, *To* = 2.9 x 10^{-8} and up to the first 3 agitation cycles

Also, the cloth surfaces developed a rich and noisy texture using a minimum 1:2 Lagrangian to Eulerian mesh width ratio, while consuming more than two times more computational time than what was required to simulate the same time duration using a 1:1 ratio.

5.5.5.6 Effect of using a sharp vs. a smooth Heaviside function

As mentioned in Chapter 4, the simulation uses Heaviside functions to represent the complex geometries of the agitator and washtub on a Cartesian Eulerian grid with two choices: by using a sharp/discontinuous or a smoothed Heaviside function. It was found in Chapter 4 on computing the drag and lift coefficients on a circular cylinder in a uniform external flow that using a sharp Heaviside function gives more accurate results than using a smoothed function.

In this study the difference of using a sharp and a smooth (across 4 Eulerian grid spacings) Heaviside function is assessed on the cloth motion in the washtub with 16 cloth pieces, *Re* = 1.2 x 10^4 and Δt = 1.01 x 10^{-3} up to the first 2.9 agitation cycles. Note that, all the previously reported three-dimensional washing machine simulations in this chapter used a sharp Heaviside function (as stated in Table 5.5-1). Figures 5.5-22 and 5.5-23 plot the trajectories of: i) all cloth pieces' common center of mass position (left column) and ii) each cloth piece's center of mass position (right column) on a plane spanned by the height z from the bottom of the washtub and the horizontal radius r_{xy} (defined in Eqn. 5.5-12). Specifically, note that with using a sharp Heaviside function the trajectories follow the expected circular orbits of Fig. 5.5-6, while they show an ambiguous pattern with using a smooth Heaviside function. This verifies the effectiveness of using sharp Heaviside functions for the simulations.

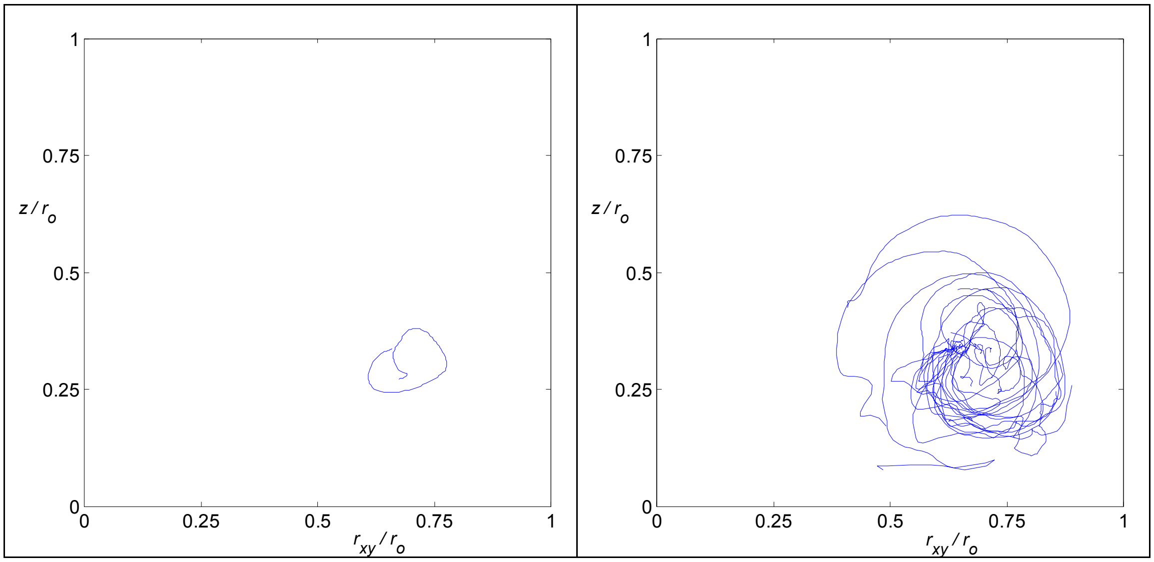

Figure 5.5-22: All cloth pieces' (left column) and each cloth piece's (right column) center of mass trajectories using sharp Heaviside function with 16 cloth pieces, *Re* = 1.2 x 10^4 up to the first 2.9 agitation cycles

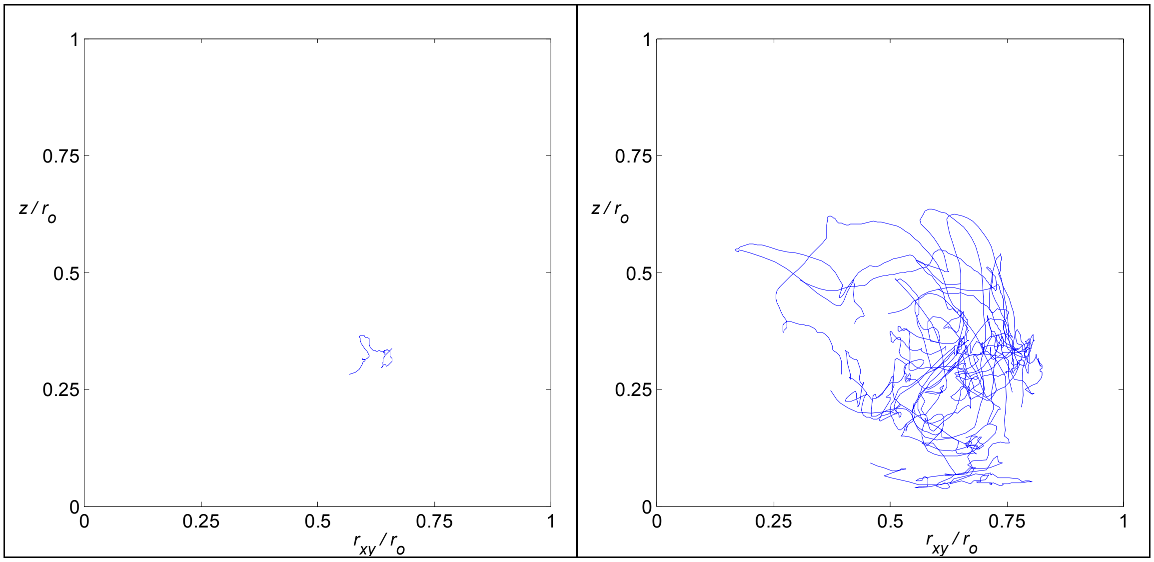

Figure 5.5-23: All cloth pieces' (left column) and each cloth piece's (right column) center of mass trajectories using a smooth Heaviside function with 16 cloth pieces, *Re* = 1.2 x 10^4 up to the first 2.9 agitation cycles

CHAPTER VI
SUMMARY, CONCLUSIONS, AND CONTRIBUTIONS

6.1 Summary

In developing a simulation of the washing machine processes, cloth, fluid, and fluid/structure interaction in arbitrary complicated three-dimensional geometries have been separately modeled and the performances of these models have been individually compared to relevant but simpler problems reported in the literature. In particular:

- Chapter 2 presents the simulation's Navier-Stokes equations solver, namely the method of Brown et al. (2001). The simulation implements this algorithm with a staggered Cartesian Eulerian grid and solves the linear sets of equations with the iterative Generalized Minimum Residual (GMRES) and the Weighted Jacobi method with Geometric Multigrid preconditioning.

  This implementation was successfully verified with the two-dimensional lid-driven cavity problem

- In Chapter 3, a large deformation one- and two-dimensional thin cloth model was developed by adapting the existing model of Love (1944). It further assumes:
  1) the cloth is elastic,
  2) the strains are small and Hooke's law is applicable,
  3) the smallest radius of curvature of the deformed cloth is much larger than the cloth thickness, and
  4) the change of the cloth's angular momentum is negligible (i.e. the Euler assumption), which is true if the bending deformations are slower than the velocity scales of the cloth natural frequencies.

The solid model’s flexible-dynamics were successfully compared against some of the natural frequencies of a vibrating plate in its small deformation zone, whereas the solid model’s performance within its large deformation zone was demonstrated with static beam bending tests.

- Again in Chapter 3, the fluid/structure interaction algorithm of the simulation, the Immersed Boundary method of Peskin (1972), was presented. Using moving Lagrangian points to trace thin solids, this method desingularizes infinitesimal solid material properties on an Eulerian grid and then solves the coupled solid and fluid dynamics together by forming a single, variable-coefficient Navier-Stokes equation. This method assumes the cloth is impermeable.

  This part of the simulation was tested against the motion of a fluttering plate as it descends under its own weight in water. Although the results of this test problem were not as closely matched as the previously mentioned verification studies, a clear convergence trend in the results to the experimental observations was apparent by increasing the numerical resolution.

- In Chapter 4, a method for using irregular rigid geometries at boundaries of the fluid/cloth mixture was presented. This part of the simulation allows simple structured Cartesian grids to be used with irregular domains such as the agitator and washtub of a washing machine. This formulation uses sharp or smoothed Heaviside functions to formulate a single equation describing both the fluid/cloth mixture and the solid boundary. Although developed independently, a very similar algorithm was also found to exist in the literature (Al-Rawahi et al. (2002) and Son (2005)). Note that, these existing methods used smooth Heaviside functions, while in this study it was shown that the sharp functions are superior to the smooth ones.

This part of the simulation was successfully verified with test problems involving the measurement of drag and lift coefficients on a cylinder in a uniform cross flow and predicting the velocity field of an axisymmetric Couette flow.

Assembling these different modules, Chapter 5 presents the two- and three-dimensional simulations of cloth pieces in a vertical-axis washing machine, whose agitator and outer drum are modeled using the technique mentioned above for irregular rigid geometries at boundaries of the fluid/cloth mixture. In addition, the present simulation uses a non-moving, slip-free surface for the dynamically evolving water-air surface in the washing machine.

The results of the three-dimensional washing machine simulations do not contain a grid convergence study due to the computational restrictions. On the other hand, the current study lacked time and resources for an experimental comparison. For these reasons no conclusions can be given on the accuracies of the quantitative results reported here. However, the two-dimensional simulations showed convergence trends in the statistics of the maximum absolute cloth stresses by increasing the grid resolution in a viscous wash-fluid, while the viscous three-dimensional simulations predicted a realistic and qualitatively correct pattern for the motion of the cloth pieces, hinting the simulation's capability to give predictions if computational resources are provided.

6.2 Specific conclusions

1) It was determined in Chapter 5, Section 5.5.5.2 that in a vertical-axis washing machine with a rotating agitator at the bottom of the washtub, cloth pieces move in a way that is shown in Fig. 6.2-1 below. Furthermore, it was determined that within more viscous wash-fluids all the cloth pieces' center of mass position is nearly immobile and the cloth pieces retain a relatively simple shape, while they slowly tumble around small rings as shown in Fig. 6.2-2 below. On the other hand, in less viscous wash-fluids these rings are not as strong and cloth pieces move more independently on the orbits shown in Fig. 6.2-1.

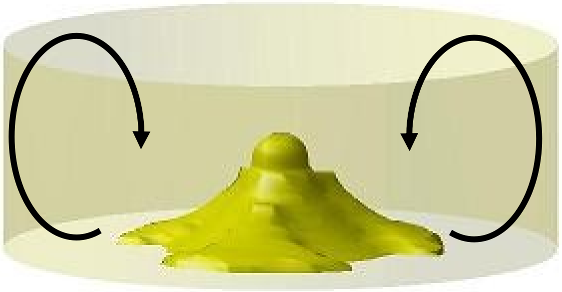

Figure 6.2-1: The representative orbits of the cloth pieces inside a vertical axis washing machine

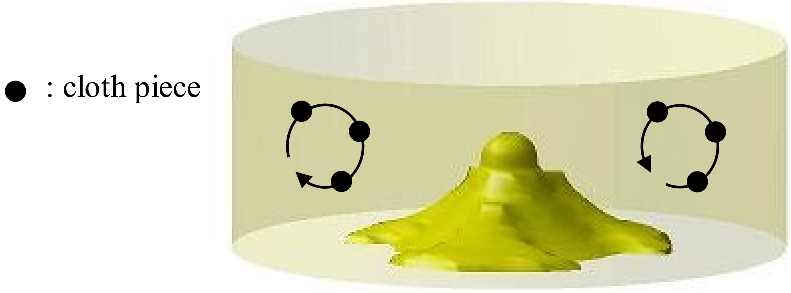

Figure 6.2-2: Cloth pieces moving in different phases around circular rings at low *Re*

2) It was determined in Chapter 5, Section 5.5.5.3 on the three-dimensional washing machine simulations that the effect of increasing cloth loading using the same Eulerian grid size leads nearby cloth pieces to interact and behave more like a single deformable solid. Although this might be due to the increased viscous stresses, using a narrower desingularization width at the same dense cloth loading showed an improvement of the individual cloth motions at the expense of reduced numerical stability.

3) In the context of the Immersed Boundary method, it was shown in Chapter 3, Section 3.5.1.2 that the simulation cannot predict the natural frequencies of a vibrating plate corresponding to its bending mode by using a Lagrangian to Eulerian mesh width ratio smaller than 1. On the other hand, the simulation was able to predict the natural frequency corresponding to the extensional vibrations by using a ratio of 0.29. Furthermore, the motion of the cloth pieces inside a

vertical-axis washing machine by using a 1:2 Lagrangian to Eulerian mesh width ratio was rather ambiguous compared to the qualitatively correct motion (as illustrated in Fig. 6.2-1) computed by using a 1:1 ratio. So it is recommended that the minimum Lagrangian to Eulerian mesh width ratio should be 1 in simulations.

4) It was shown in Chapter 3, Section 3.5.1.4 that, at least in the context of predicting the natural bending frequencies of a vibrating plate, the Dirac-delta function approximate used in the Immersed Boundary method formulation favors a full desingularization width of 4 Eulerian mesh spacings. Using a narrower width gives more accurate but less stable results using the same numerical parameters. It was also found that using a narrower Dirac-delta function width in Eqn. (3.2-13) (for approximating the solid points' velocities) than in Eqn. (3.2-12) (for desingularizing the solids) increases the vulnerability of the simulation to numerical instabilities. This last issue was also observed in the washing machine simulations.

5) It was shown in Chapter 3, Section 3.5.1 that the simulation is able to predict the natural frequencies of a plate's bending, torsion, and extensional modes for small amplitude vibrations. In addition, Section 3.5.2 shows agreement between the theoretical and computed large deformation deflected beam shapes. As expected, increasing the grid resolution while holding a constant Lagrangian to Eulerian mesh width ratio increased the accuracies of both of the results. To our knowledge, this is the first time the Immersed Boundary method formulation has been verified with such solid mechanics problems.

6) It was shown in Chapter 4, Section 4.3.1 for simulating an axisymmetric Couette flow that using a sharp Heaviside function for the simulation's algorithm to represent circular walls on a Cartesian grid gave slightly more accurate results on coarse grids than using a smooth function. Also, it was shown in Chapter 4, Section 4.3.2 for predicting the drag and lift coefficients on a cylinder in a uniform cross fluid flow that the algorithm using a sharp Heaviside function

predicts more accurate results than using a smooth function at the same grid size. Therefore, it is determined that sharp Heaviside functions are better suited for representing complex geometries on Cartesian grids.

7) It was shown in Chapter 5, Section 5.4.4.3 on the two-dimensional washing machine simulations that using a sharp Heaviside function within the simulation's algorithm to represent an agitator on a Cartesian grid permits the cloth pieces to come very close to the agitator and even sometimes slightly penetrate into it. On the other hand, by using a smooth Heaviside function the cloth pieces are kept at a small distance away from the agitator. Additionally, it was shown in Chapter 5, Section 5.5.5.6 that the realistic and qualitatively correct pattern for the motion of the cloth pieces in a vertical-axis washing machine shown in Fig. 6.2-1 could only be predicted by using a sharp Heaviside function.

8) It was shown in Chapter 3, Section 3.5.3 that the simulation is able to take a very large bending stiffness parameter and simulate a rigid plate. Also, the simulation's fluid/structure interaction model captured the fluttering phenomena of a plate descending in water under its own weight. The computed time histories of the plate's center of mass velocity components were found to be converging to the experimental values reported in Andersen (2005).

9) It was shown in Chapter 5, Section 5.5.5.1 on the three-dimensional washing machine simulations that unless the time step is small enough, the cloth pieces might sometimes penetrate into the agitator as they proceed to the bottom of the washtub in a way shown in Fig. 6.2-1. When this happens, the trapped cloth piece moves with the agitator causing the cloth to get very crumpled and this challenges the robustness of the simulations.

6.3 Contributions

The contributions of this dissertation can be counted as:

- This is the first such detailed computational study including the mechanical effects of wash-fluid/cloth coupling on the motion of the cloth pieces in a washing machine. The model was able to predict a realistic and qualitatively correct pattern for the motion of the cloth pieces in a vertical-axis washing machine. The final model is a combination of established simulation techniques and theories for both thin plates and fluids.

- This is, to our knowledge, the first time a large deformation thin plate/shell model has been used with the Immersed Boundary method formulation. This study also includes thorough verification studies to test the consistency of the model for reduced complexity fluid and cloth motions. Note that Givelberg (2004) has previously used a small deformation shell model with the Immersed Boundary method.

- A domain-mapping technique has been developed to represent irregular geometries on simple Cartesian grids. Although developed independently, a very similar algorithm was also found to exist in the literature (Al-Rawahi et al. (2002) and Son (2005)). However, these previous studies have used smooth Heaviside functions to switch between solving the fluid equations and specifying the boundary conditions, while in this study it is shown that using sharp (discontinuous) Heaviside functions are superior compared to the smoothed functions.

- It was found that a minimum Lagrangian to Eulerian mesh width ratio of 1 should be used in simulations using the Immersed Boundary method if solids are modeled with a finite bending stiffness.

BIBLIOGRAPHY

Al-Rawahi, N; Tryggvason, G. 2002. Numerical simulation of dendritic solidification with convection: Two-dimensional geometry. Journal of computational physics 180 (2): 471-496.

Andersen, A; Pesavento, U; Wang, ZJ. 2005. Unsteady aerodynamics of fluttering and tumbling plates. Journal of fluid mechanics 541: 65-90.

Aref, H. 1984. Stirring by chaotic advection. Journal of fluid mechanics 143: 1-21.

Attar, PJ; Dowell, EH; Tang, D. 2003. Modeling aerodynamic nonlinearities for two aeroelastic configurations: delta wing and flapping flag. AIAA SDM Conference, April 2003, Norfolk, VA, paper AIAA-2003-1402.

Baraff, D; Witkin, A. 1998. Large steps in cloth simulation. Computer graphics proceedings, Annual conference series, SIGGRAPH 98, Orlando, July 19-24.

Bassett, RJ; Postle, R; Pan, N. 1999. Experimental methods for measuring fabric mechanical properties: A review and analysis. Textile research journal 69 (11): 866-875.

Bell, JB; Colella, P; Howell, LH. 1991. An efficient second-order projection method for viscous incompressible flow. Proceedings of the 10th AIAA Computational Fluid Dynamics Conference, June 1991: pg. 360.

Bell, JB; Colella, P; Glaz, HM. 1989. A 2nd-order projection method for the incompressible Navier-Stokes equations. Journal of computational physics 85 (2): 257-283.

Belmonte, A; Eisenberg, H; Moses, E. 1998. From flutter to tumble: Inertial drag and Froude similarity in falling paper. Physical review letters 81 (2): 345-348.

Bickley, WG. 1934. The heavy elastica. Philosophical magazine 17 (113): 603-622, sp. Iss. 7th series.

Boisse, P; Zouari, B; Daniel, JL. 2006. Importance of in-plane shear rigidity in finite element analyses of woven fabric composite preforming. Composites part a-applied science and manufacturing 37 (12): 2201-2212, sp. Iss. SI.

Boisse, P; Gasser, A; Hagege, B; Billoet, JL. 2005. Analysis of the mechanical behavior of woven fibrous material using virtual tests at the unit cell level. Journal of materials science 40 (22): 5955-5962.

Boisse, P; Gasser, A; Hivet, G. 2001. Analyses of fabric tensile behaviour: determination of the biaxial tension-strain surfaces and their use in forming simulations. Composites part a-applied science and manufacturing 32 (10): 1395-1414, sp. Iss. Si.

Breen, DE; House, DH; Wozny, MJ. 1994. A particle-based model for simulating the draping behavior of woven cloth. Textile research journal 64 (11): 663-685.

Bridson, R; Marino, S; Fedkiw, R. 2003. Simulation of clothing with folds and wrinkles. Eurographics/SIGGRAPH symposium on computer animation (eds. Breen, D; Lin, M).

Briggs, WL; Henson, VE; McCormick, SF. 2000. A multigrid tutorial. 2nd Edition. SIAM.

Brown, DL; Cortez, R; Minion, ML. 2001. Accurate projection methods for the incompressible Navier-Stokes equations. Journal of computational physics 168 (2): 464-499.

Brown, DL. 2001. Accuracy of projection methods for the incompressible Navier-Stokes equations. UCRL-JC-144037. Presented at the Half-Moon Bay conference on incompressible flows.

Cerda, E; Mahadevan, L. 2005. Confined developable elastic surfaces: cylinders, cones and the Elastica. Proceedings of the Royal Society A-mathematical physical and engineering sciences 461 (2055): 671-700.

Chen, BJ; Govindaraj, M. 1995. A physically-based model of fabric drape using flexible shell theory. Textile research journal 65 (6): 324-330.

Chen, M; Sun, Q; Yuen, M. 1998. Simulation of fabric drape using a thin plate element with finite rotation. Acta mechanica sinica (English series) 14 (3): 239-247.

Chen, XY; Zha, GC. 2005. Fully coupled fluid-structural interactions using an efficient high resolution upwind scheme. Journal of fluids and structures 20 (8): 1105-1125.

Chorin, AJ; Marsden, JE. 1990. A mathematical introduction to fluid mechanics. 2nd Edition. Springer-Verlag.

Chorin, AJ. 1969. On convergence of discrete approximations to Navier-Stokes equations. Mathematics of computation 23 (106): 341-353.

Clark, SK. 1972. Dynamics of continuous elements. Prentice-Hall, Inc.

Coirier, WJ; Powell, KG. 1996. Solution-adaptive Cartesian cell approach for viscous and inviscid flows. AIAA journal 34 (5): 938-945.

Coirier, WJ; Powell, KG. 1995. An accuracy assessment of cartesian-mesh approaches for the Euler equations. Journal of computational physics 117 (1): 121-131.

Courant, R; Hilbert, D. 1953. Methods of mathematical physics. Interscience Publishers.

Denaro, FM. 2003. On the application of the Helmholtz-Hodge decomposition in projection methods for incompressible flows with general boundary conditions. International journal for numerical methods in fluids 43 (1): 43-69.

DeZeeuw, D; Powell, KG. 1993. An adaptively refined Cartesian mesh solver for the Euler equations. Journal of computational physics 104 (1): 56-68.

Dillon, R; Fauci, L; Fogelson, A; Gaver, D. 1996. Modeling biofilm processes using the immersed boundary method. Journal of computational physics 129 (1): 57-73.

Fadlun, EA; Verzicco, R; Orlandi, P; Mohd-Yusof, J. 2000. Combined immersed-boundary finite-difference methods for three-dimensional complex flow simulations. Journal of computational physics 161 (1): 35-60.

Fauci, LJ; Mcdonald, A. 1995. Sperm motility in the presence of boundaries. Bulletin of mathematical biology 57 (5): 679-699.

Fauci, LJ; Fogelson, AL. 1993. Truncated Newton methods and the modeling of complex immersed elastic structures. Communications on pure and applied mathematics 46 (6): 787-818.

Fauci, LJ; Peskin, CS. 1988. A computational model of aquatic animal locomotion. Journal of computational physics 77 (1): 85-108.

Ferziger, JH; Peric, M. 2002.Computational methods for fluid dynamics. 3rd Edition. Springer-Verlag.

Fung, YC. 1965. Foundations of solid mechanics. Prentice-Hall, Inc.

Ghia, U; Ghia, KN; Shin, CT. 1982. High-Re solutions for incompressible-flow using the Navier-Stokes equations and a multigrid method. Journal of computational physics 48 (3): 387-411.

Gibson, SFF; Mirtich, B. 1997. A survey of deformable modeling in computer graphics. Mitsubishi Electric Research Laboratory (MERL) technical report: TR-97-19.

Givelberg, E. 2004. Modeling elastic shell immersed in fluid. Communications on pure and applied mathematics, 57 (3): 283-309.

Goldstein, D; Handler, R; Sirovich, L. 1993. Modeling a no-slip flow boundary with an external force-field. Journal of computational physics 105 (2): 354-366.

Gresho, PM. 1991. Incompressible fluid-dynamics - some fundamental formulation issues. Annual review of fluid mechanics 23: 413-453.

Guj, G; Stella, F. 1993. A vorticity velocity method for the numerical-solution of 3D incompressible flows. Journal of computational physics 106 (2): 286-298.

Harlow, FH; Welch, JE. 1965. Numerical calculation of time-dependent viscous incompressible flow of fluid with free surface. Physics of fluids 8 (12): 2182.

House, DH; DeVaul, RW. 1996. Towards simulating cloth dynamics using interacting particles. International journal of clothing science and technology 8 (3): 75-94.

Hu, JL; Zhang, YT. 1997. The KES shear test for fabrics. Textile research journal 67 (9): 654-664.

Kang, TJ; Joo, KH; Lee, KW. 2004. Analyzing fabric buckling based on nonlinear bending properties. Textile research journal 74 (2): 172-177.

Kawabata, S. 1980. Standardization and analysis of hand evaluation. 2nd Edition. The Textile Machinery Society of Japan.

Kim, J; Kim, D; Choi, H. 2001. An immersed-boundary finite-volume method for simulations of flow in complex geometries. Journal of computational physics 171 (1): 132-150.

Kim, J; Moin, P. 1985. Application of a fractional-step method to incompressible Navier-Stokes equations. Journal of computational physics 59 (2): 308-323.

King, MJ; Jearanaisilawong, P; Socrate, S. 2005. A continuum constitutive model for the mechanical behavior of woven fabrics. International journal of solids and structures 42 (13): 3867-3896.

Kirkpatrick, MP; Armfield, SW; Kent, JH. 2003. A representation of curved boundaries for the solution of the Navier-Stokes equations on a staggered three-dimensional Cartesian grid. Journal of computational physics 184 (1): 1-36.

Koiter, WT. 1960. A consistent first approximation in the general theory of thin elastic shells. Theory of thin elastic shells – Proceedings of 1st IUTAM symposium; Koiter, WT, (ed.), Amsterdam; North-Holland Publishing Company: 12-33.

Koumoutsakos, P. 2005. Multiscale flow simulations using particles. Annual review of fluid mechanics 37: 457-487.

Krasny, R. 1990. Vortex sheet roll-up due to the motion of a flat plate. Proceedings of the international symposium on nonsteady fluid dynamics, Toronto, Canada (eds. Miller, JA; Telionis, DP), ASME Fluids Engineering Division 92: 449-453.

Kundu, PK; Cohen, IM. 2004. Fluid mechanics. 3rd Edition. Elsevier Academic Press.

Le, DV; Khoo, BC; Peraire, J. 2006. An immersed interface method for viscous incompressible flows involving rigid and flexible boundaries. Journal of computational physics 220 (1): 109-138.

Lee, L; Leveque, RJ. 2003. An immersed interface method for incompressible Navier-Stokes equations. SIAM journal on scientific computing 25 (3): 832-856.

Lee, L. 2002. Immersed interface methods for incompressible flow with moving interfaces. Ph.D. thesis, University of Washington, Seattle, WA, USA.

Leissa, AW. 1969. Vibrations of plates. National Aeronautics and Space Administration (NASA).

Leveque, RJ; Li, ZL. 1997. Immersed interface methods for Stokes flow with elastic boundaries or surface tension. SIAM journal on scientific computing 18 (3): 709-735.

Li, ZL; Lai, MC. 2001. The immersed interface method for the Navier-Stokes equations with singular forces. Journal of computational physics 171 (2): 822-842.

Lo, WM; Hu, JL. 2002. Shear properties of woven fabrics in various directions. Textile research journal 72 (5): 383-390.

Love, AEH. 1944. A treatise on the mathematical theory of elasticity. 4th Edition. Dover Publications.

Lu, L; Chen, J; Xiang, L; Sherwood, J. 2005. Two-dimensional macro-mechanics shear models of woven fabrics. Composites part a-applied science and manufacturing 36 (1): 105-114.

Lugt, HJ. 1983. Autorotation. Annual review of fluid mechanics 15: 123-147.

Ly, NG; Tester, DH; Buckenham, P; Roczniok, AF; Adriaansen, AL; Scaysbrook, F; Dejong, S. 1991. Simple instruments for quality-control by finishers and tailors. Textile research journal 61 (7): 402-406.

Malvern, LE. 1969. Introduction to the mechanics of a continuous medium. Prentice-Hall, Inc.

Marella, S; Krishnan, S; Liu, H; Udaykumar, HS. 2005. Sharp interface Cartesian grid method I: An easily implemented technique for 3D moving boundary computations. Journal of computational physics 210 (1): 1-31.

McQueen, DM; Peskin, CS. 2000. A three-dimensional computer model of the human heart for studying cardiac fluid dynamics. Computer graphics-us 34 (1): 56-60.

McQueen, DM; Peskin, CS. 1989. A 3-dimensional computational method for blood-flow in the heart .2. Contractile fibers. Journal of computational physics 82 (2): 289-297.

Mohd-Yusof, J. 1997. Combined immersed boundaries/b-splines methods for simulations of flows in complex geometries. CTR Annual Briefs, NASA Ames/Stanford University.

Morton, KW; Mayers DF. 1994. Numerical solution of partial differential equations. Cambridge University Press.

Pai, PF; Nayfeh, AH. 1992. A nonlinear composite shell theory. Nonlinear dynamics 3: 431-463.

Peskin, CS. 2002. The immersed boundary method. Acta numerica: 1-39.

Peskin, CS; Mcqueen, DM. 1989. A 3-dimensional computational method for blood-flow in the heart .1. Immersed elastic fibers in a viscous incompressible fluid. Journal of computational physics 81 (2): 372-405.

Peskin, CS. 1977. Numerical-analysis of blood-flow in heart. Journal of computational physics 25 (3): 220-252.

Peskin, CS. 1972. Flow patterns around heart valves - numerical method. Journal of computational physics 10 (2): 252-271.

Pope, SB. 2000. Turbulent flows. Cambridge University Press.

Pozrikidis, C. 2001. A note on the regularization of the discrete Poisson-Neumann problem. Journal of computational physics 172 (2): 917-923.

Russo, G; Smereka, P. 2000. A remark on computing distance functions. Journal of computational physics 163 (1): 51-67.

Sani, RL; Gresho, PM. 1994. Resume and remarks on the open boundary-condition minisymposium. International journal for numerical methods in fluids 18 (10): 983-1008.

Silva, ALFLE; Silveira-Neto, A; Damasceno, JJR. 2003. Numerical simulation of two-dimensional flows over a circular cylinder using the immersed boundary method. Journal of computational physics 189 (2): 351-370.

Son, G. 2005. A level set method for incompressible two-fluid flows with immersed solid boundaries. Numerical heat transfer part b-fundamentals 47 (5): 473-489.

Stockie, JM; Wetton, BR. 1999. Analysis of stiffness in the immersed boundary method and implications for time-stepping schemes. Journal of computational physics 154 (1): 41-64.

Su, SW; Lai, MC; Lin, CA. 2007. An immersed boundary technique for simulating complex flows with rigid boundary. Computers & fluids 36 (2): 313-324.

Sussman, M; Smereka, P; Osher, S. 1994. A level set approach for computing solutions to incompressible 2-phase flow. Journal of computational physics 114 (1): 146-159.

Taibi, EH; Hammouche, A; Kifani, A. 2001. Model of the tensile stress-strain behavior of fabrics. Textile research journal 71 (7): 582-586.

Teixeira, J; Reynolds, CA; Judd, K. 2007. Time step sensitivity of nonlinear atmospheric models: Numerical convergence, truncation error growth, and ensemble design. Journal of the atmospheric sciences 64 (1): 175-189.

Temam, R. 1968. An approximation method for solving Navier-Stokes equations. Bulletin de la societe mathematique de france 96 (2): 115.

Terzopoulos, D; Platt, J; Barr, A; Fleischer, K. 1987. Elastically deformable models. Computer graphics (proc. SIGGRAPH) 21 (4): 205-214

Trefethen, LN; Bau, D III. 1997. Numerical Linear Algebra. SIAM.

Tryggvason, G; Bunner, B; Esmaeeli, A; Juric, D; Al-Rawahi, N; Tauber, W; Han, J; Nas, S; Jan, YJ. 2001. A front-tracking method for the computations of multiphase flow. Journal of computational physics 169 (2): 708-759.

Tseng, YH; Ferziger, JH. 2003. A ghost-cell immersed boundary method for flow in complex geometry. Journal of computational physics 192 (2): 593-623.

Udaykumar, HS; Mittal, R; Rampunggoon, P; Khanna, A. 2001. A sharp interface cartesian grid method for simulating flows with complex moving boundaries. Journal of computational physics 174 (1): 345-380.

Unverdi, SO; Tryggvason, G. 1992. A front-tracking method for viscous, incompressible, multi-fluid flows. Journal of computational physics 100 (1): 25-37.

van Loon, R; Anderson, PD; van De Vosse, FN; Sherwin, SJ. 2007. Comparison of various fluid-structure interaction methods for deformable bodies. Computers & structures 85 (11-14): 833-843, sp. Iss. SI.

Ventsel, E; Krauthammer, T. 2001. Thin plates and shells. Marcel Dekker, Inc.

Ward, D. 1999. Modelling of a horizontal-axis domestic washing machine. Journal of the textile institute, Part 1, Fiber science and textile technology

Weinan, E; Liu, JG. 1996. Vorticity boundary condition and related issues for finite difference schemes. Journal of computational physics 124 (2): 368-382.

Williamson, CHK. 1996. Vortex dynamics in the cylinder wake. Annual review of fluid mechanics 28: 477-539.

Xue, P; Peng, XQ; Cao, J. 2003. A non-orthogonal constitutive model for characterizing woven composites. Composites part a-applied science and manufacturing 34 (2): 183-193.

Ye, T; Mittal, R; Udaykumar, HS; Shyy, W. 1999. An accurate Cartesian grid method for viscous incompressible flows with complex immersed boundaries. Journal of computational physics 156 (2): 209-240.

Yokoi, K. 2003. Numerical method for a moving solid object in flows. Physical review E 67 (4).

Yokota, R; Sheel, TK; Obi, S. 2007. Calculation of isotropic turbulence using a pure Lagrangian vortex method. Journal of computational physics. In press.

York, AR; Sulsky, D; Schreyer, HL. 2000. Fluid-membrane interaction based on the material point method. International journal for numerical methods in engineering 48 (6): 901-924.

Yu, WR; Kang, TJ; Chung, K. 2000. Drape simulation of woven fabrics by using explicit dynamic analysis. Journal of the textile institute 91 (2): 285-301, part 1.

Zhang, YT; Xie, YX. 2003. Nonlinear micro-mechanical model for plain woven fabric. Acta mechanica solida sinica 16 (2): 134-140.

Zhao, LJ; Tsukamoto, H. 2007. Hybrid vortex method for high Reynolds number flows around three-dimensional complex boundary. Computers & fluids 36 (7): 1213-1223.

Zhao, YF; Wong, TN; Tan, ST; Chen, WJ. 1997. A model for simulating flexible surfaces of cloth objects. Computers & structures 63 (1): 133-147.

Zhu, LD; Peskin, CS. 2003. Interaction of two flapping filaments in a flowing soap film. Physics of fluids 15 (7): 1954-1960.

Zhu, LD; Peskin, CS. 2002. Simulation of a flapping flexible filament in a flowing soap film by the immersed boundary method. Journal of computational physics 179 (2): 452-468.